



Norwegian University of  
Science and Technology

# Hydraulic Design of Francis Turbine Exposed to Sediment Erosion

Kristine Gjørseter

Master of Science in Energy and Environment

Submission date: June 2011

Supervisor: Ole Gunnar Dahlhaug, EPT

Co-supervisor: Mette Eltvik, EPT



**MASTER THESIS**

For

Stud.techn.

Kristine Gjørseter

Spring 2011

**Hydraulic design of Francis turbine exposed to sediment erosion**

**Background**

Sediment erosion in Francis turbines is a large problem for river power plants near the Himalayas and the Andes Mountains. Due to high sediment concentration in the rivers the turbine components are exposed to erosion wear and must be maintained often. During monsoon periods, the sediment concentration is at its highest and the turbines are stopped to reduce the damage on the components. The turbines at Jhimruk Power Plant in Nepal are a good example on how the sediment erosion effects the power plant operation. These turbines need to be maintained annually due to high erosion wear. This result in a reduction of power production and high maintenance cost. It is therefore of interest to design a new Francis turbine which is more resistant to sediment erosion. A cooperation between Kathmandu University and NTNU has started and aim to start manufacture Francis turbines that can withstand high sediment load.

**Objective**

The aim is to carry out a hydraulic design a new Francis turbine where the velocity components are reduced.

**The following tasks shall be considered in the project work:**

1. Literature survey
  - a. Erosion in Francis turbines
2. Software knowledge
  - a. Optimization tool within Matlab
  - b. Get familiar with the CFD-tool; Ansys CFX
3. The student has to learn how Ansys CFX and the optimization tools within Matlab will be used for the parametric study of the Francis turbine design.
4. The student will design a Francis turbine using Matlab as a programming tool
5. Parametric study of the turbine design by using Matlab and CFD-analysis



--- " ---

Within 14 days of receiving the written text on the diploma thesis, the candidate shall submit a research plan for his project to the department.

When the thesis is evaluated, emphasis is put on processing of the results, and that they are presented in tabular and/or graphic form in a clear manner, and that they are analyzed carefully.

The thesis should be formulated as a research report with summary both in English and Norwegian, conclusion, literature references, table of contents etc. During the preparation of the text, the candidate should make an effort to produce a well-structured and easily readable report. In order to ease the evaluation of the thesis, it is important that the cross-references are correct. In the making of the report, strong emphasis should be placed on both a thorough discussion of the results and an orderly presentation.

The candidate is requested to initiate and keep close contact with his/her academic supervisor(s) throughout the working period. The candidate must follow the rules and regulations of NTNU as well as passive directions given by the Department of Energy and Process Engineering.

Pursuant to "Regulations concerning the supplementary provisions to the technology study program/Master of Science" at NTNU §20, the Department reserves the permission to utilize all the results and data for teaching and research purposes as well as in future publications.

One – 1 complete original of the thesis shall be submitted to the authority that handed out the set subject. (A short summary including the author's name and the title of the thesis should also be submitted, for use as reference in journals (max. 1 page with double spacing)).

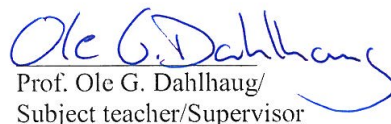
Two – 2 – copies of the thesis shall be submitted to the Department. Upon request, additional copies shall be submitted directly to research advisors/companies. A CD-ROM (Word format or corresponding) containing the thesis, and including the short summary, must also be submitted to the Department of Energy and Process Engineering

Department of Energy and Process Engineering,

Date: 31-2011



Prof. Olav Bolland  
Department Manager



Prof. Ole G. Dahlhaug/  
Subject teacher/Supervisor

Co-supervisor: Mette Eltvik, PhD-student



## Preface

This master thesis has been written at the Waterpower Laboratory, Department of Energy and Process Engineering at the Norwegian University of Science and Technology (NTNU) during the spring semester of 2011. The thesis is part of a project called *RenewableNepal*, which is in collaboration between NTNU and Kathmandu University (KU) in Nepal. The thesis is a continuation of a project assignment carried out by the author during the fall semester of 2010.

The master thesis description demands use of the optimization tools within Matlab as part of the parametric study of the turbine design. In consultation with professor Dahlhaug, this has been disregarded, as other and more appropriate tools were used instead.

The design software allows design of the entire turbine consisting of runner, guide vanes, stay vanes and spiral casing. The parametric study has however only been performed for the runner. A parameter study including the other components is recommended.

Kristine Gjørseter

Kristine Gjørseter  
Trondheim, June 13, 2011

## Acknowledgments

I would like to thank my supervisor Professor Ole Gunnar Dahlhaug for introducing me into the field of Francis turbine design. During numerous discussions, he has guided me with his great knowledge and he has inspired me a lot. I would also like to thank my co-supervisor Mette Eltvik for all the help with CFX and running programs in batch mode. Thanks for leaving the door to your office open at all times and for taking the time to help me when I needed it.

I would also like to thank the members of the Francis turbine design team: Biraj Singh Thapa and Helene P. Erichsen. It has been a pleasure working with this project and being part of the team. Thanks for all the good discussions and for our weekly team meetings. I have learned more than I ever dreamed of.

A special thank to Biraj for the fantastic cooperation we have had during this spring semester. I will remember all our moments together, both in the lab and in our spare time. And thanks for all the nice dinners, I have enjoyed a lot!

I would also like to thank Stine Trefall. I will miss our early morning breakfasts and coffee, the small chats across our desk and all the fun we have had! Also, a special thanks to Lars Frøyd for always answering my Matlab questions and for discussing my results at all hours.

And at last, thanks to all fellow students at the Waterpower Laboratory for the great working environment and for all the memorable moments, both at the lab and in Chile. I will miss you all!



## Abstract

Sediment erosion is a large problem for turbines operated in sand laden water, especially in the Himalayas and the Andes Mountains, where the contents of hard minerals in the rivers are high.

A program called *RenewableNepal* supports the development of a new design philosophy for hydraulic turbines. NTNU and Kathmandu University cooperate within this program, and this master thesis is part of that cooperation.

The objective of this thesis is to carry out the hydraulic design of a Francis turbine with reduced velocities. As part of that, a design software has been developed, using Matlab as programming tool. This software has been used to generate a reference design with the same physical dimensions as for the existing runners at Jhimruk Hydroelectric Centre in Nepal. CFD analysis has been performed to verify the design software output, showing good results. Analysis of erosion from CFD were not successful as mesh independency for the analysis could not be established. Hence results for erosion prediction from CFD studies has not been presented in this thesis.

A parametric study has been carried out, varying either the outlet diameter, the number of pole pairs, the inlet velocity, the acceleration of the flow through the runner, the height of the shroud or the blade angle distribution. An erosion model was implemented in the design software, and used as a control variable for the parametric study. CFD analyses using Ansys CFX were performed for selected designs with lower erosion than the reference design.

The largest reduction of erosion was obtained when increasing the number of pole pairs, which implies that the rotational speed of the turbine is decreased. This does however increase the size of both the turbine and the generator, which cause increased investment costs as well. CFD analysis shows that the hydraulic efficiency for this design is higher than for the reference design.

It was also discovered that by changing the blade angle distribution, and consequently also the energy distribution, a substantial reduction of erosion was possible without changing the physical dimensions or the rotational speed of the turbine. The efficiency for this design is also higher than for the reference design.

The most promising design was found as a combination of these two effects, giving a reduction of the erosion of 50 percent compared to the reference design. CFD analysis for this design show a good efficiency and acceptable flow conditions in the runner. This and other designs with the modified blade angle distribution will have an unconventional energy conversion through the runner, leading to larger hydraulic forces on the trailing edge of the blades. Strength analyses of the blade would be beneficial, but have not been performed.

The main focus in this thesis has been on developing the design software and developing runner designs for reducing sediment erosion. There have been no at-

tempts for optimizing the designs of the guide vanes and stay vanes due to time constraints.

## Sammendrag

I Himalaya og Andesfjellene er innholdet av harde mineraler i elvene svært høyt, hvilket medfører stor slitasje på vannturbiner i form av erosjon.

Et program kalt *RenewableNepal* støtter utviklingen av en ny designfilosofi for hydrauliske turbiner. NTNU og Kathmandu University samarbeider innenfor dette programmet, og denne masteroppgaven er en del av samarbeidet.

Målet med denne oppgaven er å designe en Francis turbin med reduserte strømningshastigheter for å redusere sedimenterosjon. Som en del av det, har Matlab blitt brukt til å lage et designprogram. Dette programmet har blitt brukt til å generere et referansedesign med de samme fysiske dimensjoner som for de eksisterende løpehjulene på Jhimruk Hydroelectric Centre i Nepal. CFD-analyser har blitt utført, og viser at turbinene som er generert med designprogrammet har både gode strømningsforhold og høy virkningsgrad. Analyse av erosjon ved bruk av CFD var ikke vellykket fordi resultatene ikke var griduavhengige. Disse resultatene er derfor ikke tatt med i oppgaven.

En parameterstudie er gjennomført, der enten utløpsdiameter, antall polpar, innløpshastighet, akselerasjon gjennom løpehjulet, høyde på ringen eller skovlvinkeldistribusjonen ble variert. En erosjonsmodell ble implementert i designprogrammet for å anslå mengden erosjon sammenlignet med referansedesignet. Denne parameteren ble brukt som kontrollvariabel for parameterstudiet. CFD-analyser i Ansys CFX ble utført for utvalgte design med lav erosjon.

Den største reduksjonen av erosjon ble oppnådd ved å øke antallet polpar, hvilket innebærer en reduksjon av turbinens rotasjonshastighet. Dette vil imidlertid øke størrelsen på både turbin og generator, som igjen forårsaker økte investeringskostnader. CFD-analyser viser at den hydrauliske virkningsgraden er høyere enn for referansedesignet.

Det ble også funnet at ved å endre skovlvinkeldistribusjonen, og dermed også energidistribusjonen gjennom løpehjulet, er en betydelig erosjonsreduksjon mulig uten å endre turbinens fysiske dimensjoner eller rotasjonshastighet. Virkningsgraden for dette designet var også høyere enn for referansedesignet.

Det mest lovende designet ble funnet som en kombinasjon av disse to effektene. Det gir en reduksjon av erosjon på 50 prosent sammenlignet med referansedesignet. CFD-analyse av dette designet viser god virkningsgrad og akseptable strømningsforhold i løpehjulet. Dette og andre design med endret skovlvinkeldistribusjon vil ha en ukonvensjonell energiomsetning i løpehjulet, hvilket fører til økte hydrauliske krefter nært skovlens avløpskant. Styrkeberegninger på skovlene ville i så måte vært fordelaktig, men har ikke blitt utført.

Hovedfokus for denne oppgaven har vært på utviklingen av et designprogram og på utforming av løpehjulet. Grunnet tidsmangel har det ikke blitt gjort noen forsøk på å redusere erosjonen i ledeapparatet.



# Contents

<b>1</b>	<b>Introduction</b>	<b>1</b>
1.1	Hydropower in Nepal . . . . .	1
1.2	Jhimruk Hydroelectric Centre . . . . .	1
1.3	Objective . . . . .	2
1.4	Outline . . . . .	2
<b>2</b>	<b>Background</b>	<b>3</b>
2.1	<i>RenewableNepal</i> Program . . . . .	3
2.2	The Francis Turbine Design Team . . . . .	3
2.3	Earlier Work . . . . .	3
2.4	The Design Software . . . . .	4
<b>3</b>	<b>Sediment Erosion</b>	<b>5</b>
3.1	Wear Mechanisms . . . . .	5
3.2	Sediment Erosion in Francis Turbines . . . . .	7
3.3	Parameters Influencing the Erosion Rate . . . . .	10
3.4	Erosion Classification . . . . .	11
3.5	Erosion Models . . . . .	11
<b>4</b>	<b>Francis Turbine Design</b>	<b>15</b>
4.1	Introduction . . . . .	15
4.2	Main Dimensions . . . . .	16
4.3	Runner Blades . . . . .	20
4.4	Runner . . . . .	25
4.5	Leading and trailing edge . . . . .	29
4.6	Guide vanes . . . . .	30
4.7	Stay vanes . . . . .	31
4.8	Spiral casing . . . . .	33
<b>5</b>	<b>Review of the Design Software</b>	<b>35</b>
5.1	Tab 1 - Intro . . . . .	35
5.2	Tab 2 - Main Dimensions . . . . .	36
5.3	Tab 3 - The Axial View . . . . .	37
5.4	Tab 4 - The Blade Angle Distribution and the <i>GH</i> -plane . . . . .	38
5.5	Tab 5 - The Radial View and Runner Blade . . . . .	39
5.6	Tab 6 - Blade with Thickness . . . . .	40
5.7	Tab 7 - Labyrinths . . . . .	40
5.8	Tab 8 - Guide Vanes, Stay Vanes and Spiral Casing . . . . .	41
5.9	Tab 9 - Summary . . . . .	42
<b>6</b>	<b>CFD Theory</b>	<b>43</b>
6.1	Mesh Generation: ATM Optimized Mesh . . . . .	43
6.2	Turbulence Modelling . . . . .	43
6.3	Sediment Erosion Prediction using CFD . . . . .	45

<b>7</b>	<b>Computational Model for Francis Turbines</b>	<b>47</b>
7.1	Mesh Generation . . . . .	47
7.2	Boundary Conditions . . . . .	48
<b>8</b>	<b>Reference Design</b>	<b>51</b>
8.1	CFD Analysis . . . . .	51
8.2	Erosion Prediction in CFX . . . . .	56
<b>9</b>	<b>Verification</b>	<b>57</b>
9.1	Multilevel CFD . . . . .	57
<b>10</b>	<b>Parameter Study</b>	<b>61</b>
10.1	Control Variables for the Parameter Study . . . . .	61
10.2	Single Parameter Studies . . . . .	62
10.3	Selective Parameter Studies . . . . .	85
<b>11</b>	<b>Discussion</b>	<b>89</b>
11.1	Design Software . . . . .	89
11.2	The Reference Design . . . . .	89
11.3	Single Parameter Study . . . . .	90
11.4	Selective Parameter Study . . . . .	93
<b>12</b>	<b>Conclusion</b>	<b>95</b>
<b>13</b>	<b>Further Work</b>	<b>97</b>
<b>A</b>	<b>Sediment Erosion</b>	<b>I</b>
<b>B</b>	<b>Design Software</b>	<b>XX</b>

## List of Figures

1.1	Map of Nepal with location of Jhimruk Hydro Electric Centre . . . . .	2
3.1	Mechanisms of abrasive wear [1] . . . . .	5
3.2	Mechanisms of erosive wear [1] . . . . .	6
3.3	Areas exposed to sediment erosion wear . . . . .	7
3.4	Design of stay vane inlet . . . . .	7
3.5	Illustration of particle-flow separation at high acceleration [2] . . . . .	8
3.6	Erosion in guide vanes . . . . .	9
3.7	Vortex from guide vanes causing erosion at runner inlet . . . . .	9
3.8	Erosion in runners . . . . .	10
3.9	Impact angle . . . . .	10
4.1	Axial view of a turbine [3] . . . . .	15
4.2	Velocity triangles . . . . .	16
4.3	Projection of the blade thickness into the outlet plane . . . . .	17
4.4	Determining a new point on a streamline. Adapted from Eltvik et al. [3] . . . . .	21
4.5	Axial view of the runner blade after cutting endpoints and redistributing the remaining points . . . . .	22
4.6	Definition of $G-H$ plane. Adapted from Eltvik et al. [3] . . . . .	23
4.7	$GH$ -plane . . . . .	24
4.8	Definition of $\theta$ . . . . .	24
4.9	Radial view . . . . .	24
4.10	3D-blade plotted without thickness . . . . .	25
4.11	Relative velocity in rotating channel [4] . . . . .	26
4.12	Velocity diagram at BEP (*) and at full load . . . . .	27
4.13	Blade modeled as a straight beam between hub and shroud . . . . .	28
4.14	Definition of $a$ , $b$ , $\Delta r$ and $R_M$ . . . . .	28
4.15	Shape of leading and trailing edge . . . . .	29
4.16	Geometry of guide vane . . . . .	31
4.17	Stay vanes . . . . .	32
4.18	Traditional spiral casing and simplified annulus for calculating purposes . . . . .	32
4.19	Cross section of spiral casing . . . . .	33
4.20	Secondary flow in the spiral casing . . . . .	33
5.1	Tab 1 - Intro tab . . . . .	35
5.2	Tab 2 - Main dimensions . . . . .	36
5.3	Tab 3 - Axial view . . . . .	37
5.4	Fourth power Bezier curve . . . . .	38
5.5	Tab 4 - The blade angle distribution and the $GH$ -plane . . . . .	38
5.6	Tab 5 - Radial view and runner blade . . . . .	39
5.7	Tab 6 - Blade thickness . . . . .	40
5.8	Tab 7 - Labyrinths . . . . .	41
5.9	Tab 8 - Guide vanes, stay vanes and spiral casing design . . . . .	41
5.10	Tab 9 - Summary . . . . .	42
6.1	SST model . . . . .	44

6.2	Wall function. Adapted from [5]	45
7.1	TurboGrid ATM mesh	47
7.2	Computational domain	48
7.3	Iterating for velocity components to give the design head for CFX simulations	49
8.1	$y^+$ values on runner blade for mesh with <i>Factor ratio</i> =2.0	52
8.2	Streamlines in draft tube at BEP	53
8.3	Relative velocity in runner seen from outlet and from top	54
8.4	Relative velocity in runner seen from hub and from shroud	54
8.5	Blade to blade pressure distribution	54
8.6	Trailing edge shape in TurboGrid, somewhat exaggerated	55
8.7	Erosion rate density for different mesh qualities	56
9.1	Static pressure on blade, viscous simulation results	58
9.2	Static pressure on blade, inviscid simulation results	58
9.3	Static pressure on blade, viscous simulation results	59
9.4	Static pressure on blade, inviscid simulation results	59
10.1	Effect on outlet peripheral velocity and outlet meridional velocity	63
10.2	Effects on the inlet and outlet relative velocity	63
10.3	Effect on erosion factor and required submergence. Negative value of $H_s$ means a placement below tail water level (see section 4.2)	64
10.4	Relative velocity in runner seen from outlet and from top	64
10.5	Blade to blade pressure distribution	65
10.6	Draft tube flow conditions for $D_2 = 0.64m$	65
10.7	Effect on speed number	66
10.8	Effect on outlet velocity components	67
10.9	Effect on erosion factor and submergence requirements	67
10.10	Relative velocity in runner seen from hub and from shroud	68
10.11	Streamlines in draft tube	69
10.12	Blade to blade pressure distribution	69
10.13	Effect on inlet height and inlet diameter	70
10.14	Effect on $\beta_1$ and $W_1$ when reducing $\underline{U}_1$	71
10.15	Effect on blade shape when reducing $\underline{U}_1$ . (Blade shape at hub)	71
10.16	Effect on erosion factor and reaction ratio	71
10.17	Pressure on the runner blades	72
10.18	Blade to blade pressure distribution	72
10.19	Relative velocity in runner seen from outlet and from top	73
10.20	Streamlines in the draft tube	74
10.21	Effects on inlet velocities	74
10.22	Effect on erosion factor	75
10.23	Relative velocity in runner seen from hub and from shroud	75
10.24	Blade to blade pressure distribution	76
10.25	Streamlines in the draft tube	76
10.26	Definition of height $b$	77
10.27	Effect on erosion factor	77



10.28	Pressure contours on runner blade. The blade are turned so that the trailing edge area close to the hub are visible . . . . .	78
10.29	Relative velocity in runner seen from outlet and from top . . . . .	78
10.30	Blade to blade pressure distribution . . . . .	79
10.31	Streamlines in the draft tube . . . . .	79
10.32	Different shapes of the blade angle distribution for the parameter study . . . . .	80
10.33	Erosion factor for different shapes of the blade angle distribution . .	80
10.34	GH-plane plots for different blade angle distributions . . . . .	81
10.35	Energy distributions for different blade angle distributions . . . . .	81
10.36	Shape of the blade for different blade angle dstribution . . . . .	81
10.37	Blade to blade pressure distribution . . . . .	83
10.38	Blade to blade pressure distribution for $\beta$ -distribution shape 1 at midway from hub to shroud . . . . .	83
10.39	Relative velocity in runner . . . . .	84
10.40	Streamlines in the draft tube . . . . .	84
10.41	Flow in the draft tube . . . . .	86
10.42	Relative velocity in runner . . . . .	86
10.43	Relative velocity in runner . . . . .	87

# List of Tables

7.1	Boundary layer refinement control data . . . . .	47
8.1	Reference turbine data . . . . .	51
8.2	Reference turbine mesh data . . . . .	52
8.3	Comparison of reference turbine data from design software and CFX	52
9.1	Mesh size information . . . . .	57
9.2	Fine mesh simulation results . . . . .	58
9.3	Coarse mesh simulation results . . . . .	59
10.1	Parameters for single effects study . . . . .	62
10.2	Simulation results $D_2=0.64$ m . . . . .	65
10.3	Simulation results six pole pairs . . . . .	70
10.4	Simulation results $\overline{U}_1=0.63$ . . . . .	73
10.5	Simulation results $Acc=50\%$ . . . . .	76
10.6	Simulation results $b=0.4$ m . . . . .	78
10.7	Simulation results $\beta$ -distribution shape 1 . . . . .	84
10.8	Simulation results selective design no. 1 . . . . .	85
10.9	Simulation results selective design no. 2 . . . . .	87
11.1	Design parameter values combined with blade angle distribution shape 1. The values of the parameters not listed are chosen equal to the reference design value . . . . .	94

# Nomenclature

## Symbols

Symbol	Description	Unit
$a$	Difference between inlt and outlet radius of runner	$m$
$A$	Area	$m^2$
$b$	Height of shroud	$m$
$B$	Height	$m$
$C$	Absolute velocity	$m/s$
$D$	Diameter	$m$
$E_f$	Erosion factor	—
$E_t$	Erosion tendency	$m^3/s^3$
$f$	Frequency	$Hz$
$F$	Force	$N$
$g$	Gravity	$m/s^2$
$G$	Length of streamline in axial direction	$m$
$H$	Length of streamline in radial direction	$m$
$H_e$	Head	$m$
$i$	Factor that relate erosion rate and velocity	—
$I$	Second area moment of inertia	$m^4$
$K$	Constant	—
$L$	Length	$m$
$m$	Mass	$kg$
$M$	Bending moment	$Nm$
$M$	Non-dimensional mass	—
$n$	Rotational speed	$rpm$
$n$	Line normal to streamlines	$m$
$\dot{N}$	Particle number rate	$1/m^2s$
$p$	Pressure	$Pa$
$p$	Particles per unit surface area	—
$P$	Power	$W$
$q$	Load	$kg/s^2$
$Q$	Flow rate	$m^3/s$
$r$	Radius	$m$
$r_{curv}$	Radius of curvature	$m$
$R$	Radius	$m$
$S$	Abrasive depth	$mm$
$t$	Thickness	$m$
$U$	Peripheral velocity	$m/s$
$W$	Relative velocity	$m/s$
$y^+$	Non-dimensional distance	—
$Z$	Number of items	—

## Greek Symbols

Symbol	Description	Unit
$\alpha$	Guide vane angle	$^{\circ}$
$\beta$	Blade angle	$^{\circ}$
$\eta$	Efficiency	—
$\lambda$	Turbine coefficient	—
$\mu$	Dynamic viscosity	$kg/(m \cdot s)$
$\phi$	Angle in spiral casing cross section	$^{\circ}$
$\pi$	Constant	—
$\rho$	Density	$kg/m^3$
$\sigma$	Bending stress	$MPa$
$\tau_w$	Wall shear stress	$Pa$
$\theta$	Angle in the radial view	$^{\circ}$
$\omega$	Angular velocity	$rad/s$
$\Omega$	Speed number	—

## Sub-symbols

$*$	Refers to best efficiency point of turbine
$e$	Refers to effective
$gv$	Refers to guide vane
$gvi$	Refers to guide vane inlet
$gvo$	Refers to guide vane outlet
$h$	Refers to hydraulic
$m$	Refers to meridional direction
$max$	Refers to maximum value
$min$	Refers to minimum value
$p$	Refers to particle
$poles$	Refers to generator pole pairs
$r$	Refers to runner
$sv$	Refers to stay vane
$svi$	Refers to stay vane inlet
$svo$	Refers to stay vane outlet
$u$	Refers to peripheral direction
$x$	Concentration exponent
$y$	Size exponent
0	Refers to where the guide vane axis is fixed
1	Refers to inlet of turbine runner
2	Refers to outlet of turbine runner
$\underline{x}$	Underline refers to reduced value

## Abbreviations

BEP	Best Efficiency Point
CFD	Computational Fluid Dynamics
FEM	Finite Element Method
FSI	Fluid Structure Interaction
GUI	Graphical User Interface
HEC	Hydroelectric Centre
IEC	International Electrotechnical Commission
KU	Kathmandu University
masl	Meters above sea level
mWc	Meters of Water column
NPSH	Net Positive Suction Head
NORAD	Norwegian Agency for Development Cooperation
NTNU	Norwegian University of Science and Technology
PL	Particle load
ppm	Parts per million
rpm	Revolutions per minute
SST	Shear Stress Transport



# 1 Introduction

## 1.1 Hydropower in Nepal

Nepal is an Asian country located in the Himalayas with borders to India and China. The topography is steep, ranging from the delta of Ganges to the peak of Mt. Everest. The country is blessed with access to large water resources from regular monsoon rain and glacier run-off, giving a great potential for hydropower. The estimated potential is 80 000 MW, out of which approximately 43 000 MW is economically feasible. Despite of this, only about 2 % of the economically feasible capacity has been exploited [6].

In March 2011, Nepalese government launched an ambitious four-year hydropower development plan to counter the energy crisis the country is facing. Today's load-shedding with around 12-hour power cuts a day affects the country's industry widely, forcing many industries to reduce operation or shut down. The new initiative is aiming for 2.500 MW of electricity by 2016, and reducing the load-shedding drastically. With new energy policies and reforms, this is intended to become a golden era for hydropower development in Nepal [7].

Hydropower development in the Himalayan region is however not as straight forward as in many other regions, due to the large amounts of sediments in the water streams. The sediment transport in the rivers reaches its peak during the monsoon period. Run-of-river hydropower plants then experience significant sediment induced turbine wear problems, causing loss in energy generation and frequent maintenance stops. One solution to reduce the sand erosion problem is to reduce the flow velocities through the turbine, as previous studies have shown a relation between the relative flow velocity and the erosion rate.

## 1.2 Jhimruk Hydroelectric Centre

The 12 MW run-of-river Jhimruk HEC is located in the Pyuthan District in the west of Nepal. Due to large amounts of quartz mineral particles in the Jhimruk River, the three turbines at Jhimruk have experienced severe erosion problems, demanding annual maintenance stops.

Most of the erosion damage occurs during the monsoon period. At Jhimruk about 83 % of the annual rainfall occur in this period. A sediment study indicates that the sediment concentration exceeds 4,000 ppm for about 15 % of the monsoon period. The average content of quartz in the sediments has been found to be above 60 % [6].



Figure 1.1: Map of Nepal with location of Jhimruk Hydro Electric Centre

### 1.3 Objective

This master thesis is a continuation of the author's project thesis aiming for a new design philosophy for Francis turbines operated in sand laden water. The objective of the thesis is to carry out the hydraulic design of a new Francis turbine with reduced velocity components. Matlab is used to generate runner blade geometries and for a first stage optimization. Furthermore, a coarse grid inviscid CFD analysis is used for a second stage optimization. Further optimization is needed before manufacturing of the turbines can be started.

### 1.4 Outline

The report starts with a brief comment on the hydropower potential in Nepal and a short introduction of the reference case, Jhimruk Hydro Electric Centre. Sediment erosion theory and models are presented in chapter three. Chapter four contains a review of traditional high head Francis turbine design theory according to the standard design approach at NTNU. This is the basis for the design software, which is explained in chapter five. Chapter six and seven gives an overview of selected topics concerning CFD. A reference design generated using the design software and analysed using CFD is presented in chapter eight. Further follows a parameter study with CFD results for selected designs, a discussion of the results and conclusion.



## 2 Background

### 2.1 *RenewableNepal* Program

*RenewableNepal* is a NORAD funded program supporting research based industrial development in Nepal. The project is jointly managed by SINTEF Energy Research and Kathmandu University, and provides funding support to research and development projects related to renewable energy technology.

One project going on with support from *RenewableNepal* is the *Development of Hydraulic Turbines with new Design Philosophy as a foundation for turbine Manufacturing in Nepal*. A description of the project can be found in the *RenewableNepal* web page [8]. NTNU and KU cooperate to establish a new Francis turbine design suitable to handle sediment erosion. The ultimate goal of the project is to start manufacturing of Francis turbines in Nepal. Hence, a parallel activity is to develop a manufacturer in Nepal.

This thesis is part of the project, aiming at reducing sediment erosion in Francis turbines by means of hydraulic design changes.

### 2.2 The Francis Turbine Design Team

At the beginning of the semester, the master students at the Waterpower Laboratory were divided into different teams. The Francis turbine design team consisted of me, Biraj Singh Thapa (*Hydraulic design of Francis turbine exposed to sediment erosion*), Helene P. Erichsen (*Mechanical design of Francis turbine exposed to sediment erosion*) and ph.d candidate Mette Eltvik (*Sediment erosion in Francis turbines*).

### 2.3 Earlier Work

A lot of papers and books on sediment erosion have been published. Only a few of these focus on sediment erosion in hydraulic machinery. Literature on design of Francis turbines is hard to retrieve. However, some literature on designing pump impellers is available, and the methods described there may be used for designing turbines as well.

Hermod Brekke, former NTNU professor, has performed quite a lot of research concerning sediment erosion in hydraulic machinery, both on design, material properties and development of sediment erosion resistant coatings. He has also contributed with a chapter in the book *Abrasive Erosion & Corrosion of Hydraulic Machinery* edited by Duan and Karelin.

During the last years the focus on sediment erosion at the Waterpower laboratory has increased. In 2004, Bhola Thapa finished his doctoral thesis *Sand Erosion in*

*Hydraulic Machinery*. Same year, Jonas Jessen Ruud wrote his master thesis on *Sediment handling problems at Jhimruk Power Plant*.

The procedure of proposing a new design of a Francis turbine with reduced velocity components in order to reduce the sediment erosion rate has been carried out by both Mattias Rögner in 2008 and by Hallvard Meland in 2010.

Ola Gjømle performed a CFD analysis and a stress analysis of the Francis turbine of Cahua power plant in Peru in his master thesis. Cahua power plant has experienced large sediment erosion problems. Cahua was also the reference case of the project assignment and master thesis of Mette Eltvik. She performed CFD analysis with two-phase fluid-particle flow on the Francis turbine. The results were compared with the erosion damage on the old turbines at Cahua.

In 2010, Hari Prasad Neopane finished his doctoral thesis *Sand Erosion in Hydro Turbines*. He performed experimental tests, CFD analysis (two-phase fluid particles) and field studies of sediment erosion. The doctoral theses of Neopane and Thapa are important contributions to the research field of sediment erosion in hydraulic machinery.

Some works on material properties have also been performed. Tests have shown a relation between the hardness of particles and hydraulic component material properties. Increasing the hardness of the components by e.g. ceramic coatings could considerably reduce the erosion damage. This is outside the scope of this thesis, and will not be discussed any further.

## 2.4 The Design Software

Programming a Francis turbine design software in Matlab was the main objective of the author's project assignment. This design software has been further developed and expanded as part of the master thesis. The theory behind the software is presented in chapter 4.

### 3 Sediment Erosion

A chapter from Helene P. Erichsen’s master thesis [10], containing supplementary theory about sediment erosion and some info about materials and ceramic coatings, is found in appendix A.

#### 3.1 Wear Mechanisms

Wear is a collective term of different mechanisms which cause material loss or deformation of solids. In general these mechanisms can be classified into three categories; mechanical, chemical and thermal actions [6]. This chapter focuses on the mechanical wear caused by sediments impinging on a solid surface. When speaking of hydraulic machinery, this wear is termed erosion.

Stachowiak and Batchelor [1] classifies erosion as either abrasive or erosive wear, depending on the contact between a particle and the surface. Abrasive wear occur when hard particles that are sliding, rolling or jumping along the surface at a lower velocity than the flow cut or scratch off material. Erosive wear is a result of material being removed when particles hit a surface with higher impact angle.

##### Abrasive wear

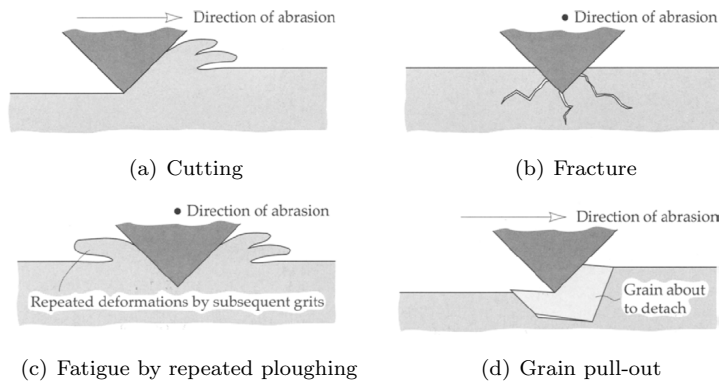


Figure 3.1: Mechanisms of abrasive wear [1]

Abrasive wear is a collective term of different wear mechanisms depending on both particle properties and wall material properties. The different mechanisms are illustrated in figure 3.1.

When a hard particle strikes the solid surface, material can be cut off and removed as wear debris, as illustrated in figure 3.1(a). For brittle materials, the impact can cause fractures and cracking (see figure 3.1(b)). Over time, accumulation of cracks

may result in loss of large quantities of material. For ductile materials, repeated ploughing will cause material deformation as illustrated in figure 3.1(c). Material is removed as a result of material fatigue. This is however a relatively slow process compared to the other processes described. Figure 3.1(d) illustrates detachment of grains. This is a rare form of abrasive wear, which is mainly found in very brittle materials like ceramics. When present, this is a rapid and damaging wear mechanism.

### Erosive wear

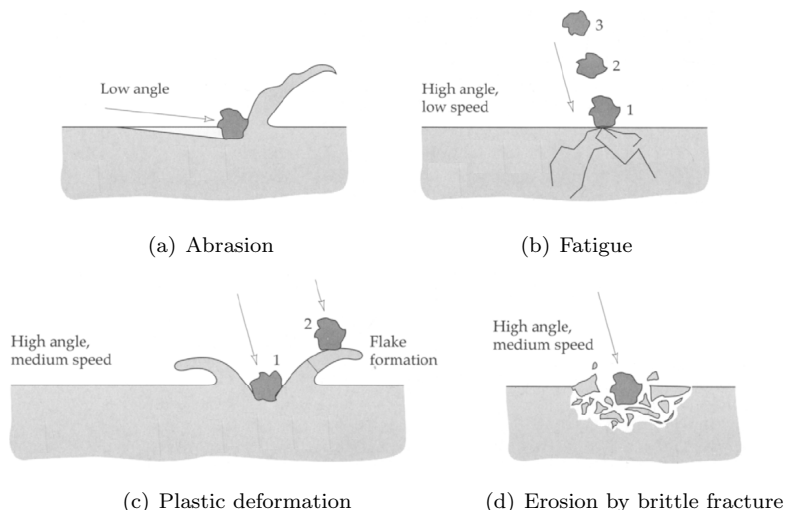


Figure 3.2: Mechanisms of erosive wear [1]

Suspended load in a fluid flow will cause different mechanisms of erosive wear depending on the impact angle and the speed of the particle. These mechanisms are illustrated in figure 3.2.

When a particle strikes the surface at a low impact angle, material is removed by a cutting action, as illustrated in figure 3.2(a). This is similar to the abrasive wear. Figure 3.2(b) illustrates particles hitting the surface at a large impact angle but at low velocity. In this case a single particle does not have enough kinetic energy to deform the surface material, but surface fatigue might occur if the striking is repeated. For particles with medium velocity and high impact angle, the erosion action depends on the surface material property. If the surface consists of a ductile material, particles hitting the surface may cause plastic deformation due to formation of flakes around the striking point. Material will detach as debris when a particle hit a flake. This is illustrated in figure 3.2(c). If the surface material is brittle, a fracture is likely to occur when sharp particles strike. The debris then detach from the material by surface cracking as figure 3.2(d) illustrates.

## 3.2 Sediment Erosion in Francis Turbines

The most severe erosion damage is found in areas with high velocities and/or accelerations [9]. These are illustrated in figure 3.3.

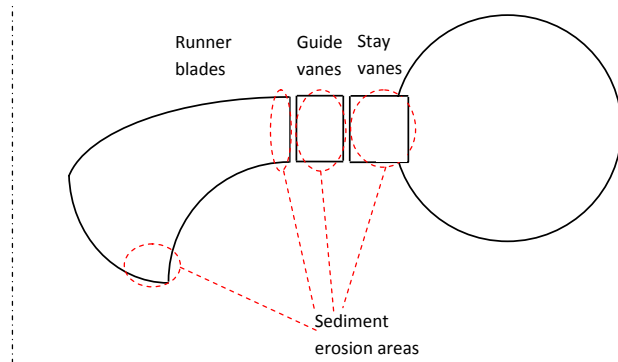


Figure 3.3: Areas exposed to sediment erosion wear

### Stay vanes

In the stay vanes, erosion occurs because secondary flows from the spiral casing causing incorrect flow angles at the inlet, and because of the high absolute velocity  $C$ . The erosion damage is worst close to the upper and lower cover. Modern spiral casing design, as shown in figure 3.4, reduces the propagation of secondary flows from the spiral casing into the stay vanes, and thus also the erosion damage.

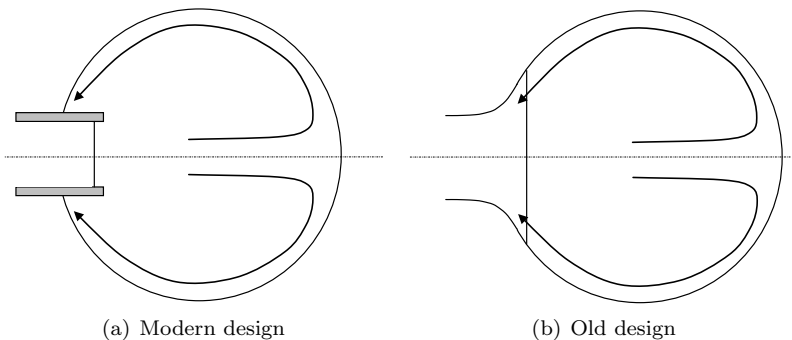


Figure 3.4: Design of stay vane inlet

## Guide vanes

The guide vanes experience erosion damage due to the high flow velocities and accelerations. Secondary flow in the corners between facing plates and guide vanes causes erosion of the facing plates along the guide vane contour. Leakage flows between guide vane and facing plates due to the pressure difference between pressure and suction side cause erosion on the guide vanes. Duan and Karelin [9] classifies erosion in the guide vanes into four categories:

- *Turbulence erosion* occur in the outlet region due to high velocities and small particles suspended in the flow. Severe turbulence erosion is also found on the facing plates.
- *Secondary flow erosion* occur in corners between facing plates and guide vanes due to horse shoe vortices around obstacles, like the guide vane inlet. This results in heavy erosion on the facing plates along the guide vane contour.
- *Leakage erosion* occur due to leakage flow through the clearance between guide vanes and facing plates. This causes material removal on both the facing plates and the guide vanes. The leakage flow will also increase the horse shoe vortex on the suction side of the guide vane.
- *Acceleration* of the main flow creates an acceleration of sand particles normal to the streamlines. This causes the particles to collide with the guide vane surface. The impacts of large particles ( $d_p > 0.5 \text{ mm}$ ) will normally cause heavy erosion damage.

Thapa [2] states that the small particles ( $d_p < 0.5 \text{ mm}$ ) will follow the streamlines longer than the larger particles. Thapa illustrates this in a Pelton turbine bucket, as shown in figure 3.5, but it is assumed that the same effect might occur in Francis turbines as well. Typical erosion on guide vanes are shown in figure 3.6.

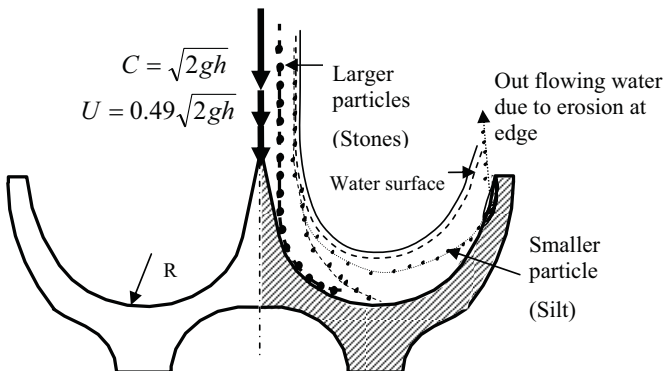


Figure 3.5: Illustration of particle-flow separation at high acceleration [2]

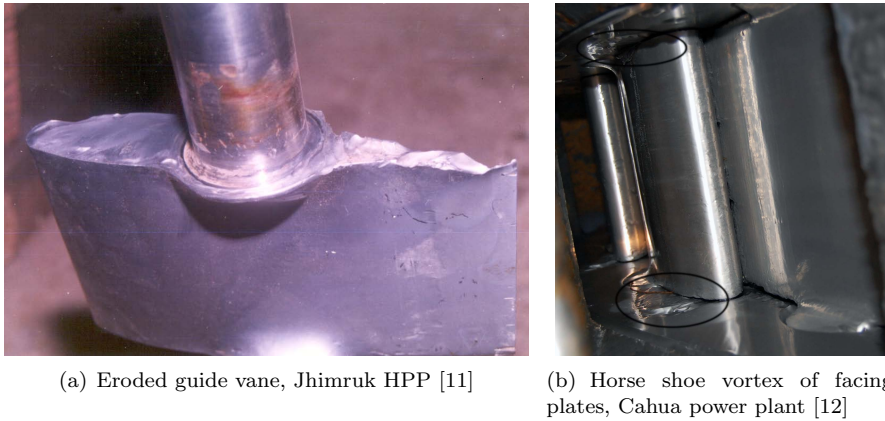


Figure 3.6: Erosion in guide vanes

## Runner

A vortex is created due to the leakage flow between the cover and the guide vane facing surface and the secondary flow, as illustrated in figure 3.7. This occurs both at the top and at the bottom of the guide vanes. These two vortices hit the runner inlet, and cause erosion at the top and at the bottom of the runner leading edge. This can be seen in figure 3.8(a).

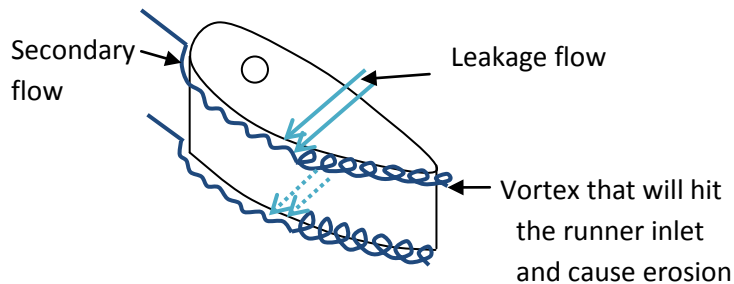


Figure 3.7: Vortex from guide vanes causing erosion at runner inlet

The highest relative velocity in the turbine is found at the runner outlet, close to the shroud. This causes turbulence erosion to occur. In addition, the runner outlet area is subject to cavitation wear if subject to low pressure. Synergy between cavitation and sediment erosion can accelerate the wearing process considerably. Typical erosion damage at runner outlet is shown in figure 3.8(b).



(a) Erosion damage at runner inlet, Cahua power plant [12] (b) Erosion damage at runner outlet, Jhimruk HEC [11]

Figure 3.8: Erosion in runners

### 3.3 Parameters Influencing the Erosion Rate

Erosion rate depends on flow conditions, particle characteristics and surface material properties [2]. At low velocities, a particle does not have enough kinetic energy to cut the turbine surface, although surface fatigue may occur if particle striking is repeated. This is valid for all velocities below a certain velocity, referred to as a critical velocity. This critical velocity depends on both surface properties and characteristics of the particles, like size, shape and hardness. At velocities above the critical velocity, both cutting and plastic deformation of the surface may occur.

The impact angle is the angle between the particle trajectory and the wall surface, as illustrated in figure 3.9. The impact angle is sometimes referred to as the impingement angle. For ductile materials, the erosion is most severe at low impact angles, whereas the erosion is more severe at high impact angles for brittle materials [13]. Surface morphology and material characteristics like elasticity, hardness and chemistry are referred to as surface properties.

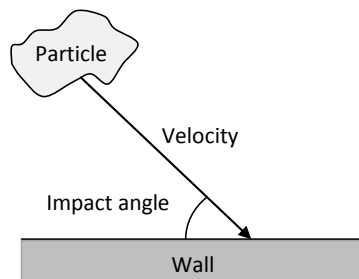


Figure 3.9: Impact angle



### 3.4 Erosion Classification

Duan and Karelin [9] states that sediment erosion in hydro turbines may be classified into three subcategories:

- *Micro erosion* occur due to small particles ( $d_p < 60 \mu m$ ) at high velocities gaining a high rotational velocity by boundary layer turbulence and thus inducing abrasive erosion on the surfaces, especially in the runner outlet region.
- *Secondary flow vortex erosion* occur due to secondary flow in corners and due to horse shoe vortices around obstacles, like the guide vane shafts. This kind of erosion is caused by a combined effect of boundary layers and change of flow acceleration.
- *Acceleration* of large particles ( $d_p > 0.5 mm$ ) normal to the streamlines cause the particles to collide with the walls.

Bardal [13] also divides erosion into three subcategories similar to the ones classified by Duan and Karelin:

- *Impingement erosion* occurs for two-phase flows changing flow direction as particles then hit the material surface.
- *Turbulence erosion* occur in areas with strong flow accelerations. This is typically found at the outlet of an inner curve of a bend, and thus also at the outlet of a runner close to the shroud.
- *Wear and tear* due to particles flowing along and in contact with the surface.

### 3.5 Erosion Models

According to Truscott [14], several authors have given simple expressions for erosion rate as a function of velocity and particle properties based on wear test results. The most often quoted expression is

$$Erosion \propto Velocity^i \quad (3.1)$$

where  $i$  may vary depending on material properties, but most commonly is close to three.

#### Bergeron's model

Not all models considered by Truscott are suitable for hydraulic machinery, as they were developed for other conditions. However, Truscott also presents a more complicated expression of wear rate adjusted for hydraulic machinery which was

developed by Bergeron.

$$Erosion \propto \frac{W^3 \cdot (\rho_p - \rho_w) \cdot D_p^3 \cdot p \cdot K}{D} \quad [-] \quad (3.2)$$

where  $K$  is an experimental coefficient dependent on the abrasive nature of particles.

### Tsuguo's model

Another relation of erosion rate worth mentioning is the one established by Tsuguo [15]. This model is based on 8 years of erosion data from 18 hydropower plants, while most of the other models are based on laboratory tests. Tsuguo's model gives the erosion rate measured as loss of thickness per unit time.

$$Erosion = \lambda \cdot K_{concentration}^x \cdot K_{size}^y \cdot K_{shape} \cdot K_{hardness} \cdot K_{material} \cdot W^i \quad [mm/year] \quad (3.3)$$

where  $K_{concentration}$  is the concentration of suspended sediments,  $K_{size}$  is the average particle size coefficient,  $K_{shape}$  is the coefficient of shape of particle,  $K_{hardness}$  is the coefficient of hardness of particles and  $K_{material}$  is the abrasion resistance coefficient of surface material. All  $K$ 's are non-dimensional constants.

### The IEC model

The International Electrotechnical Commission (IEC) recommends the following theoretical model of abrasion rate in order to demonstrate how different critical aspects influence the particle erosion rate in the turbine [16].

$$dS/dt = f(\text{particle velocity, concentration and physical properties, flow pattern, turbine material properties and other factors})$$

However, it is not known how the listed variables interact with each other, and thus several simplifications are introduced. Most importantly, all the variables in the model are considered independent. This simplification is not proven, but based on literature studies and experience. For hydraulic machinery, IEC suggests the following expression

$$S = W^3 \cdot PL \cdot K_{material} \cdot K_{flow} \quad [mm] \quad (3.4)$$

where  $K_{material}$  is the turbine material factor and  $K_{flow}$  is the flow factor.

### Tabakoff's model

Tabakoff's model gives the erosion rate as the eroded wall material divided by the mass of the particles [17]. A non-dimensional mass  $M$  is found as in equation 3.5:

$$M = k_1 \cdot f(\gamma) \cdot V_p^2 \cdot \cos^2 \gamma \cdot (1 - R_T^2) + f(V_{PN}) \quad (3.5)$$

where

$$f(\gamma) = \left( 1 + k_2 \cdot k_5 \cdot \sin \left( \gamma \frac{\pi/2}{\gamma_0} \right) \right)^2 \quad (3.6)$$

$$R_T = 1 - k_4 \cdot V_P \cdot \sin \gamma \quad (3.7)$$

$$f(V_{PN}) = k_3 \cdot (V_P \cdot \sin \gamma)^4 \quad (3.8)$$

$k_1$  to  $k_5$  and  $\gamma_0$  are model constants which depend on the particle/wall material combination.  $V_P$  is the particle impact velocity and  $\gamma$  is the impact angle in radians.

Tabakoff's erosion model is implemented in the Ansys CFX solver, and might thus be used to predict the erosion rate in the CFD analyses. The total erosion rate found from CFX is defined as:

$$\text{Total Erosion Rate} = M \cdot \dot{N} \cdot m_p \quad [kg/m^2s] \quad (3.9)$$



## 4 Francis Turbine Design

This chapter presents the theory basis for the design software. The design method is to a large extent based on the method most commonly used at the Waterpower Laboratory, but with some exceptions where other methods are found more suited and with more correct results. Most of this chapter is taken from the authors project thesis [18]. The chapter is included to give an assembled presentation of the design software theory basis. In addition, the software has been extended and revised with minor and major changes, hence new theory is prevailing. Sections 4.2, 4.3 and 4.5 contain new or revised paragraphs.

Alternative design procedures are hard to retrieve from turbine producers, as this is considered as classified information. However, designing a pump impeller is similar to designing a Francis turbine, and pump impeller design can be reviewed in Stepanoff [19] and Lazarkiewicz [20].

### 4.1 Introduction

A traditional Francis turbine consists of a runner, a set of guide vanes, a set of stay vanes and a spiral casing, as shown in figure 4.1. The design process starts with the runner and moves outwards, ending with the spiral casing.

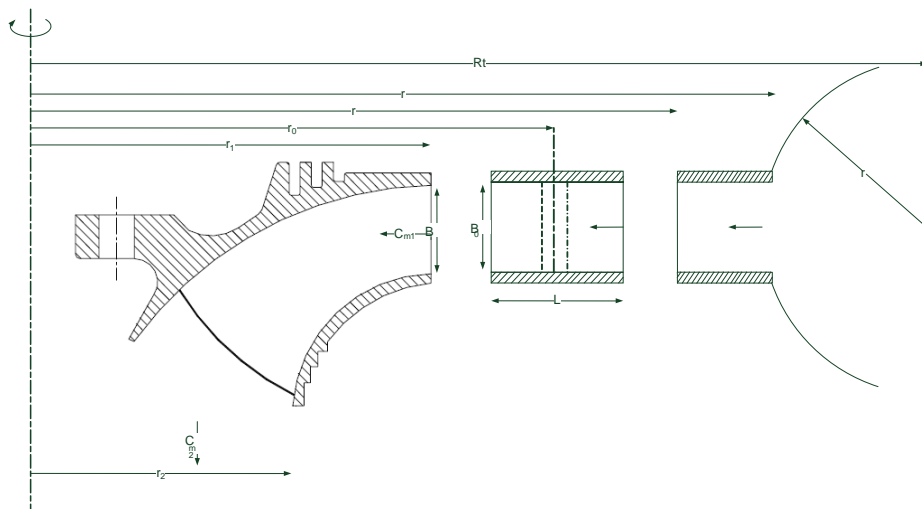


Figure 4.1: Axial view of a turbine [3]

## 4.2 Main Dimensions

Designing a Francis runner starts with calculating the main dimensions. These are based on hydraulic parameters like head  $H_e$  and discharge  $Q$ , which are determined by the topography and hydrology of the power plant site. Traditionally, velocity triangles at the inlet and outlet of the runner, as shown in figure 4.2, are used in the design process.

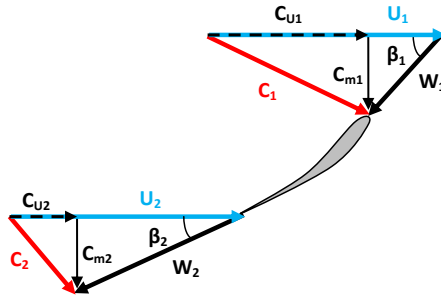


Figure 4.2: Velocity triangles

### Dimensions at runner outlet

As a first attempt, the outlet angle  $\beta_2$  and peripheral speed  $U_2$  can be chosen based on empirical data. Brekke [21] states that for traditional Francis runners these values are usually found in the intervals

$$15^\circ < \beta_2 < 22^\circ \quad (4.1)$$

$$35 \text{ m/s} < U_2 < 42 \text{ m/s} \quad (4.2)$$

where  $\beta_2$  takes lower values for higher heads and  $U_2$  takes higher values for higher heads. The listed intervals should not be considered fixed limits, especially when designing turbines that will be operated in silty water. Measurements at Jhimruk show that the existing runners have a lower outlet peripheral speed than what traditionally is suggested.

At best efficiency point (BEP) no swirl in the draft tube has to be assumed. Hence the peripheral component of the absolute velocity,  $C_{u2}$ , equals zero, and the meridional component of the absolute velocity can be found from the velocity triangles.

$$C_{m2} = U_2 \cdot \tan \beta_2 \quad [m/s] \quad (4.3)$$

With these parameters the outlet diameter  $D_2$  can be calculated from continuity.

$$D_2 = \sqrt{\frac{4Q}{\pi \cdot C_{m2}}} \quad [m] \quad (4.4)$$

However, this is only strictly valid for infinitely thin blades: Due to the thickness of the blades at the trailing edge, the effective outlet area will be smaller. To find a rough estimate of the outlet area, the number of blades and the thickness of the blade at the trailing edge have to be decided or guessed. Because of the outlet blade angle  $\beta_2$ , the lost area must be approximated as the projection of the blade thickness in the outlet plane, as shown in figure 4.3.

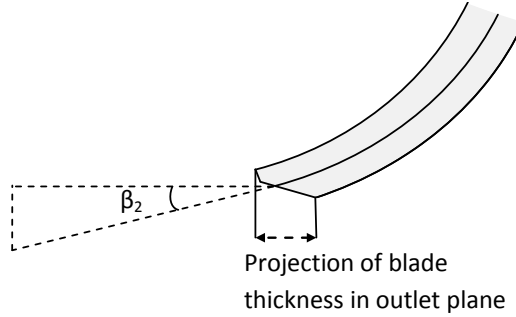


Figure 4.3: Projection of the blade thickness into the outlet plane

Choosing to keep the value of  $D_2$ , the  $C_{m2}$  value is recalculated taking the lost area into account. However, because  $\beta_2$  is dependent on  $C_{m2}$ , a small iteration loop is necessary to fulfil the no swirl condition.

Knowing  $D_2$ , the rotational speed of the turbine can be calculated according to equation 4.5.

$$n = \frac{U_2 \cdot 60}{\pi \cdot D_2} \quad [rpm] \quad (4.5)$$

The grid frequency in Nepal is 50 Hz. In order to obtain a frequency of 50 Hz, the generator rotor has to pass 50 pole pairs in the stator per second.

$$Z_{poles} = \frac{f_{grid} \cdot 60}{n} \quad [-] \quad (4.6)$$

The number of pole pairs has to be an integer. To fulfil this requirement, the rotational speed has to be corrected to the corresponding synchronous speed found by rearranging equation 4.6. The designer has to choose whether to round up or down the number of pole pairs. Choosing a higher  $Z_p$  yields a larger and slower rotating turbine. According to Verma [22], the sediment erosion damage is less in large machines than in smaller ones. By selecting the speed of rotation one or two steps lower than for turbines operated in clean water, the machine size is increased. Thus the relative flow velocities are reduced with consequently less erosion damage.

## Dimensions at runner inlet

When the outlet dimensions are set, the inlet of the runner is to be designed. The designer chooses the inlet peripheral speed, and with that the inlet diameter as well.

$$D_1 = \frac{U_1 \cdot 60}{n \cdot \pi} \quad [m] \quad (4.7)$$

It is convenient to use *reduced values* in the design process because the reduced velocities are dimensionless. The reduced values are denoted by an underscore.

$$\underline{U}_1 = \frac{U_1}{\sqrt{2 \cdot g \cdot H_e}} \quad [-] \quad (4.8)$$

The Euler equation is commonly used for turbine design, and is defined as shown in equation 4.9.

$$\eta_h = \frac{C_{u1} \cdot U_1 - C_{u2} \cdot U_2}{g \cdot H_e} \quad [-] \quad (4.9)$$

By introducing reduced values and including the assumption of no swirl flow in the draft tube at BEP, the Euler turbine equation reduces to:

$$\eta_h = 2 \cdot \underline{U}_1 \cdot \underline{C}_{u1} \quad [-] \quad (4.10)$$

It is common to assume a hydraulic efficiency  $\eta_h$  of 96 % for the runner.

In order to avoid back flow in the runner, an acceleration of the flow through the runner is desirable. Generally, ten percent is chosen, but this is up to the designer.

$$C_{m2} = \left(1 + \frac{Acc}{100}\right) \cdot C_{m1} \quad [m/s] \quad (4.11)$$

The inlet area can now be found according to continuity.

$$C_{m1} \cdot A_1 = C_{m2} \cdot A_2 \quad (4.12)$$

As was done at the outlet, the runner blade thickness has to be accounted for also at the inlet. The inlet diameter is fixed due to equation 4.7, so the blade thickness will only affect the runner inlet height  $B_1$ , as shown in equation 4.13. By combining equations 4.11 and 4.12, the inlet height can be calculated as

$$B_1 = \frac{A_1}{\pi \cdot D_1 - Z_{blades} \cdot \frac{t_{LE}}{\sin \beta_1}} \quad [m] \quad (4.13)$$

where  $\beta_1$  is found from equation 4.14.

$$\tan \beta_1 = \frac{C_{m1}}{U_1 - C_{u1}} \quad [-] \quad (4.14)$$



## Submerging the turbine

If the water pressure in the runner is lower than the vapor pressure, cavitation may occur. The impact of gas cavities collapsing close to the wall surface causes cavitation erosion. In order to avoid the water pressure to drop below the vapor pressure, the turbine can be submerged. The required level of submergence, expressed as Net Positive Suction Head (NPSH) depends on the main dimensions and the speed number  $\Omega$  of the runner. The speed number is a non-dimensional expression for rotational speed at a given head at BEP.

$$\Omega = \underline{\omega} \cdot \sqrt{*Q} \quad [-] \quad (4.15)$$

Knowing the speed number, the required NPSH can be calculated as

$$\text{NPSH}_{\text{required}} = a \frac{C_{m2}^2}{2 \cdot g} + b \frac{U_2^2}{2 \cdot g} \quad [mWc] \quad (4.16)$$

where the parameters  $a$  and  $b$  are empirical constants, and, according to Brekke [21], dependent on the speed number.

$$\Omega < 0.55 \quad \text{gives } a=1.12 \text{ and } b=0.055$$

$$\Omega > 0.55 \quad \text{gives } a=1.12 \text{ and } b=0.1 \cdot \Omega$$

NPSH has to fulfil the following requirement to avoid cavitation

$$\text{NPSH}_{\text{required}} < h_{atm} - h_{va} - H_s \quad [mWc] \quad (4.17)$$

where

$h_{atm}$  - atmospherically pressure, 1 atm = 10.3 mWc

$h_{va}$  - vapor pressure

$H_s$  - submerging of the turbine. A negative value of  $H_s$  implies that the turbine is set below tail water level.

Runners are often designed for high velocities to keep the dimensions down. This results in low water pressures and possible cavitation damage. A turbine designed with low velocity components to reduce the sediment erosion is likely to have larger dimensions than a traditional Francis runner, and hence possibly less cavitation problems.

Traditionally, turbines are designed based on head and flow, assuming sediment free water. Experiments have shown that components, which are cavitation free when operated in clean water, cavitates when operated in silty water [23].

The required submergence is calculated based on the vapour pressure of clean water. The viscosity of silty water is higher than for clean water, hence the vaporizing pressure is higher as well. This causes cavitation to occur at higher pressure levels for silty water than for clean water operation [24].

In addition, sediment erosion and cavitation are inducing each other. An already cavitation pitted surface is more prone to sediment impacts, which intensifies the damage. Likewise, a sediment eroded surface has local flow conditions which induce cavitation at an earlier stage than in clean water, and hence accelerates the damage mechanism vastly.

A deeper submergence of the turbine will avoid cavitation erosion, and thus also the 'cavitation - sediment erosion' synergy. The extent of the additional required submergence is dependent on several parameters, including concentration and size of the particles.

### 4.3 Runner Blades

When the main dimensions of the runner are known, the runner blades can be designed. The design procedure starts by determining the shape of the blade in the axial view, then the radial view is established, and finally the runner blade can be plotted in three dimensions.

#### Runner axial view

At first a streamline along the shroud or along the hub has to be defined. It is most common to define it along the shroud. Traditionally an elliptical or circular shape is chosen for the streamline.

After the first streamline is defined, the number of streamlines has to be chosen. The distribution of streamlines is determined by the velocity profile at the inlet of the runner, which initially is considered uniform. This gives a uniform distribution of the streamlines between the hub and shroud at the inlet.

Based on the inlet distribution and the definition of the first streamline, the rest of the streamlines can be determined. A point  $i$  on streamline  $j + 1$  is found by drawing a line between the points  $(i + 1, j)$  and  $(i - 1, j)$ . Then the new point,  $(i, j + 1)$ , is placed on an axis orthogonal to this line going through point  $(i, j)$ , as shown in figure 4.4.

From figure 4.4 the following expressions can be derived:

$$\alpha_{i,j} = \tan^{-1} \left( \frac{Z_{i-1,j} - Z_{i+1,j}}{R_{i-1,j} - R_{i+1,j}} \right) \quad [-] \quad (4.18)$$

$$r_{i,j} = \frac{R_{i,j} + R_{i,j+1}}{2} \quad [m] \quad (4.19)$$

$$A_{i,j} = 2\pi \cdot r_{i,j} \cdot b_{i,j} \quad [m] \quad (4.20)$$

$$b_{i,j} = \frac{R_{i,j+1} - R_{i,j}}{\sin \alpha_{i,j}} \quad [m] \quad (4.21)$$

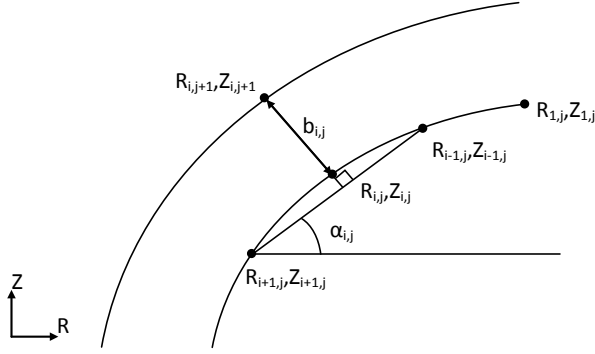


Figure 4.4: Determining a new point on a streamline. Adapted from Eltvik et al. [3]

Combining equation 4.19-4.21 yields:

$$A_{i,j} = 2\pi \left( \frac{R_{i,j+1} + R_{i,j}}{2} \right) \left( \frac{R_{i,j+1} - R_{i,j}}{\sin \alpha_{i,j}} \right) = \frac{\pi}{\sin \alpha_{i,j}} (R_{i,j+1}^2 - R_{i,j}^2) \quad [m^2] \quad (4.22)$$

Expression equation 4.22 can be rearranged to:

$$R_{i,j+1} = \sqrt{R_{i,j}^2 + \frac{A_{i,j} \sin \alpha_{i,j}}{\pi}} \quad [m] \quad (4.23)$$

Finally, the  $Z$  coordinate can be found:

$$Z_{i,j+1} = Z_{i,j} - b_{i,j} \cos \alpha_{i,j} \quad [m] \quad (4.24)$$

A common issue when defining the first streamline along the shroud is that the streamlines close to the hub curve upwards at the inlet instead of going in a straight line, bending down towards the outlet. This is an undesirable design feature that must be corrected before proceeding with the design.

Starting with the first streamline along the hub avoids the problem with upward curvature, but it causes other problems, such as lines crossing each other at the inlet, which could result in numerical problems.

Considering these issues, a more general shape of the first streamline would be desirable. Then the problems of upward curvature could be avoided, even when starting from the shroud. An example of a more general curve definition is the Bezier curve.

When the curvature issue has been corrected, the design may need some further adjustments if the runner blades are too close to the centre of the shaft. Removing some of the endpoints on each streamline will solve this problem. If the endpoints

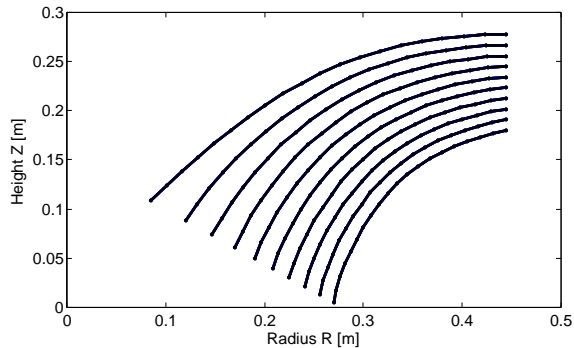


Figure 4.5: Axial view of the runner blade after cutting endpoints and redistributing the remaining points

are removed, the rest of the points should be redistributed with equal spacing. Figure 4.5 show the axial view of a Francis runner after removing upward curvature at the hub, cutting endpoints and redistributing the remaining points. If constraints exist for the outlet diameter, it has to be checked that the outlet diameter after cutting endpoints does not exceed the limits.

### Runner radial view

In order to simplify the design process of going from the axial view to the radial view, a  $GH$ -plane is defined.  $G$  is the length of a streamline in the axial plane and  $H$  is the length of a streamline in the radial plane.

The  $GH$ -plane is commonly used when designing centrifugal pump impellers, as described by both Stepanoff [19] and Lazarkiewicz [20].

Calculating the values of  $G$  is an easy and straight forward process, using the values of  $R$  and  $Z$  from the axial view.  $G$  equals zero at the inlet.

$$G_{i,1} = G_{i-1,1} + \sqrt{(R_{i-1,1} - R_{i,1})^2 + (Z_{i-1,1} - Z_{i,1})^2} \quad [m] \quad (4.25)$$

Calculating the values of  $H$  is more demanding, as they are dependent on the distribution of the blade angle,  $\beta$ . The blade angle is closely linked to the energy distribution along the blade. The energy distribution is often referred to as the  $U \cdot C_u$  distribution, and describes the transformation from pressure energy to rotational energy along the blade. The relation between the energy distribution and the blade angle  $\beta$  is governed by equation 4.26.

$$\beta = \arctan\left(\frac{C_m}{U - C_u}\right) \quad [^\circ] \quad (4.26)$$

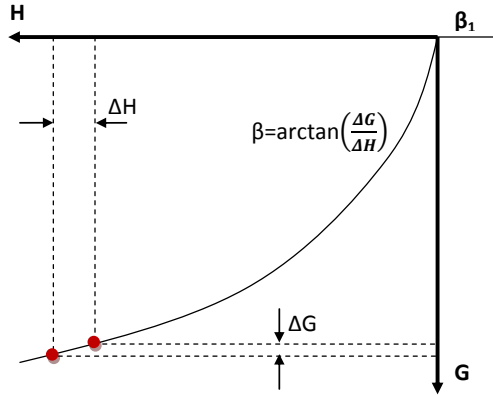


Figure 4.6: Definition of  $G$ - $H$  plane. Adapted from Eltvik et al. [3]

The blade angles at the inlet and outlet are known from the velocity triangles. The distribution in between has to be determined. This can be done in two ways. Either you can choose the  $U \cdot C_u$  distribution and then calculate the  $\beta$  distribution, or you can choose  $\beta$  and then calculate  $U \cdot C_u$ . Choosing the blade angle distribution gives the designer full control of the design outcome, and avoids any strange designs. Choosing the energy distribution and subsequently calculating the blade angle distribution, you gain the advantage of controlling the energy distribution, but you lose the control of the blade angle, and thus some strange designs may occur. A good practice is to control the corresponding distribution afterwards, either if the energy or the blade angle distribution is chosen. A distribution must be specified for each streamline, but you could of course specify the same distribution for all streamlines. The same  $U \cdot C_u$  distribution for all streamlines will give a different distribution of the blade angle for each streamline. Likewise, equal blade angle distribution for all streamlines will give a different energy distribution for each streamline. The corresponding distributions are calculated using equation 4.26.

$C_m$  is the velocity along the streamline, and is found using the continuity equation. The peripheral velocity  $U$  is dependent on the radius  $R$  and the angular velocity  $\omega$  and is thus known for each point.

$$U = \omega \cdot R \quad [m/s] \quad (4.27)$$

Next the values of  $\Delta H$  can be obtained using equation 4.28, defined as shown in figure 4.6.

$$\Delta H = \frac{\Delta G}{\tan \beta} \quad [m] \quad (4.28)$$

When this is performed for each streamline, the  $G$ - $H$  plane can be plotted. The radial view is established using equation 4.29, which is defined according to figure 4.8.

$$d\theta = \frac{\Delta H}{R} \quad (4.29)$$

When knowing all the coordinates for  $\theta$  and  $R$ , the radial view can be plotted as in figure 4.9.

Combining the axial coordinates and the radial coordinates, the 3D shape of the runner blade emerges as shown in figure 4.10.

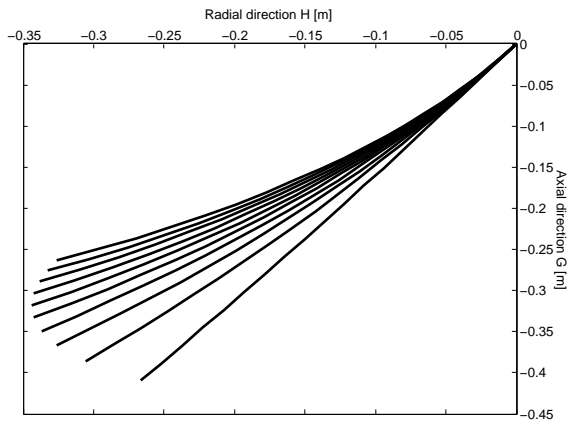


Figure 4.7: GH-plane

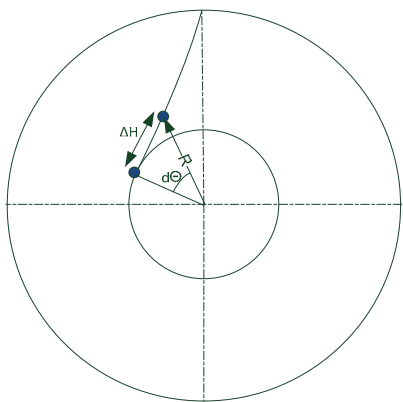


Figure 4.8: Definition of  $\theta$

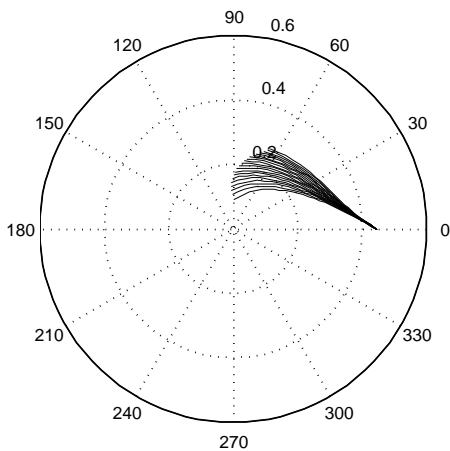


Figure 4.9: Radial view

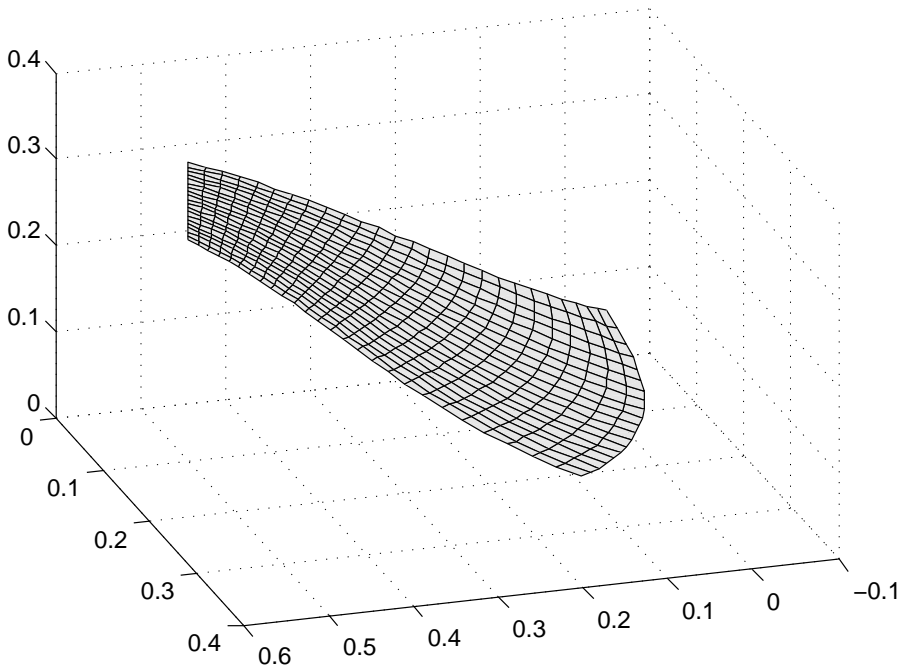


Figure 4.10: 3D-blade plotted without thickness

## 4.4 Runner

This section presents simplified methods for calculating the required number of blades in the runner and the required runner blade inlet thickness. We have however already guessed both number of blades and thickness at the leading and trailing edges in order to find the effective outlet and inlet areas of the turbine when deciding the main dimensions.

It seems that the method for calculating number of blades is excessively conservative, giving a very high number of blades. Furthermore the calculation of the blade thickness is not suitable for turbines where sediment erosion is expected. Then it makes sense to have thicker blades.

### Number of blades in the runner

When the shape of the blade is established, the number of blades in the runner has to be decided. This is done by investigating equation 4.30

$$\frac{\partial w}{\partial n} = -2\omega - \frac{w}{r_{curv}} \quad [1/s] \quad (4.30)$$

where  $r_{curv}$  is the radius of curvature of the blade surface.

The equation is derived from the balance of forces acting on a particle in a rotating channel, and describes the change in relative velocity,  $w$ , along a line,  $n$ , normal to the streamlines in the channel.

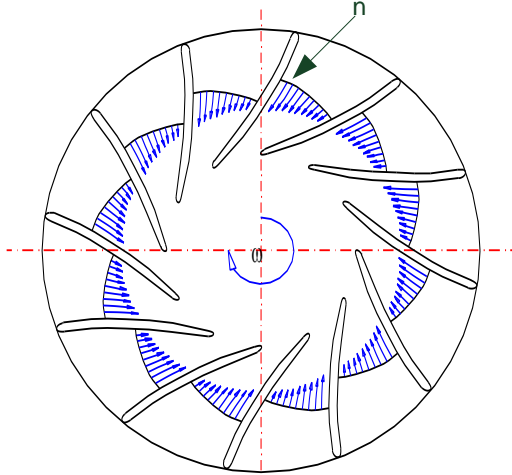


Figure 4.11: Relative velocity in rotating channel [4]

As can be seen from figure 4.11, the lowest relative velocity appears on the pressure side of the blade. To avoid backflow, the relative velocity at the pressure side cannot be negative.

In general, the  $-2\omega$  term is relatively much larger than the  $\frac{w}{r_{curv}}$  term in equation 4.30, and thus we can conclude that the value of  $\frac{\partial w}{\partial n}$  will be close to constant. That will give a velocity profile which is almost linear. For calculation purposes, the profile is assumed to be entirely linear.

$$\frac{\partial w}{\partial n} = \frac{\Delta w}{\Delta n} \quad (4.31)$$

Solving for  $\Delta n$ :

$$\Delta n = \frac{1}{\frac{\partial w}{\partial n}} \Delta w = const \cdot \Delta w \quad (4.32)$$

$\Delta n$  is the distance from the middle of the channel to the blade. The relative velocity increases with the flow rate, and the maximum relative velocity is found at full load, as can be seen in figure 4.12. As a decrease in  $\Delta w$  will cause narrower channels, and consequently an increased number of blades required, the dimensioning case for the number of blades will be found at part load. At some point on part load, backflow has to be allowed, and this limit has to be decided. This is, according to Dahlhaug [25, Personal conversations], typically set to 80 percent of the flow rate at design load.



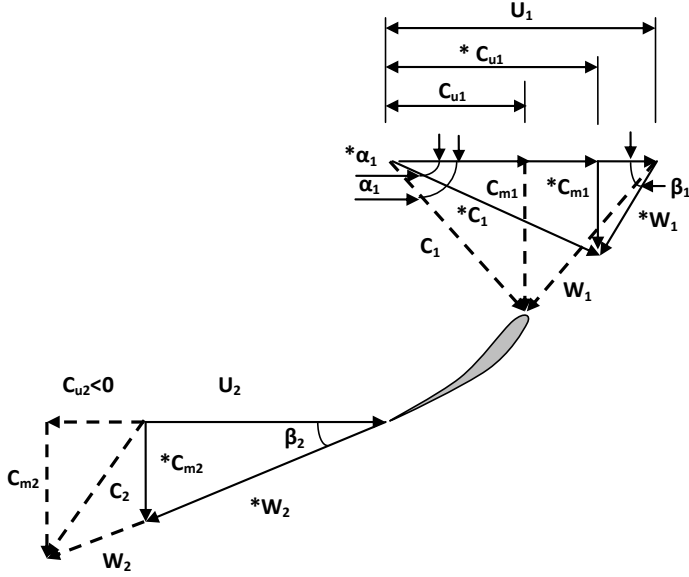


Figure 4.12: Velocity diagram at BEP (\*) and at full load

To calculate the least number of blades required to avoid backflow at the inlet, the relative velocity is set to zero at the inlet on the pressure side. The relative velocity in the middle of the channel is calculated based on the flow rate at 80 percent part load,  $Q_{80}$ . As the exact behavior of the  $C_u$  component is hard to calculate, it is in the design process assumed to obtain the same values as at design load. The peripheral speed is the same as on design load and the  $C_m$  component is found from continuity. Thus the relative velocity is found from the velocity triangles, and  $\frac{\partial w}{\partial n}$  is calculated from equation 4.30. Next, the distance from the center of the channel to the pressure side,  $\Delta n$ , is found from equation 4.32.

The distance between two blades are  $2\Delta n$ . The circumference of the runner is known from the main dimensions. Hence the least number of blades to avoid back flow is:

$$Z_{rb} = \frac{\text{Circumference}}{\text{Channel Width}} = \frac{\pi D_1}{2\Delta n} \quad [-] \quad (4.33)$$

This calculation of number of blades should be checked with CFD analysis, as the blade thickness is not accounted for, and because of the assumption of a linear velocity distribution and the simplification of the behavior of the  $C_u$  component. The simplification of the  $C_u$  component is discussed in the further work section.

## Thickness of blades

After the number of blades in the runner is determined, the thickness of each blade can be calculated. The thickness has to be large enough to withstand the hydraulic forces which the blade is exposed to, being the static pressure difference between the pressure and the suction side of the blade, and the dynamic pressure pulsations.

As the geometry of the runner blades are quite complex, a simplified stress analysis is performed to calculate a conservative estimate of the required blade thickness. Modeling the blade as a straight beam between hub and shroud, classical mechanics is applicable. The hub is considered to be rigid, while the shroud is assumed to be flexible in torsion with respect to the hub. This means that the blade can be modelled as a beam that is clamped at the hub side and guided at the shroud side.

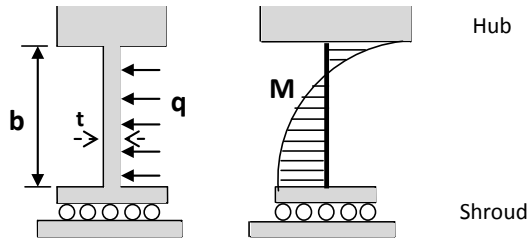


Figure 4.13: Blade modeled as a straight beam between hub and shroud

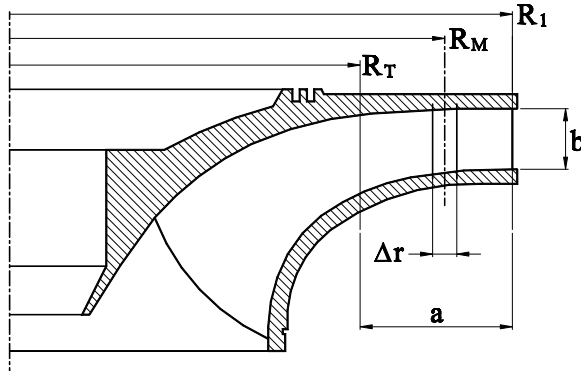


Figure 4.14: Definition of  $a$ ,  $b$ ,  $\Delta r$  and  $R_M$

Assuming equally distributed load,  $q = \Delta r \Delta p$ , the bending moment,  $M$ , is found as [26]

$$M = q \frac{b^2}{3} \quad [Nm] \quad (4.34)$$

The maximum bending stress,  $\sigma_{max}$ , is

$$\sigma_{max} = \frac{M t}{I} \frac{1}{2} \quad [Pa] \quad (4.35)$$

with blade thickness,  $t$ , and second area moment of inertia,  $I$

$$I = \frac{\Delta r t^3}{12} \quad [m^4] \quad (4.36)$$

Rearranging equation 4.34 - 4.36 gives the minimum blade thickness at the inlet as

$$t_{min} = \sqrt{\frac{2b^2 \Delta p}{\sigma_{max}}} \quad [m] \quad (4.37)$$

The pressure difference is calculated from the torque on the runner. The length  $a$  defined in figure 4.14, is an imaginary length where it is assumed that the entire torque is transferred from the flow to the blade. The value of  $a$  is usually set to  $1.5 b$  according to Brekke [21].

$$M_{runner} = Z_r a b R_M \Delta p = \frac{P}{\omega} \quad [Nm] \quad (4.38)$$

$$\Delta p = \frac{P}{Z_r a b R_M \omega} \quad [Pa] \quad (4.39)$$

## 4.5 Leading and trailing edge

The shape of the leading and trailing edge are designed based on experience as shown in figure 4.15 [27, personal conversation]. The trailing edge shape is chosen in order to minimize the amplitude of von Karman vortices.

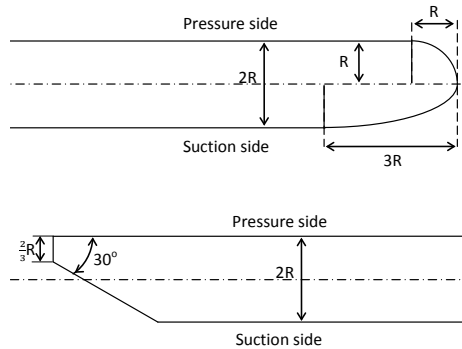


Figure 4.15: Shape of leading and trailing edge

## 4.6 Guide vanes

A number of adjustable blades, known as guide vanes, govern the discharge and the direction of the flow before it enters the runner.

The number of guide vanes has to be chosen. To minimize the extent of the pressure pulsations that occur when the runner vanes pass the guide vanes, the number of guide vanes has conform to equation 4.40.

$$\frac{\text{Number of Guide vanes}}{\text{Number of Runner vanes}} \neq \text{Integer} \quad (4.40)$$

To have sufficient distance between the guide vane and the runner, it is common to design the guide vanes outlet diameter at rated power approximately five percent larger than the runner inlet diameter. The gap between the guide vane outlet and the runner inlet is less at full power, and it should be controlled that there is sufficient clearance also at this guide vane position.

As flow in the gap between the guide vane outlet and the runner inlet is unaffected, the free vortex theory is used to find the tangential component of the absolute velocity at the trailing edge of the guide vanes.

$$C_{u1}r_1 = C_{ugvo}r_{gvo} = \text{Constant} \quad (4.41)$$

The meridional component is found using continuity and the guide vane outlet angle is found from the velocity triangle.

$$\tan \alpha_{gvo} = \frac{C_{mgvo}}{C_{ugvo}} \quad [-] \quad (4.42)$$

Next, the radial position of the guide vane axis,  $r_0$ , has to be determined. When  $r_0$  is known, the length from the trailing edge to the axis of the guide vane,  $L_0$ , is found from the law of cosine.

The length of the guide vane is dependent on the number of vanes, as the vanes have to overlap in the closed position. This is to avoid the vane from being able to rotate full circle. It is common to have an overlap with a cover factor,  $K_{cf}$ , of approximately 10 - 15 percent [3]. With few vanes, each vane has to be longer. A long vane guides the flow better than a short one, but it also accounts for larger friction losses. Thus the choice of number of guide vanes should be carefully considered.

$$L_{gv} = \frac{\pi D_0 K_{cf}}{Z_{gv}} \quad [m] \quad (4.43)$$

The guide vane axis should be located somewhere between the middle and three quarters of the vane length upstream from the trailing edge. It is important that both the overlap and axis location criteria are satisfied. The guide vane inlet diameter can now be found using the law of cosine.

To decrease the flow losses in the guide vane cascade, it is desirable to shape the vane as an airfoil. Smooth and symmetrical NACA profiles are often chosen.

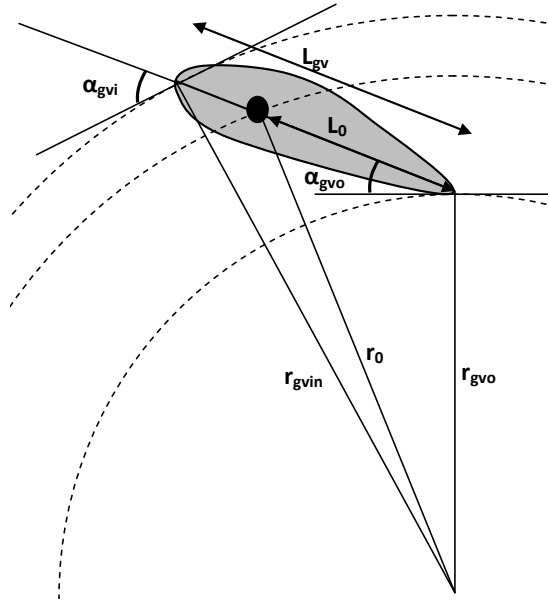


Figure 4.16: Geometry of guide vane

## 4.7 Stay vanes

The stay vanes are designed to have no hydraulic effect, and are present in the turbine cascade just to keep the spiral casing together. Thus the stay vanes have to withstand the maximum hydraulic force acting on the spiral casing.

The shape of the stay vanes follows a free vortex. The outlet diameter is usually chosen 2 percent larger than the guide vane inlet diameter [3]. The design process requires the designer to choose a stay vane inlet diameter. Then the length of the vane can be found, as the length of a streamline following the path of the free vortex from stay vane inlet to stay vane outlet.

The maximum force acting on the spiral casing is the maximum pressure times the area on which the pressure acts. The effective area of the spiral casing and the stay vanes is difficult to determine. As a simplification, the spiral casing and the stay vanes are modeled as an annulus with constant inner and outer diameter.

$$F_{max} = p_{max} \cdot A_{annulus} \quad [N] \quad (4.44)$$

$$A_{annulus} = \frac{1}{4}\pi(D_{outer}^2 - D_{inner}^2) \quad [m^2] \quad (4.45)$$

The maximum pressure acting on the area of the spiral casing occurs if the turbine running at full power is suddenly shut down. This will cause large pressure pulsations, known as the water hammer. The water hammer and the static pressure

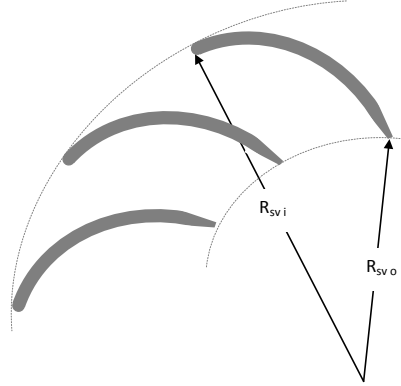


Figure 4.17: Stay vanes

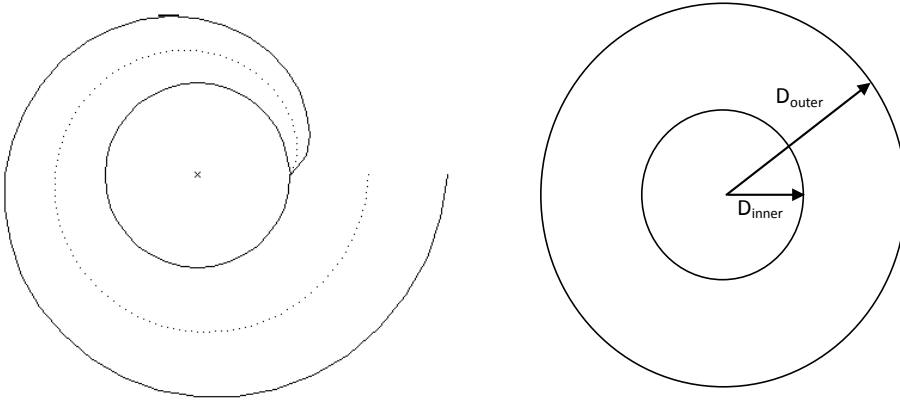


Figure 4.18: Traditional spiral casing and simplified annulus for calculating purposes

caused by the head difference give the dimensioning pressure.

$$p_{max} = p_{head} + p_{waterhammer} \quad [Pa] \quad (4.46)$$

Then the required cross sectional area of the stay vane can be found with maximum bending stress for steel,  $\sigma_{max}$ , equal to 100 MPa. Subsequently the required thickness is calculated.

$$A_{required} = \frac{F_{max}}{\sigma_{max} Z_{sv}} \quad [m^2] \quad (4.47)$$

$$t_{sv} = \frac{A_{required}}{L_{sv}} \quad [m] \quad (4.48)$$

## 4.8 Spiral casing

The purpose of the spiral casing is to distribute the flow evenly around the runner. Thus the cross section area of the spiral casing has to decrease downstream, as parts of the water flows through the stay vanes in each section.

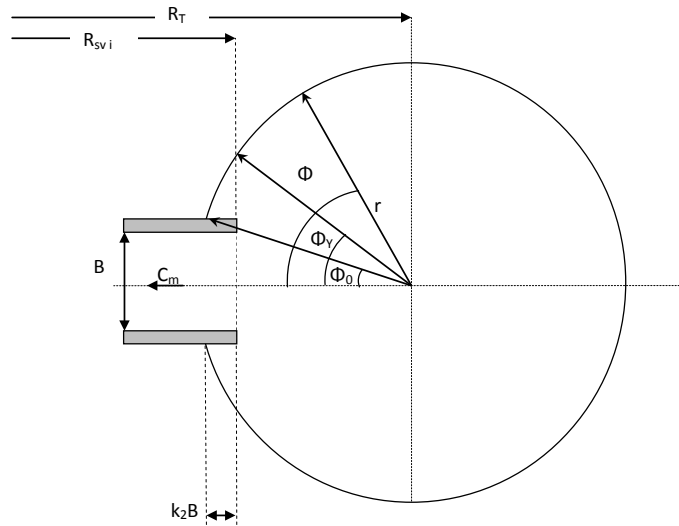


Figure 4.19: Cross section of spiral casing

The boundary layer in the spiral casing cause an energy loss, but it also induce a secondary flow. To prevent this secondary flow to propagate into the stay vanes and guide vanes, the spiral casing overlaps the stay vane inlet. The overlap factor

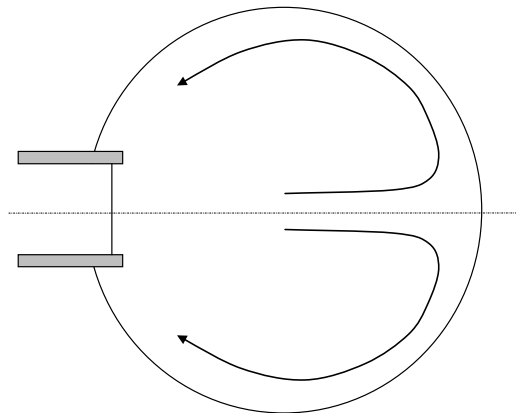


Figure 4.20: Secondary flow in the spiral casing

$K_2$  is traditionally set to 0.1 for high head Francis turbines [21]. For the design software however, this factor has been set to 0.05 based on discussions in the weekly design team meeting [28].

When designing the stay vanes, the designer has to choose a stay vane inlet radius,  $R_{svi}$ . As it is desirable to minimize the flow losses in the spiral casing, the casing is designed so that the flow follows a free vortex. The free vortex constant,  $K_{FV}$ , is found from the inlet dimensions of the stay vanes.

$$K_{FV} = C_{usvi} R_{svi} \quad [m^2/s] \quad (4.49)$$

The spiral casing is made of a number of sections chosen by the designer. Many sections cause a better and more correct reduction of the flow through the spiral casing, but it is also more expensive to manufacture due to the increased number of weld joints.

$R_T$  and  $r$  has to be calculated for each section in order to find the cross section area. This is obtained by at first choosing a starting value of  $r$ . Then  $\phi_0$  and  $\phi_y$  is calculated from geometrical relations according to figure 4.19. Next,  $R_T$  is calculated from equation 4.50, and then an new value of  $r$  is found by solving equation 4.51 with respect to  $r$ . This is an iterative process, which is repeated until the value of  $r$  has converged.

$$R_T(\theta) = R_{svi} + r(\theta) \cdot \cos(\phi_0) - K_2 B \quad [m] \quad (4.50)$$

$$Q(\theta) = 2r(\theta)^2 K_{FV} \int_{\phi_y}^{\pi} \frac{\sin^2(\phi)}{R_T(\theta) - r(\theta) \cdot \cos(\phi)} d\phi \quad [m^3/s] \quad (4.51)$$

When the dimensions of the spiral casing have been found, the thickness of the stay vanes should be calculated. If the required thickness is too small or too large, a new stay vane inlet diameter should be chosen. Subsequently the calculations of stay vane length, spiral casing dimensions and required stay vane thickness should be performed over again. This should be repeated until the required thickness of the stay vanes is acceptable.



## 5 Review of the Design Software

The design software is programmed in Matlab. It has a graphical user interface (GUI) consisting of a window with nine tabs. The tabs allow the designer to easily move between the different Francis turbine design steps. Tab two to four have an *Update Design* button. This has to be executed if the designer wants to check how the change made alters the following design steps. It is also necessary to execute the update button in the following tabs after a change is made in one of the earlier tabs.

The program is fitted for a screen resolution of 1680 x 1050. Hence might the tabs look somewhat untidy if running on a different screen resolution.

The program has been tested and used by the members of the Francis turbine design team during spring 2011. The program has been improved and expanded based on the team's findings and needs. It can however not be guaranteed that all bugs have been discovered. Further improvements and expansions might be added in the future.

### 5.1 Tab 1 - Intro

In the first tab, the designer is given three choices: Start a new design, load an old design, or compare a design with CFX results.

Starting a new project, the turbine is designed from scratch. Loading a project

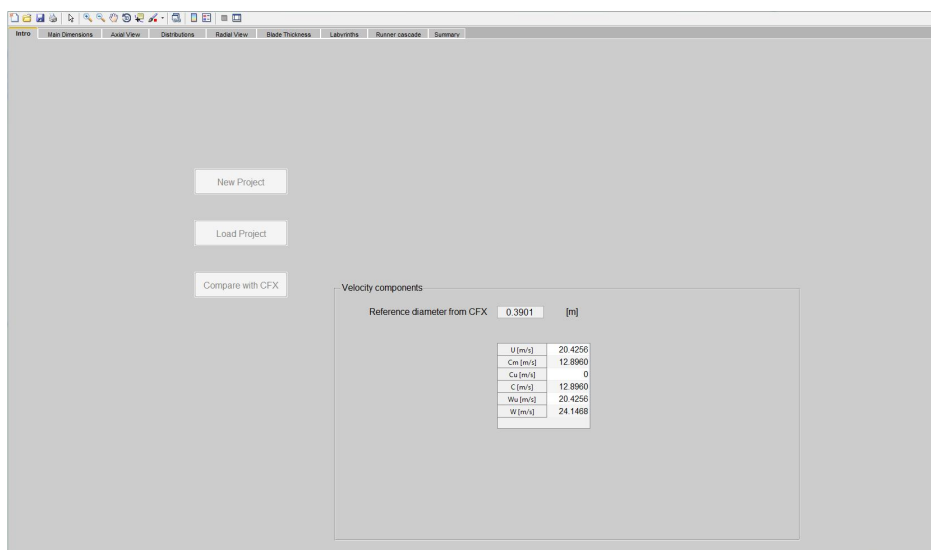


Figure 5.1: Tab 1 - Intro tab

allows the designer to load an old design for viewing it or for modifications. The *Compare with CFX* function was necessary because the velocity components provided in the hydraulic turbine report in CFX Post is given at a reference diameter which is not at the shroud. When executing this button, the designer is asked to load the design which has been analysed with CFX. Then the reference diameter which is listed in the hydraulic turbine report has to be submitted. The design software then calculates the velocity components at the trailing edge for this diameter and lists these in a table as shown in figure 5.1. With these values, it is possible to compare the velocities from the CFD results with the design software results.

## 5.2 Tab 2 - Main Dimensions

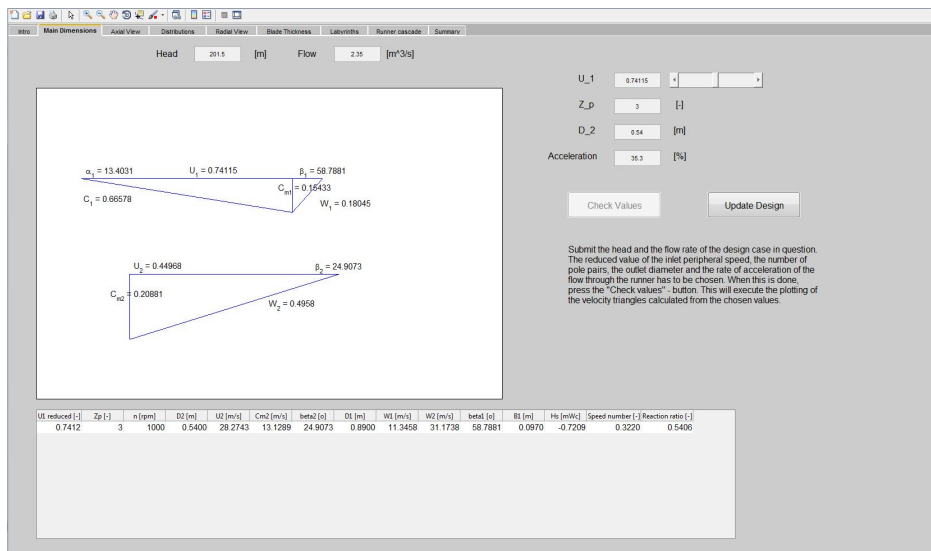


Figure 5.2: Tab 2 - Main dimensions

In the second tab the main dimensions have to be decided. The designer has to input the nominal head and the flow rate of the site. In addition, the reduced value of the inlet peripheral speed  $U_1$ , the number of pole pairs in the generator  $Z_p$ , the outlet diameter  $D_2$  and the acceleration of the flow through the runner, denoted  $Acc$ , has to be chosen. When this is done, the designer can press the *Check values* button. This will execute the plotting of the velocity triangles calculated for the chosen values.

Data for the turbine will be added in the table below the velocity triangles. Each time the *Check values* button is executed, a new line is added in the table, allowing the designer to compare the values of the different tested main dimension combinations.

### 5.3 Tab 3 - The Axial View

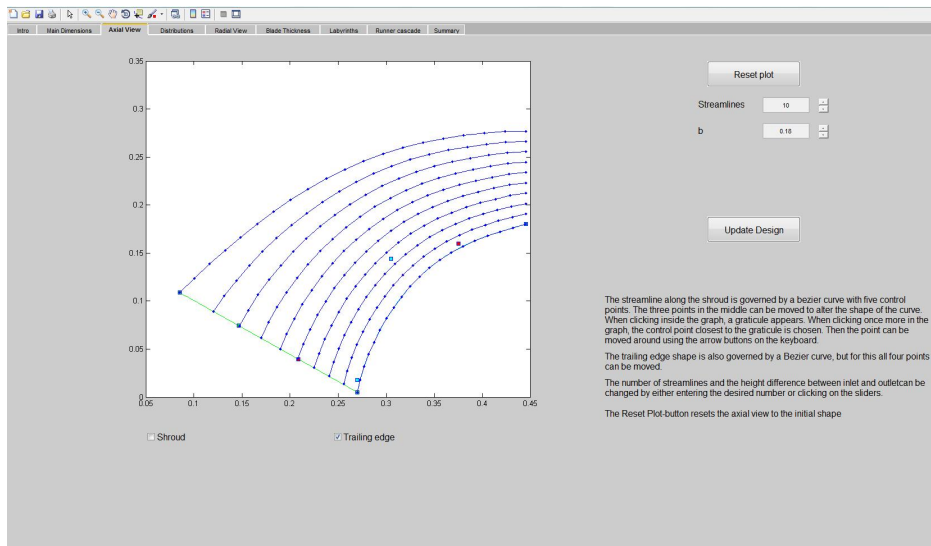


Figure 5.3: Tab 3 - Axial view

In the third tab the designer has to decide the axial view of the runner. Traditionally the first streamline is decided to have a circular or elliptical shape. With the design software it is possible for the designer to choose the shape of the first streamline to have a more general shape. This is implemented using a Bezier curve with five control points. The three points in the middle can be moved by the designer. When clicking inside the graph, a pair of cross hairs appears. When clicking once more in the graph, the closest control point is chosen. Then the point can be moved around using the arrow keys on the keyboard.

The designer also has the possibility to decide the outline of the trailing edge in the same way as for the shape of the shroud. The check boxes below the graph tell which line that can be changed.

A Bezier curve (as illustrated in figure 5.4) is specified by its two end points and a number of control points in between. This gives a great flexibility of the design. In the design program a fourth power Bezier curve is used for the shroud contour, which means that it has three control points between the end points. For the trailing edge shape, a cubic Bezier curve is implemented. A cubic Bezier curve has two control points in between the end points. The Bezier curve is suitable for these applications because the curve is both a smooth line between the endpoints, and tangent to the line between the endpoints and the closest control point at the end point.

To the left in the tab, the designer is allowed to choose the number of streamlines. It is also possible to alter the height difference between the first and the last control

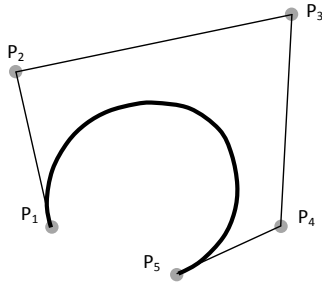


Figure 5.4: Fourth power Bezier curve

point, which comes out as the height difference between the inlet close to the shroud and the outlet close to the shroud. This height difference is denoted  $b$ .

## 5.4 Tab 4 - The Blade Angle Distribution and the $GH$ -plane

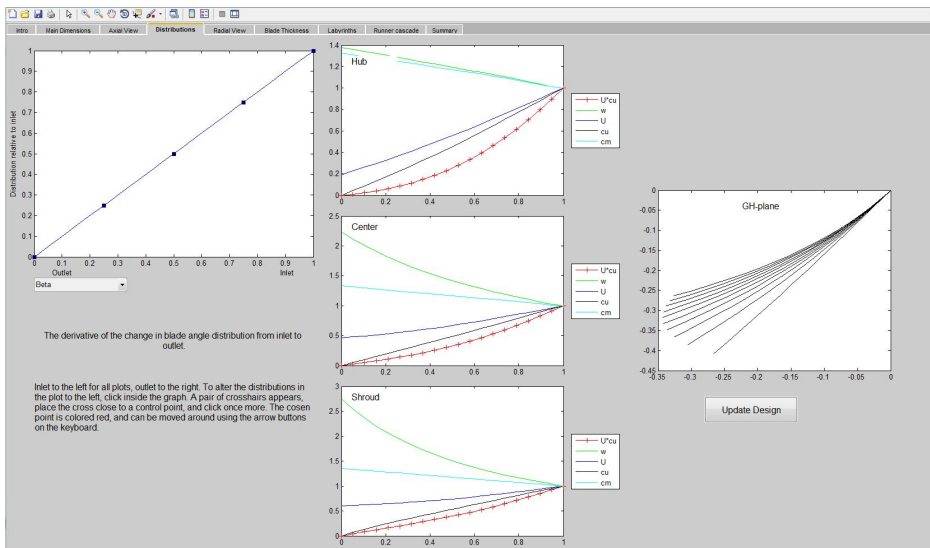


Figure 5.5: Tab 4 - The blade angle distribution and the  $GH$ -plane

In the fourth tab the designer determines the  $GH$ -plane by deciding either the distribution of the blade angle or the energy distribution. The shape of these distributions is also governed by a Bezier curve with five control points. As for the axial view shroud contour, the three points in the middle can be selected by clicking in the graph and moved around using the arrow keys. The same distribution is used for all streamlines.

In the centre of the window, the distributions of the different velocity components from inlet to outlet are plotted at the hub, in the middle of the channel and at the shroud. The energy distribution is also plotted in these plots. The inlet is to the right and the outlet is to the left in all plots.

## 5.5 Tab 5 - The Radial View and Runner Blade

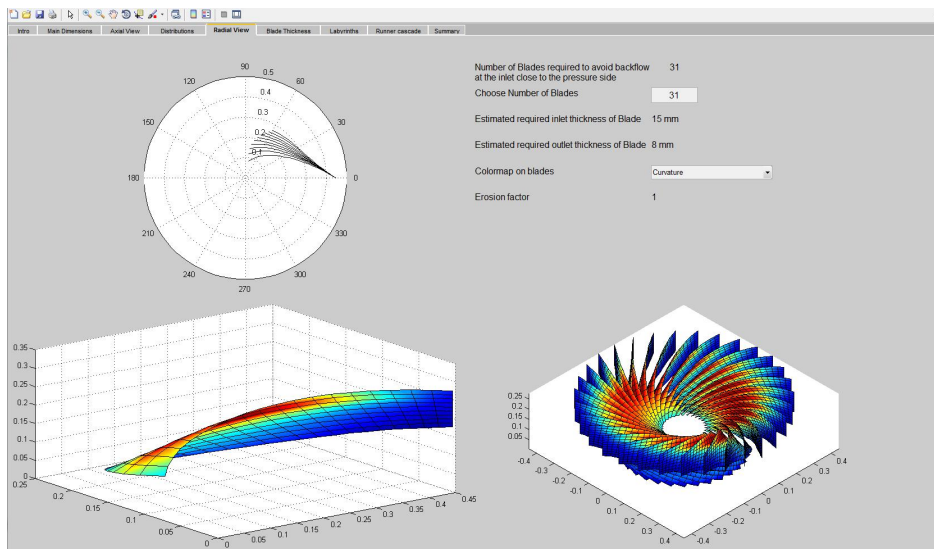


Figure 5.6: Tab 5 - Radial view and runner blade

The first two plots in the fifth tab show the output of the previous design choices. The upper left one is the radial view of the blade, the lower left one is the 3D view of the blade. The colour map on the blade is determined by the designer. This can be used to see where the relative velocity is at its highest, where on the blade the dimensioning case for number of blades appears or where the curvature of the blade surface is biggest.

The designer has to choose the number of blades in the runner. A calculation according to the one described in chapter 4.4 is performed and the result is listed as a suggestion of the number of blades required to avoid backflow, but it is not an absolute limit. It is possible to choose fewer blades than suggested, as it seems as if the method used to calculate the required number of blades might be somewhat too conservative. The blade thickness at the inlet and at the trailing edge is also listed. The last parameter listed is the erosion factor, which is calculated as described in chapter 10.1. The third plot in this tab is the runner plotted with the number of blades chosen by the designer.

## 5.6 Tab 6 - Blade with Thickness

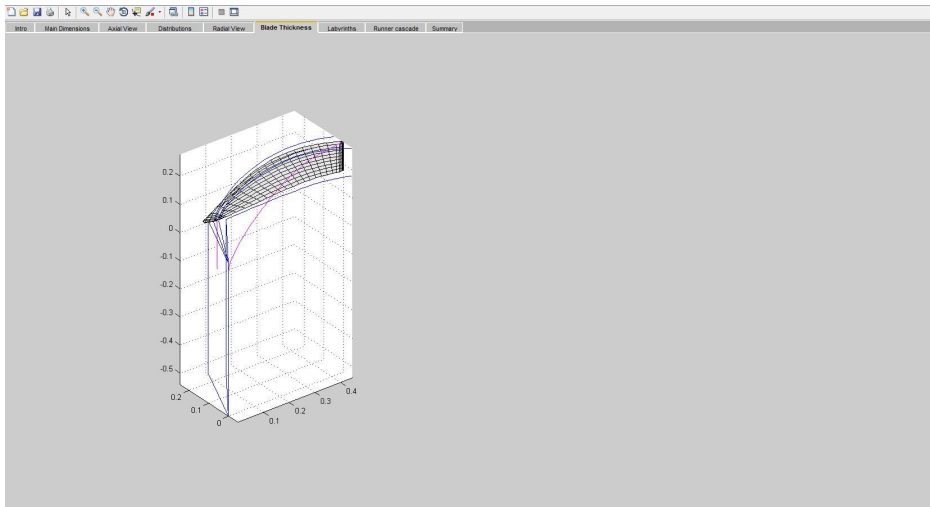


Figure 5.7: Tab 6 - Blade thickness

In this tab, the blade is plotted with thickness. A screen shot of the tab is shown in figure 5.7. The blue lines surrounding the blade is showing the domain used for CFD simulations. TurboGrid does however divide the calculation domain itself, based on the number of blades. Intentions are to implement new functions in this tab, like for instance leaning of the blade for better control of the pressure distribution.

## 5.7 Tab 7 - Labyrinths

In the seventh tab, the location of the labyrinth seals are calculated, such that axial forces acting on the runner is balanced to have a resultant force acting down towards the draft tube. For the time being, the weight of the runner is assumed to be 1 000 kg, independent of the unit size. The unit is also assumed to have a vertical shaft, so that the weight is causing a stabilizing axial force. The designer has to decide the thickness of the shroud at the outlet of the runner, in order to calculate at what diameter the upper labyrinth seal has to be placed to fulfil the requirement of the resultant force. For now, the resultant force has to be at least 1 000N. The calculation of the hydraulic axial forces are performed in accordance with Brekke [21, Chapter 4].

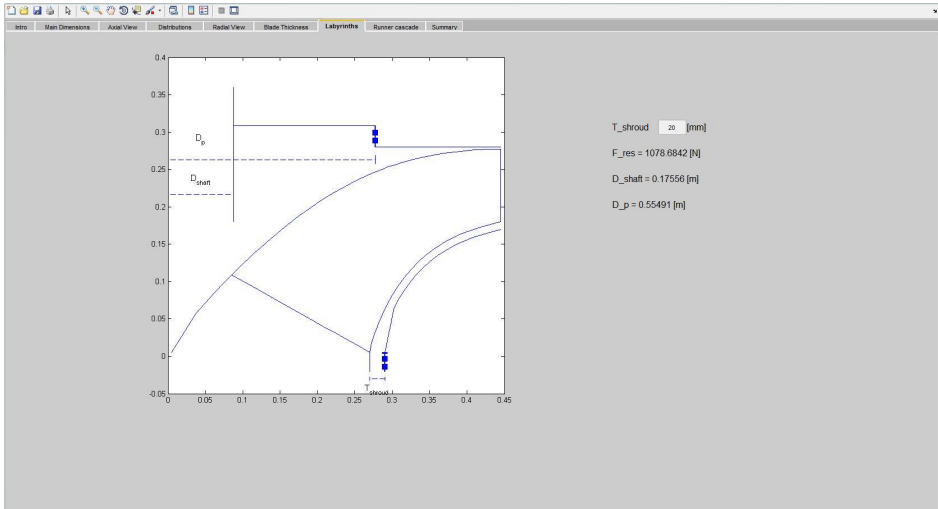


Figure 5.8: Tab 7 - Labyrinths

## 5.8 Tab 8 - Guide Vanes, Stay Vanes and Spiral Casing

This tab is for designing the guide vanes, stay vanes and spiral casing. The designer has to choose the number of guide vanes,  $Z_{gv}$ , and the diameter for where the guide vanes are fixed, denoted as  $D_0$ . It is important to make sure that the number of

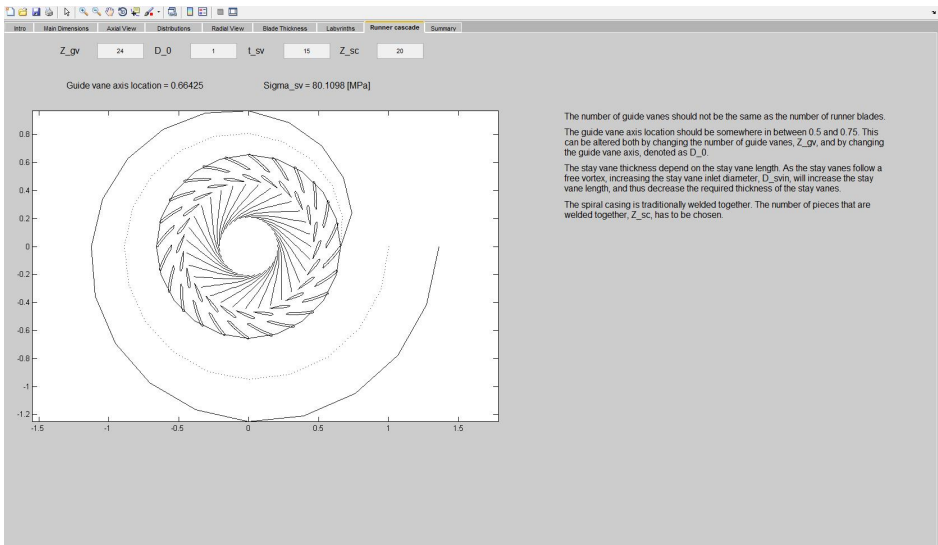


Figure 5.9: Tab 8 - Guide vanes, stay vanes and spiral casing design

guide vanes chosen does not cause any problems in terms of pressure pulsations, as discussed in chapter 4.6.

Next, the thickness of the stay vanes has to be chosen. The maximum stresses in the stay vanes  $\sigma_{sv}$  is not allowed to exceed 100 MPa. The designer might need to try different stay vane thicknesses before obtaining a reasonable stay vane length.

## 5.9 Tab 9 - Summary

In the last tab, a summary of the turbine data is given. In addition, the designer has the possibility of saving the design. When the *Save Design* button is executed, a text box appears below the button. A folder named with the text entered in the text box is created inside the *Design* folder in the current directory and a *.mat*-file containing all the design parameters is saved.

The designer also has the possibility to export the design as *.curve*-files for Turbo-Grid import and as *.txt*-files for import in Pro/E by executing the *Export Design* button. These files are saved in a folder with the same name as the design were saved as in the folder *Exported designs* in the current directory.

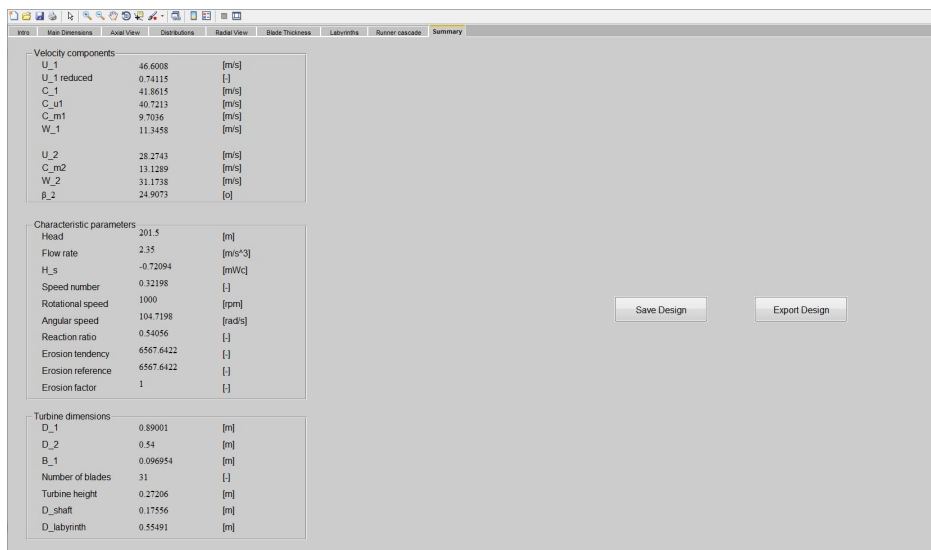


Figure 5.10: Tab 9 - Summary



## 6 CFD Theory

CFD is a recognized tool for analysis of hydraulic machinery like Francis turbines. In this thesis, CFD is used to verify the results from the design software. A wide variety of CFD tools are available, both commercial and open source software. Ansys CFX was chosen because of in-house experience and previous work of similar problems with promising results. CFX also provides the opportunity to run simulations with sediment particles in the flow to predict erosion. All simulations are performed in Ansys 13.0.

### 6.1 Mesh Generation: ATM Optimized Mesh

The Automatic Topology and Meshing (ATM optimized) mesh feature was new in the Ansys TurboGrid Release 13.0. It is said to generate "high-quality meshes with minimal effort" [29]. This agrees with experience gained when using this meshing feature. Mesh generation is fast, and we have scarcely experienced issues with negative volumes in the meshes, which were the biggest problem when generating meshes the traditional way.

To get the trailing edge shaped correct in TurboGrid, we should use the 'cut-off and squared' option available when loading the geometry. Release notes state that it should be possible to use this option together with the ATM optimized feature. We have however experienced trouble with this combination, and thus we have chosen not to use it. To improve the shape of the leading and trailing edge, we have chosen the surface type to be ruled. This gives no problems with negative volume and a more correct shape of the trailing edge than the default option.

### 6.2 Turbulence Modelling

A vast variety of turbulence models are available in Ansys CFX but not all of them are suitable for flows dominated by boundary layer behaviour or for fluids in rotating systems.

The  $k-\epsilon$  model is the most commonly used turbulence model in the industry due to its stability and numerical robustness. This model is valid for the free stream region, but tends to fail in the viscous sublayer. The  $k-\omega$  model used to be the most common alternative to the  $k-\epsilon$  model, providing robust and accurate results for the viscous sublayer. This model is however very sensitive in free stream region calculations.

In lack of a turbulence model which could handle both the viscous sublayer and the free stream region, Menter [30] proposed a new model called the shear stress transport model (SST model). This model retains the properties of the  $k-\omega$  model close to the wall, but gradually blends into the  $k-\epsilon$  model away from the wall as illustrated in figure 6.1.

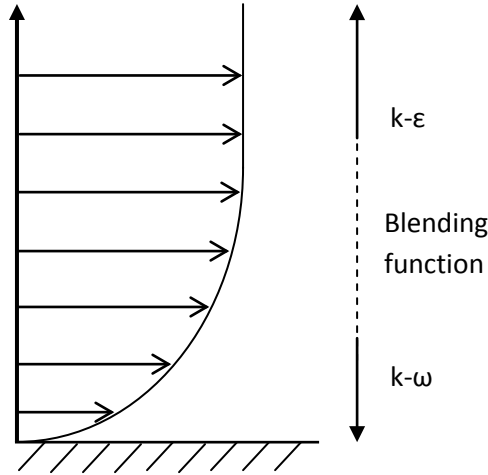


Figure 6.1: SST model

The mesh resolution is defined by  $y^+$  values. The  $y^+$  parameter is a non-dimensional distance from the wall to the nearest mesh node, defined as

$$y^+ = \frac{\rho \cdot \Delta y \cdot u_\tau}{\mu} \quad [-] \quad (6.1)$$

where  $u_\tau = (\frac{\tau_w}{\rho})^{(1/2)}$  is the friction velocity and  $\Delta y$  is the distance from the wall to the first mesh node.  $\tau_w$  is the wall shear stress.

Theoretically, a mesh resolution of  $y^+ \sim 1$  is required for the SST model to account for the physics of the flow all the way throughout the viscous sublayer. Such low  $y^+$  value is however hard to obtain for a Francis turbine runner blade. An alternative is to not resolve the near-wall flow completely, but use a wall function approach on the flow close to the no-slip wall instead. The wall function method assumes a velocity profile for the near-wall region, as shown in figure 6.2. This implies that the CFX solver does not have to resolve the boundary layer, allowing a much coarser mesh, which is computationally cheaper yielding lower runtime and computer-memory requirements.

Several sources state that using wall functions instead of resolving the flow all the way down to the wall gives sufficiently accurate results. Menter [31] found that for a Couette flow, the computed shear stress varies by less than five percent when changing the mesh resolution from  $y^+ \sim 0.2$  to  $y^+ \sim 100$ . Apsley [32] states that to obtain good results when using wall functions, meshes cannot be made arbitrarily fine. He suggests an  $y^+$  value in the interval between 30 and 150. This is confirmed by Skaare [33, personal conversations], who recommends a mesh resolution in an approximate range from  $y^+ \sim 20$  to  $y^+ \sim 200$  for a Francis turbine runner blade. He also states that it is impossible to have a constant value of  $y^+$  over the entire

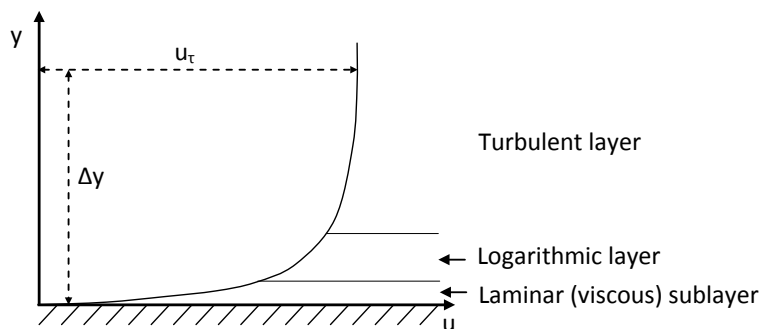


Figure 6.2: Wall function. Adapted from [5]

blade, and that it is the  $y^+$  value on the main part of the blade that has to be found within the recommended range. The low  $y^+$  values at the leading and trailing edge can be disregarded.

For  $k-\omega$  based turbulence models, including the SST model, CFX applies an automatic near-wall treatment method[17]. This implies that CFX decides whether to resolve the flow right up to the wall or to use a wall function based on the resolution of the mesh, and it automatically switches between the two as the mesh is refined. This is only possible because an analytic expression for  $\omega$  in the viscous sublayer is known for the  $k-\omega$  model.

### 6.3 Sediment Erosion Prediction using CFD

Commercial CFD software has been available for quite some time, but few have used it to predict erosion in Francis turbines. By implementing particles in a CFD simulation of a Francis turbine, theoretical estimates of erosion areas and erosion intensity can be predicted. These theoretical estimates do however depend on several variables. Due to complex relations between the different variables, an accurate mathematical model is yet to be established. This implies that research work in this field is necessary to develop good and sufficiently exact empirical and statistical relations.

Frawley et al. [34] simulated erosion in an elbow using the commercial software *FLUENT 6.1*. Their simulated erosion results are coincident with measured data. The simulations are performed on meshes with  $y^+$  values in the range 1-5 in the area where they expect erosion to occur. In the areas less prone to erosion and where the flow field was of secondary interest, a coarser mesh with  $y^+$  values in the range 30-210 was applied in the near wall region.

Ansys CFX has two different pre-implemented erosion models; *Finnie's erosion model* and *Tabakoff and Grant erosion model*. Neither of them is perfectly suited for erosion prediction in Francis turbines [12]. Eltvik tested both and found *Tabakoff*

and *Grant erosion model* to give the most realistic values [35]. Eltvik performed the simulations on meshes with approximately 130 000 nodes. This is a relatively coarse mesh for a Francis turbine runner with an inlet diameter of approximately 1.5m, yielding  $y^+$  values far above the recommended range. The results did however give similar erosion trends as observed on turbines exposed to sediment erosion.

## 7 Computational Model for Francis Turbines

The computational model for the Francis turbines analysed in this thesis consists of only one runner blade. The geometry is generated using the design software. This chapter describes the mesh generation and the definition of the boundary conditions.

### 7.1 Mesh Generation

All meshes are generated using the ATM optimized feature in Ansys TurboGrid (see section 6.1). A smooth transition between the small and the larger control volumes is ensured by specifying the boundary layer refinement control parameters as shown in table 7.1. The methods and values are chosen based on recommendations from Eltvik [12, 36, Personal conversations].

<b>Proportional refinement:</b>	
Factor ratio	1.25
<b>Near wall element size specification:</b>	
Method	$y^+$
Reynolds number	500 000

Table 7.1: Boundary layer refinement control data

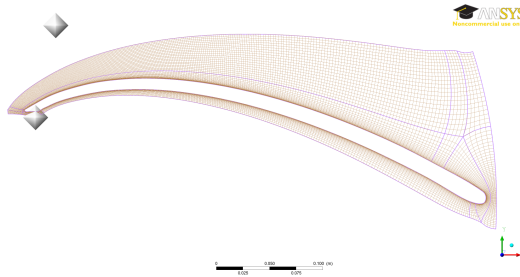


Figure 7.1: TurboGrid ATM mesh

It has however been impossible to make a mesh with these values that is fine enough to meet the  $y^+$  value recommendations and still not require more computer memory than available. Changing the *Factor ratio* to 2.0 allows a finer mesh in the near-wall region, yielding  $y^+$  values in the recommended area for a mesh with approximately one million nodes. Increasing the factor ratio implies increasing the expansion ratio of the mesh cells size. If increasing the factor ratio too much, the solver will have problems to converge smoothly. A factor ratio of 2.0 does however not imply convergence problems, and simulation results are showing the same trends as the simulations with a ratio of 1.25.

## 7.2 Boundary Conditions

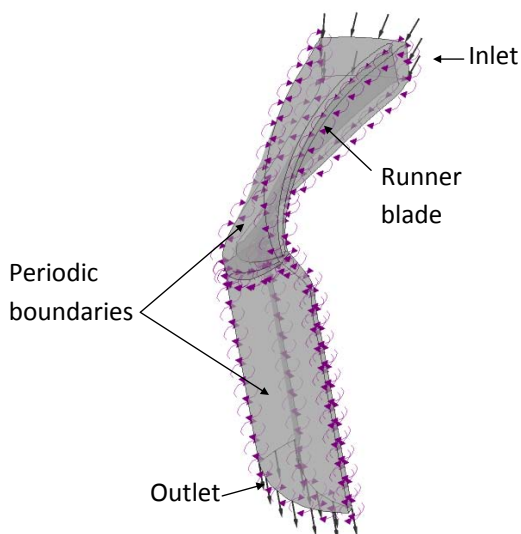


Figure 7.2: Computational domain

Simulations are performed for one runner blade. The calculation domain with periodic boundary conditions are shown in figure 7.2. The blade, hub and shroud are modelled as walls. The flow can be solved either viscous or inviscid. This is determined by the boundary condition on the walls of the hub, shroud and blade. For viscous simulations, a no-slip condition has to be chosen, implying zero velocity at the wall and a boundary layer between the wall and the free stream region. An inviscid simulation is a simplification of the viscous case. Then a free slip condition at the walls implies that the boundary layer is disregarded, and the velocity of the flow at the walls is equal to the velocity in the free stream region. This implies that the friction loss caused by the no-slip condition is not taken into account, yielding a slightly higher efficiency.

For simulations of Francis turbines, it is recommended to specify the mass flow at the inlet and the static pressure at the outlet [12]. For all simulations in this thesis, the mass flow rate is set to  $2.35 \text{ m}^3/\text{s}$  and the static pressure at the outlet is equal to one atmosphere. The direction of the flow at the inlet is specified using cylindrical coordinates. The design software calculates these coordinates, but without taking the blade thickness into account. Disregarding the blade thickness causes that the head calculated based on the CFD simulation results is inconsistent with the design head. To obtain a correct head, it is necessary to iterate on the velocity components as shown in figure 7.3. For this process, a small MATLAB program running CFX in batch mode has been developed. If the program is run with a fairly coarse grid, the simulation time is sufficiently fast and accurate (see

section 9). Velocity components that give a head within 0.25% of the design head are deemed acceptable, and are found to give sufficiently accurate results when applied for simulations on fine grids too. Further, the mesh has to be saved as *Combined in one domain, one file*, as this is what the *.pre*-file is set up for. If another way of saving the mesh is desirable, a new *.pre*-file is necessary.

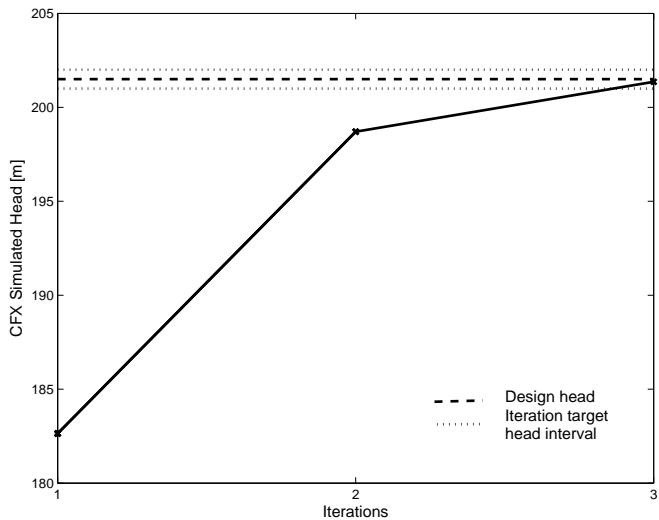


Figure 7.3: Iterating for velocity components to give the design head for CFX simulations





## 8 Reference Design

Jhimruk HEC is chosen as a reference case for this project. The objective is to design a new turbine for the power plant. Thus, based on the head, flow rate, rotational speed, outlet and inlet dimensions of the existing turbines, a reference design was established using the design software.

The existing turbines at Jhimruk have splitter blades, consisting of 15 ordinary blades and 15 half-length blades. Splitter blades have not been implemented in the design software, instead 17 ordinary blades are chosen for the design. In order to account for the thickness of the blades when designing the turbine, we had to choose the thickness when deciding the main dimensions. The blade thickness of the existing turbines is not known. A thickness of 15 mm at the leading edge and 8 mm at the trailing edge were chosen. The reference turbine data are listed in table 8.1.

Head	$H$	201.5	m
Flow rate	$Q$	2.35	m <sup>3</sup> /s
Outlet diameter	$D_2$	540	mm
Rotational speed	$n$	1000	rpm
Inlet diameter	$D_1$	890	mm
Inlet height	$B_1$	97	mm
Number of blades	$Z_{blades}$	17	-
Thickness at leading edge	$t_{LE}$	15	mm
Thickness at trailing edge	$t_{TE}$	8	mm
Speed number	$\Omega$	0.3220	-
Submergence requirement	$H_s$	-0.7209	mWc
Reaction ratio	$R$	0.5406	-

Table 8.1: Reference turbine data

### 8.1 CFD Analysis

To verify the reference design, a CFD simulation is carried out. Mesh data can be found in table 8.2. Concerning the values of  $y^+$ , the lower values appear on the leading and trailing edge, and can be disregarded, according to Skaare [33, Personal conversations]. To obtain the  $y^+$  values on the main part of the blade within the recommended range, the *Factor ratio* had to be set to 2.0, despite the recommendations of a lower value.  $y^+$  values on the blade are shown in figure 8.1.

All velocities and angles at the inlet calculated in the design software are more or less coincident with the CFX simulation results, as shown in table 8.3. The velocities from CFX does not assembly exact to a correct velocity triangle. In the hydraulic report provided in CFX-Post, a distortion parameter is listed. This parameter gives the ratio between the length of the absolute velocity  $C$  found by

Elements	1055705
Nodes	1113650
$y_{max}^+$	99.55
$y_{min}^+$	1.281
$y_{avg}^+$	42.98

Table 8.2: Reference turbine mesh data

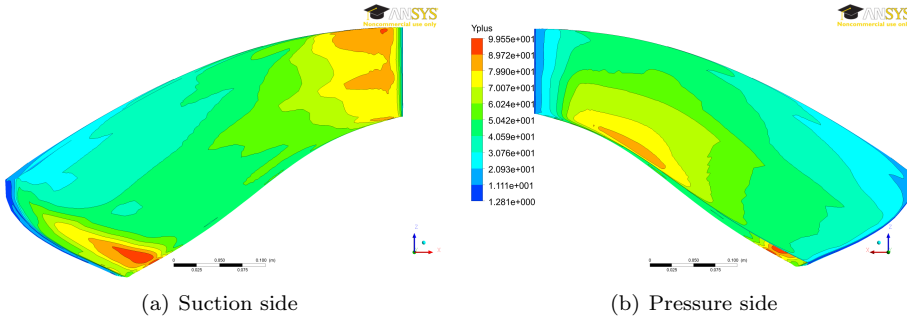


Figure 8.1:  $y^+$  values on runner blade for mesh with *Factor ratio*=2.0

Variable	Design software		CFX		Difference [%]
Head $H$	201.5	m	200.05	m	0.71
Flow rate $Q$	2.35	m <sup>3</sup> /s	2.3571	m <sup>3</sup> /s	0.30
Efficiency $\eta$	96	%	97.8424	%	1.92
Inlet velocities:					
$U_1$	46.6008	m/s	46.6565	m/s	0.12
$C_{m1}$	9.7036	m/s	9.0115	m/s	7.68
$C_{u1}$	-40.7214	m/s	-41.0482	m/s	0.80
$C_1$	41.8615	m/s	42.0463	m/s	0.44
$W_1$	11.3458	m/s	11.1203	m/s	2.03
$W_{u1}$	5.8794	m/s	5.6084	m/s	4.83
Outlet velocities at diameter $D_{ref}$					
$U_2$	390.1	mm	390.1	mm	
$U_2$	20.4265	m/s	20.4233	m/s	0.02
$C_{m2}$	12.8960	m/s	12.3053	m/s	4.80
$C_{u2}$	0	m/s	-0.9208	m/s	-
$C_2$	12.8960	m/s	13.9976	m/s	7.87
$W_2$	24.1468	m/s	23.2430	m/s	3.89
$W_{u2}$	20.4256	m/s	19.5026	m/s	4.73

Table 8.3: Comparison of reference turbine data from design software and CFX

CFX and the vector sum of the  $C_u$  and  $C_m$  components. A low value of the distortion parameter is desirable. For the reference runner, the distortion parameter is only 1.0235 at the leading edge, whereas it is 1.1296 at the trailing edge. The relatively large distortion parameter at the outlet (12.96 %) causes the difference in the velocity components from the design software and CFX. The largest difference is the  $C_u$  component, which ideally should be equal to zero. CFX calculates this to be -0.9208 m/s, implying operation slightly at part load. Studying figure 8.2, we see from the streamlines that there is almost no swirl in the flow close to the wall in the draft tube. The swirl that can be seen in the centre of the draft tube is generally considered to be harmless for the turbine, and is thus of no concern. A  $C_u$  component of 0.9208 m/s does not represent a large energy loss, as can be calculated according to equation 8.1.

$$\text{Energy loss} = \frac{C_2^2 - C_{m2}}{2 \cdot g} \quad [mWc] \quad (8.1)$$

This should ideally equal  $\frac{C_{u2}^2}{2 \cdot g}$ , but due to the distortion parameter in CFX, the loss is slightly larger. For the reference design is the energy loss equal to 2.27 mWc if using the value of  $C$  from CFX. Calculating the energy loss based on the value of  $C_{u2}$ , it is only 0.04 mWc.

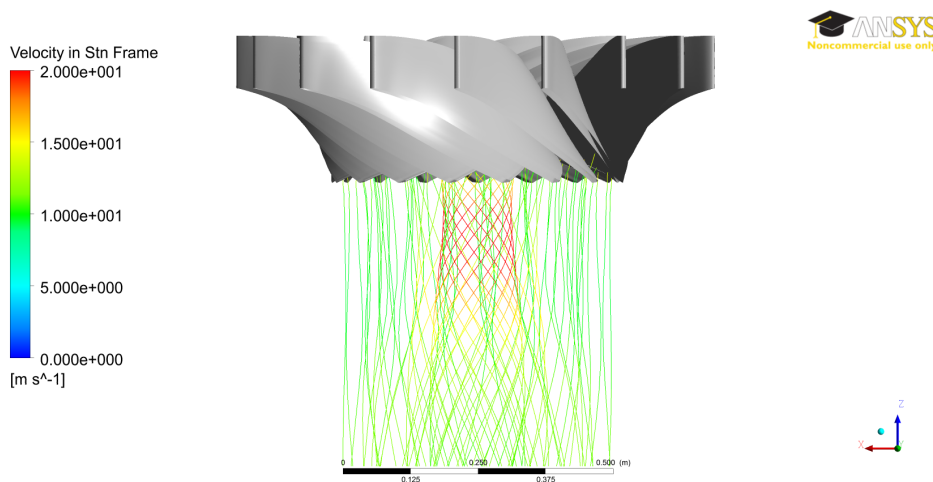


Figure 8.2: Streamlines in draft tube at BEP

Figure 8.3 shows the transition of the relative velocity from inlet to outlet. There are no swirls in the blade channels, and the acceleration of the flow is smooth. In figure 8.3(a), we see that the magnitude of the relative velocity is quite uniform when the flow enters the draft tube. The velocity differences close to the draft tube wall is due to the end of the blade causing flow from the pressure side and suction side of the blade to meet, and is levelled shortly after entering the draft tube.

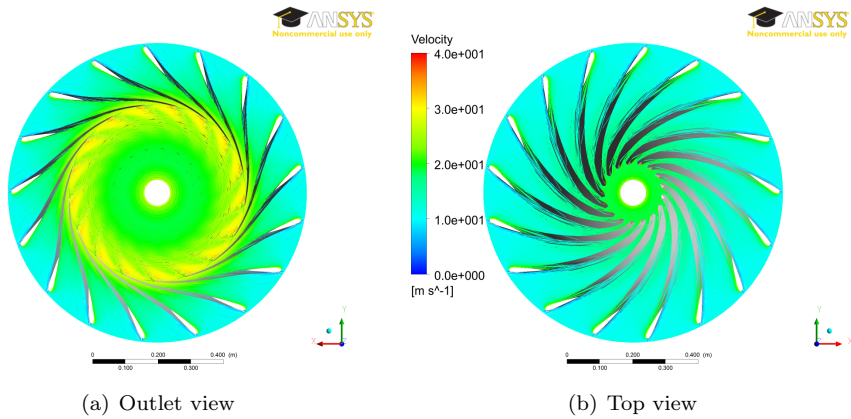


Figure 8.3: Relative velocity in runner seen from outlet and from top

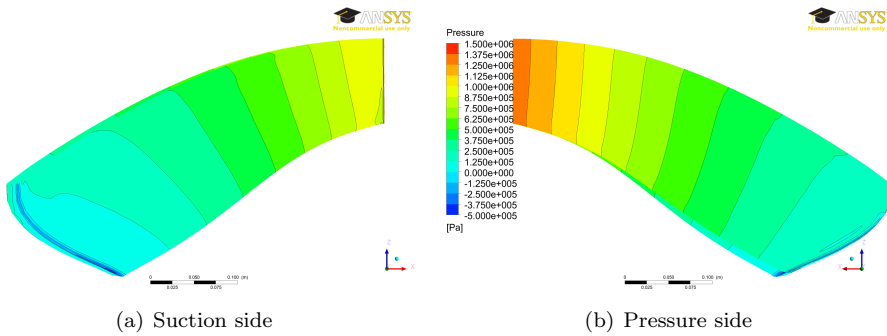


Figure 8.4: Relative velocity in runner seen from hub and from shroud

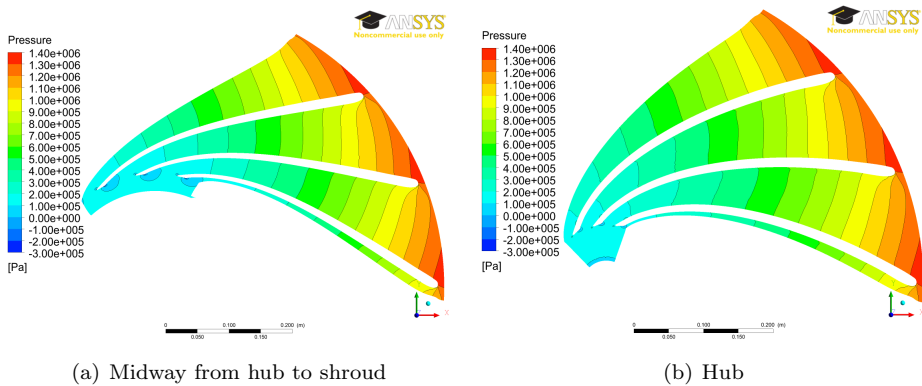


Figure 8.5: Blade to blade pressure distribution

Figure 8.4 shows the pressure distribution on the blade surface. A smooth transition from the leading to the trailing edge, with straight contour lines is desirable. The distribution on the pressure side is very good, showing a smooth transition. On the suction side, the inlet region is good. Towards the trailing edge the distribution is not as straight as desirable, but still acceptable. Fine tuning of the blade trailing edge is needed to improve the distribution. Figure 8.5 show the pressure distribution between the blades from inlet to outlet. A pressure distribution with slanting or wavy contour lines will experience problems due to cross flows from high to low pressure regions. This design does not have that problem, except for a small high pressure region on the suction side, close to the hub at the trailing edge. This is not considered as a big problem, and is accepted for the reference design. Small modifications to the design will be necessary to avoid this high pressure region.

The negative pressure region at the trailing edge is an undesirable effect, prone to cause cavitation. We have experienced trouble modelling the trailing edge. Importing points to define each streamline into TurboGrid, for TurboGrid to generate the blade surface, implies using splines along the curves. This implies that the sharp edges at the trailing edge are rounded off, unfortunately not as we desire it, but as shown in figure 8.6. The low pressure region might be a result of that.

The initial design is generated using the design software. This geometry is exported both to Pro/ENGINEER (Pro/E.) for the mechanical design of the turbine, and to TurboGrid for CFD analysis of the hydraulic design. This is inefficient because both softwares have to generate the blade and might also cause small numerical differences between the two models. Hopefully, drawing the leading and trailing edges in Pro/E. and subsequently exporting the geometry to TurboGrid, the shape of the edges will be more equal to what we desire, and possibly avoiding the negative pressure region to occur. However, obtaining the exact shape of the trailing edge might not be crucial in the early optimization phase, where design flaws like swirls and low efficiency are more critical.

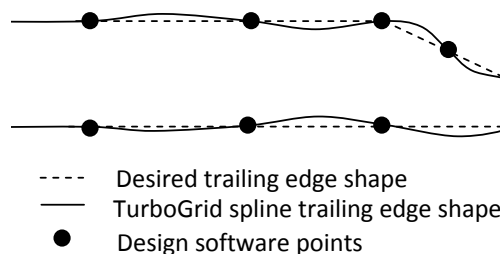


Figure 8.6: Trailing edge shape in TurboGrid, somewhat exaggerated

## 8.2 Erosion Prediction in CFX

Erosion predicting simulations have been performed for the reference design, on different meshes, as shown in figure 8.7. The  $y^+$  value decreases for increasing mesh sizes. For the lowest  $y^+$  value plotted, the mesh is very fine, consisting of approximately 10 million elements. The memory and run time requirements are consequently very high.

Literature correlating mesh size and erosion prediction using CFD codes has been hard to obtain, and so has best practice recommendations as well. Thus was Frawley et al. [34] taken as the best reference available. For the reference case, an extremely fine mesh is necessary if the  $y^+$  values should be kept below five. This requires a lot of computer memory and the run time for each simulation is high. Testing the mesh size shows that the erosion prediction does not seem to converge even for the lowest  $y^+$  values tested, as shown in figure 8.7. Due to this, further study on mesh size for erosion prediction with CFD analysis should be carried out. Due to time limitations and lack of permanent access to a computer with enough memory, it will not be done as a part of this thesis.

It has been questioned whether the poor results are due to the ATM optimized mesh or the mesh size. Eltvik claims to have obtained better results with traditionally generated meshes than for the ATM meshes. It is however likely that mesh size plays an important role too. Results for a fine, traditionally generated mesh would be interesting to investigate, but this will not be performed, due to computer memory and time limitations.

The quality of the erosion model used is also questionable, as it is not developed for the operational conditions and materials of a Francis runner. As a result of this, a simple erosion model has been implemented in the design software, estimating the erosion based on the velocity cubed. The idea is to give a relative measure of the erosion that can be compared with the reference design without relying on CFD. This factor is defined in section 10.2.

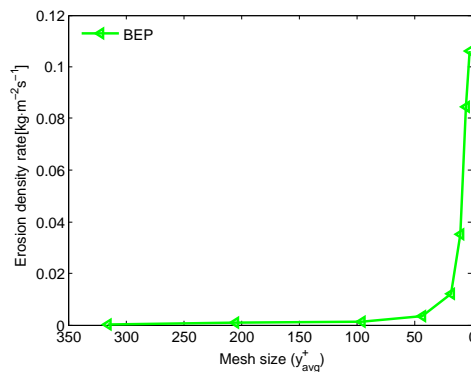


Figure 8.7: Erosion rate density for different mesh qualities

## 9 Verification

All CFD simulations should be verified to give realistic and mesh independent results. To ensure mesh independency, the mesh should be refined until simulations give the same results for different resolution meshes. In terms of computer memory and run time requirements, it is desirable with as coarse meshes as possible. In order to ensure that the results are realistic, results should ideally be compared with experimental results.

### 9.1 Multilevel CFD

Full Navier-Stokes CFD simulations are computationally expensive, and conducting an optimization study using this method directly would be very time demanding. The effort can be reduced by using multilevel CFD, which implies that the initial simulations are carried out on a lower accuracy level, capturing the trends but not every detail. However, to be able to use multilevel CFD, we need to know that the low-level methods are sufficiently accurate and capture the physics correctly.

The simulation time is decided by the number of calculation domains, defined by the mesh size, and the number of equations to solve for each domain. Using a coarser mesh will reduce the number of mesh points and consequently also the simulation time. Another approach to reduce the simulations is to use inviscid calculations; the viscous boundary layer both requires finer mesh to capture the physics and increases the number of equations to be solved. However, both changing the mesh size and using inviscid calculations may adversely influence the accuracy.

To verify the multilevel CFD approach for the Francis turbine design process, meshes with different sizes were generated based on the same runner geometry. CFD simulations were then performed on these meshes using both viscous and inviscid calculations. The mesh size information is given in table 9.1. The results from the different simulations are compared in the following sections.

Mesh	Nodes	Elements	$y_{max}^+$	$y_{min}^+$	$y_{avg}^+$
Fine	1113650	1055705	99.55	1.281	42.98
Coarse	102676	89245	757.0	16.13	315.9

Table 9.1: Mesh size information

## Fine Mesh

	Inviscid	Viscous
Head (LE-TE)	201.8710 m	200.0500 m
Total Efficiency (IN-OUT)	98.6627 %	97.8424 %

Table 9.2: Fine mesh simulation results

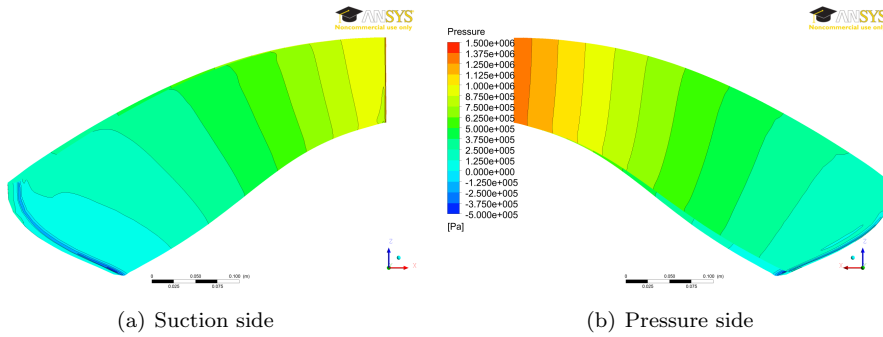


Figure 9.1: Static pressure on blade, viscous simulation results

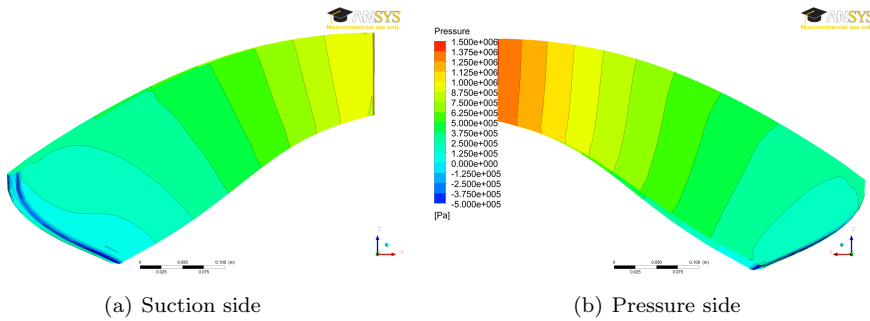


Figure 9.2: Static pressure on blade, inviscid simulation results



## Coarse Mesh

	Inviscid	Viscous
Head (LE-TE)	200.5760 m	200.9830 m
Total Efficiency (IN-OUT)	98.4175 %	97.5108 %

Table 9.3: Coarse mesh simulation results

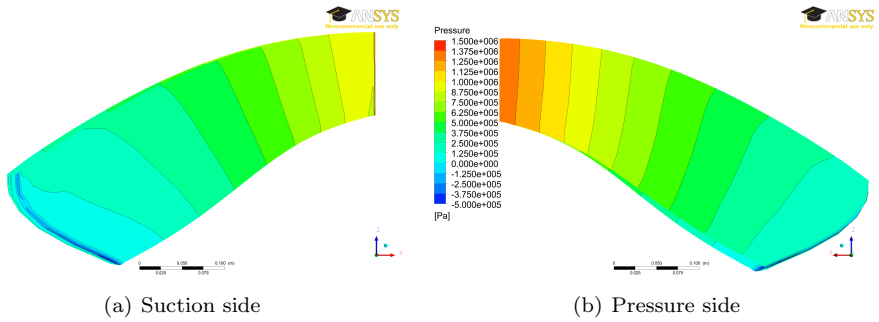


Figure 9.3: Static pressure on blade, viscous simulation results

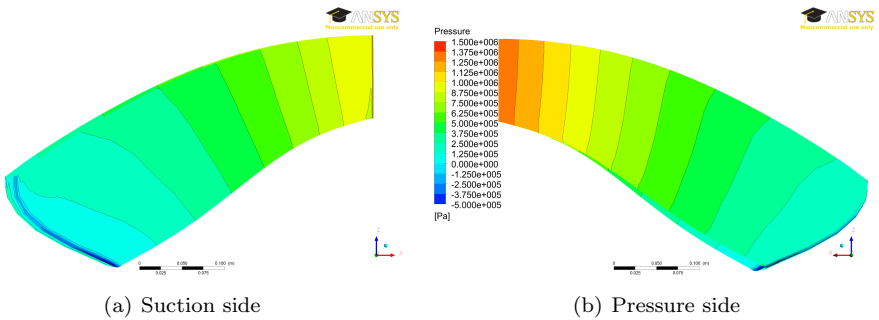


Figure 9.4: Static pressure on blade, inviscid simulation results

## Summary

Simulation time vary a lot, depending on mesh size and calculation method. To calculate the physics of the flow in the boundary layer the Shear Stress Transport (SST) turbulence model require  $y^+$  values of less than one. This is however hard to achieve, and require an extremely fine mesh, causing very time consuming simulations. According to Skaare [33, personal conversation], satisfactory simulation results for solving the flow conditions of a Francis turbine runner are obtained if the maximum value of  $y^+$  does not surpass 200. A mesh with approximately one million elements gives a maximum  $y^+$  value of 100, and a simulation time of approximately one hour. Inviscid simulations on coarse meshes have proven to repeat the same trends as viscous simulations on fine meshes do. Based on this, inviscid, coarse mesh simulations are found sufficiently accurate for the first stage of the optimization and also extremely time saving for the designer.

## 10 Parameter Study

The design software allows the designer to vary several parameters in order to generate different turbine designs. The first step of the parameter study is to map the effects of changing one parameter at the time.

Secondly, the joint effects of changing two or more parameters at the same time are studied. The combination of the parameters are selected based on the results of the single parameter study, but only the most promising combinations are investigated.

### 10.1 Control Variables for the Parameter Study

#### Submergence

Run-of-river scheme power plants seldom have a turbine submergence of more than ten meters [27, Personal conversations]. Six to eight meters below tail water level is relatively common, but the deeper the submergence, the higher is the development costs for the power plant. It is however important to remember that cavitation is more prone to occur on turbines operating in silty water (see section 4.2). Thus it may be necessary to submerge the turbine a bit more than what is calculated as required, as this value is valid for clean water operation only.

#### Speed number

The speed number should be found within the range where Francis turbines usually are chosen, which is in the interval between 0.2 and 0.8 [37]. For low speed numbers, the blades of a Francis turbine become relatively long, which implies an increase of friction losses. For speed numbers in the interval from 0.05 to 0.15 Pelton turbines are usually preferred, as Francis turbines generally have too high friction losses. In this case, however, where the aim is to reduce sediment erosion, the longer blades have an advantage because they reduce the maximum velocity of the flow. This reduces the erosion, meaning that Francis turbines should be considered as an alternative to Pelton turbines also for lower speed numbers.

#### Erosion Factor

Because it is desirable to reduce the sediment erosion of the turbines, a preliminary estimate of erosion is calculated based on the relative velocity through the runner. This parameter has been termed erosion tendency and defined as in equation 10.1.

$$E_t = \frac{\sum W_i^3 \cdot A_i}{\sum A_i} \quad [m^3/s^3] \quad (10.1)$$

$W_i$  is the relative velocity in each segment area  $A_i$  on the runner blade. Most erosion models give erosion as a term proportional to the relative velocity cubed. For this erosion tendency to give direct physical meaning, it has to be calibrated according to experimental or field data. Because such data was not available, an erosion factor was needed for comparing the erosion tendency of a new design to the erosion tendency of the reference design. The erosion factor is defined as shown in equation 10.2.

$$E_f = \frac{E_t \text{ New design}}{E_t \text{ Reference design}} \quad [-] \quad (10.2)$$

## 10.2 Single Parameter Studies

Six parameters were chosen for the single parameter study. These are listed in table 10.1 together with the range they are studied for. The number of blades is fixed to 17 blades, while the blade thickness is set to 15 mm at the leading edge and 8 mm at the trailing edge.

<i>Parameter</i>	<i>Symbol</i>	<i>Unit</i>	<i>Range of optimization</i>
Reduced peripheral velocity at inlet	$\underline{U}_1$	-	0.65 - 1
Outlet Diameter	$D_2$	m	0.4m - 0.75m
Number of pole pairs in the generator	$Z_p$	-	3-12 pairs
Acceleration of flow through runner	$Acc$	%	0-50 %
Blade height	$b$	m	0.05 m - 0.4m
Blade angle distribution	$\beta$	-	Five different shapes

Table 10.1: Parameters for single effects study

Table 10.1 shows that the number of pole pairs and the outlet diameter are chosen as design parameters. The reference design runner is generated to have the same dimensions as the existing turbines at Jhimruk HEC. Knowing the number of pole pairs and the outlet diameter, those parameters were used as input when establishing the reference design for the parameter study. For turbines intended for new sites, it is recommended to start the design procedure as explained in section 4.2.

### Effects of varying the outlet diameter

The outlet diameter affects all the velocity components at the outlet. Increasing the outlet diameter causes the peripheral velocity to increase, whereas the merid-

ional velocity component decreases due to continuity, as shown in figure 10.1. The relative velocity at the outlet is changed as a result of the changes in  $U_2$  and  $C_{m2}$ . The change in  $C_{m2}$  also causes a direct change of  $C_{m1}$  as the flow is accelerated from inlet to the outlet of the runner. The inlet peripheral velocity is held constant. Thus will a change in outlet diameter also cause a change in the relative velocity at the inlet. The changes in relative velocity at inlet and outlet are shown in figure 10.2.

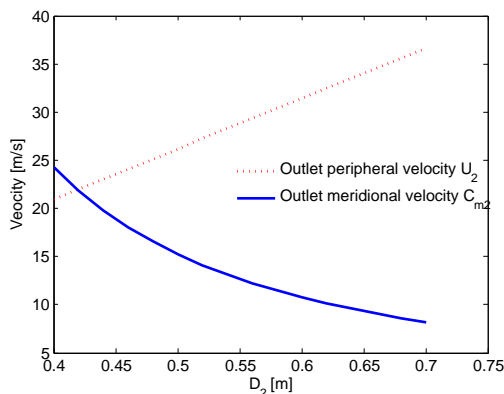


Figure 10.1: Effect on outlet peripheral velocity and outlet meridional velocity

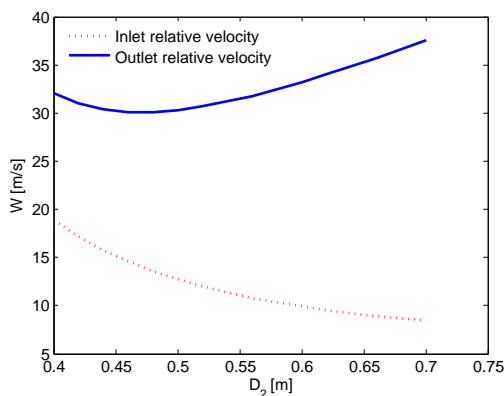


Figure 10.2: Effects on the inlet and outlet relative velocity

The changes shown in figure 10.2 also affect the erosion parameter as shown in figure 10.3. From the underlying data, a minimum value for the erosion factor is found for an outlet diameter of approximately 0.64 meters, given that the other design parameters are kept constant with respect to the reference design. Presumably will the erosion factor have a minimum value for one single outlet diameter

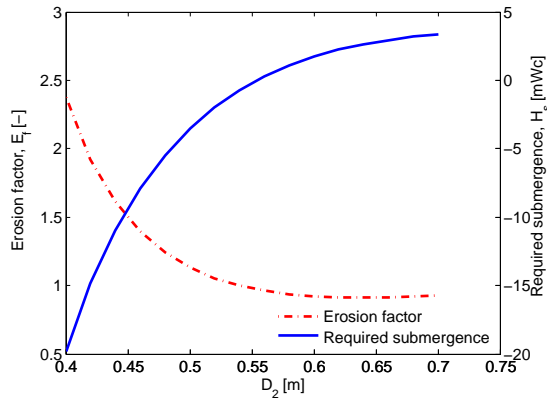


Figure 10.3: Effect on erosion factor and required submergence. Negative value of  $H_s$  means a placement below tail water level (see section 4.2)

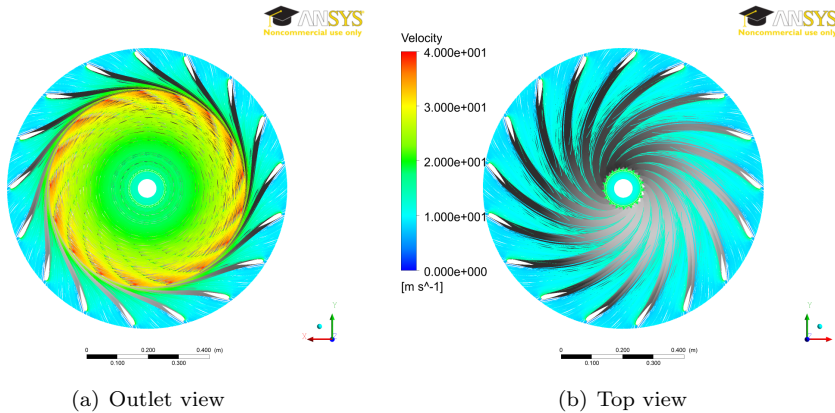


Figure 10.4: Relative velocity in runner seen from outlet and from top

for other combinations of the design parameters as well. How this lowest value of the erosion factor varies for other design parameter combinations is of interest to investigate when studying the joint effects of more parameters.

Figure 10.3 also shows how the required submergence of the turbine is affected when varying the outlet diameter.  $U_2$  increases for increasing values of the outlet diameter, whereas the  $C_{m2}$  component is decreasing. This yields  $NPSH_{required}$  to decrease, and thus  $H_s$  to increase, meaning that less submergence is required. The required submergence should not go below approximately minus 10 mWc. This limit is not surpassed for designs with an erosion factor ranging below 1.5, meaning that the submergence does not imply any constraints in this case.

Figure 10.2 shows that the relative velocity is lower at the inlet and higher at outlet

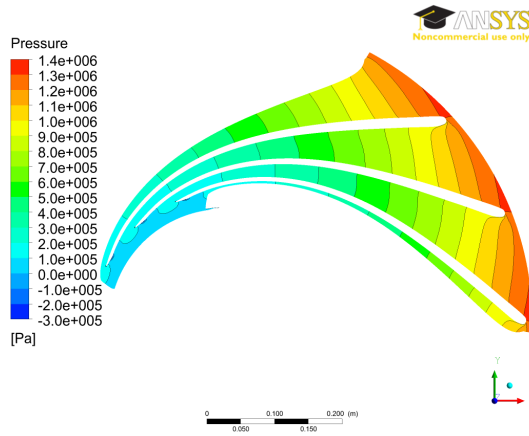


Figure 10.5: Blade to blade pressure distribution

	$D_2 = 0.64m$	<i>Ref. Design</i>	<i>Difference[%]</i>
Head (LE-TE)	201.6840 m	200.5760 m	0.55
Total Efficiency (IN-OUT)	97.4320 %	98.4175 %	1.00

Table 10.2: Simulation results  $D_2=0.64$  m

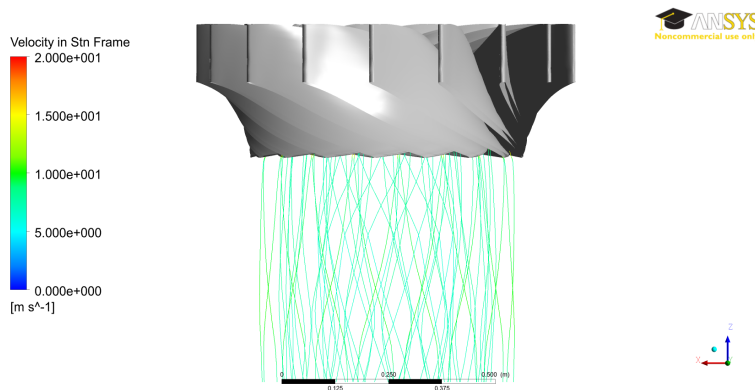


Figure 10.6: Draft tube flow conditions for  $D_2 = 0.64m$

than for the reference design when the outlet diameter is increased. Figure 10.4 confirms this for the design analysed with CFD.

The blade to blade pressure distribution, as shown in figure 10.5, is also as desired for a Francis runner. The contour lines are straight, which implies that no unfavourable flow conditions or swirls are present in the blade channels.

Figure 10.6 shows that the flow in the draft tube goes straight down with almost no swirl close to the draft tube wall. The swirl in the centre of the draft tube is generally considered harmless. The  $C_u$  component reported in CFX is negative, meaning operation slightly at part load like for the reference design. The value is closer to zero than for the reference design, and should thus yield a higher efficiency. The efficiency is however lower, as listed in table 10.2, which indicates that the reference design is hydraulically better than this design.

### Effects of varying the number of pole pairs

By choosing the number of pole pairs, you also choose the synchronous rotational speed of the unit. Increasing the number of pole pairs causes a reduction of rotational speed according to equation 10.3 where  $f_{grid}$  is the local grid frequency.

$$n = \frac{f_{grid} \cdot 60}{Z_p} \quad [rpm] \quad (10.3)$$

Reducing the rotational speed will also reduce the speed number. A speed number below 0.2 causes increased friction losses for a Francis turbine and is generally avoided. For speed numbers below 0.15, Pelton turbines are usually preferred. Figure 10.7 shows that the speed number will go below 0.2 for more than four pole pairs and below 0.15 for more than six pole pairs. This graph will be equal for all Jhimruk designs as the speed number is only dependent on head, flow rate and rotational speed. Considering a new design philosophy for reduction of erosion, it might however be favourable to allow a speed number below 0.2, and thus an increase in friction, if this implies a substantial reduction of erosion.

Decreasing the rotational speed will cause a reduction of  $U_2$ . If the blades were infinitely thin,  $C_{m2}$  would have been constant. Accounting for the blade thickness,  $C_{m2}$  is slightly decreased when the rotational speed is decreased, due to an increase

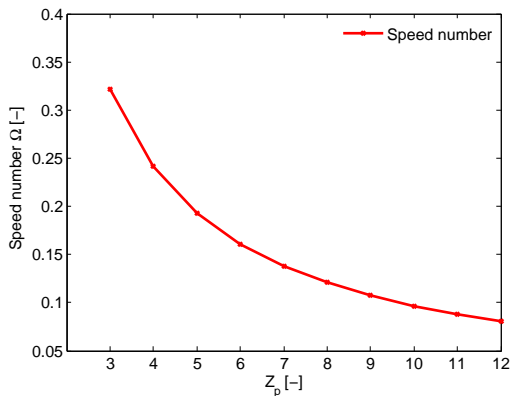


Figure 10.7: Effect on speed number



in effective outlet area, as shown in figure 10.8. This implies a reduction of the outlet relative velocity as well, because the change in  $U_2$  is much larger than the change in  $C_{m2}$ .

A continuity approach is applied to determine the inlet dimensions. Given a specified acceleration of the  $C_m$ -component through the runner,  $C_{m1}$  is changing in the same way as  $C_{m2}$ .  $U_1$  is fixed to the reference design value, causing the inlet diameter to increase when the rotational speed is decreased. Figure 10.8 shows that the change in  $C_{m2}$ , and consequently also the change in  $C_{m1}$ , is almost negligible when changing number of pole pairs. Due to continuity, this implies an almost constant inlet area. This means that the inlet height has to decrease for an increasing inlet diameter.

Reducing the outlet relative velocity is generally considered essential for reducing

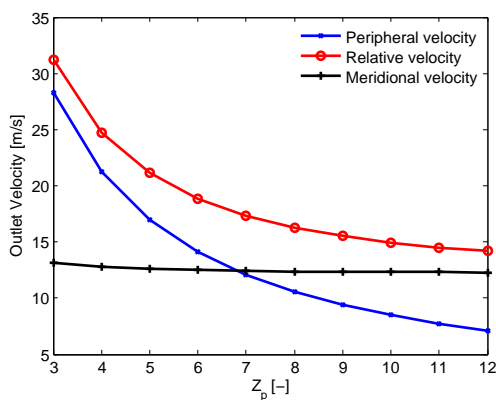


Figure 10.8: Effect on outlet velocity components

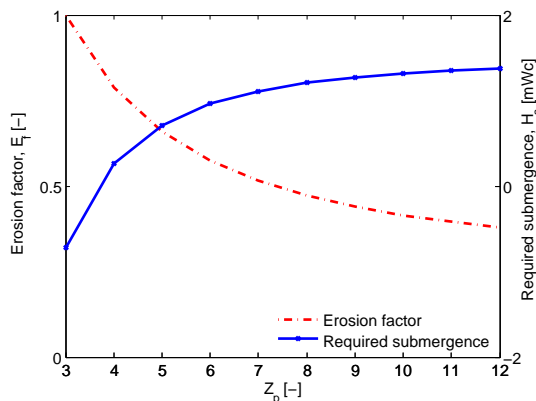


Figure 10.9: Effect on erosion factor and submergence requirements

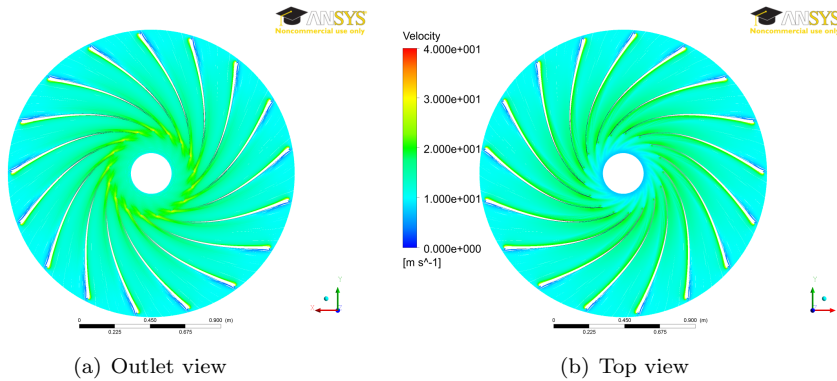


Figure 10.10: Relative velocity in runner seen from hub and from shroud

the erosion problem in turbines operated in silty water. Studying figure 10.8, we see that increasing the number of pole pairs, and with that reducing the rotational speed, will decrease the relative velocity at the outlet. Figure 10.9 shows how this reduction of relative velocity implies a substantial reduction of the erosion factor and a decrease in submergence requirements. This is confirmed by the CFD analysis, as shown in figure 10.10.

Six pole pairs were chosen for CFD investigation because the axial view got an unfavourable shape when surpassing this number and keeping the height  $b$  fixed to the reference design value. If increasing the height  $b$ , a further reduction of rotational speed is possible in terms of axial view layout. According to figure 10.9, the erosion factor is decreased even further when increasing the number of pole pairs to more than to six pairs. Thus, increasing both the height  $b$  and the number of pole pairs might be favourable for reducing erosion, and should be further studied.

The value listed for the  $C_u$  component in CFX is almost the same as for the reference design. The flow in the draft tube does however look like it goes almost straight down. The efficiency is slightly higher than for the reference design, as shown in table 10.3. The inlet height  $B_1$  is very small compared to the width of the channel at the inlet. In addition, the blade channel becomes long and wide compared to the height, when increasing the inlet diameter while keeping the height of the shroud  $b$  constant. This results in outer dimensions similar to a reversible pump turbine. The large inlet diameter also causes longer blades. Suspecting that the increased length of the blades compared to the reference design would yield large friction losses, a viscous simulation was performed, as the inviscid simulation does not take friction losses into account. That simulation did however disprove this assumption showing equally good results as the inviscid simulation. The viscous results are compared to a viscous simulation of the reference design in table 10.3. This proves that this design is hydraulically more promising and probably better than the reference design. Reducing the erosion at the same time, this will be interesting to combine with other parameters.

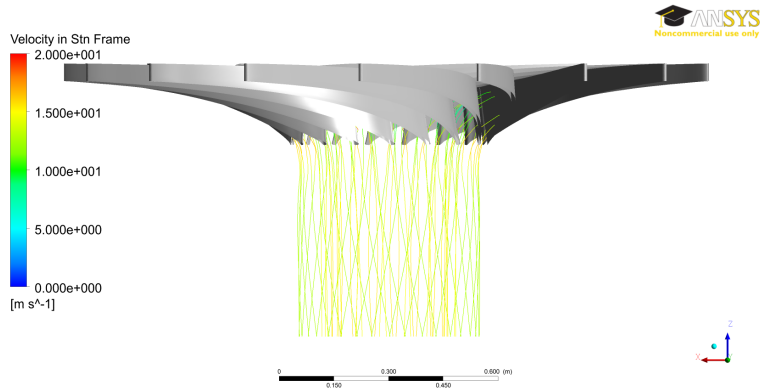


Figure 10.11: Streamlines in draft tube

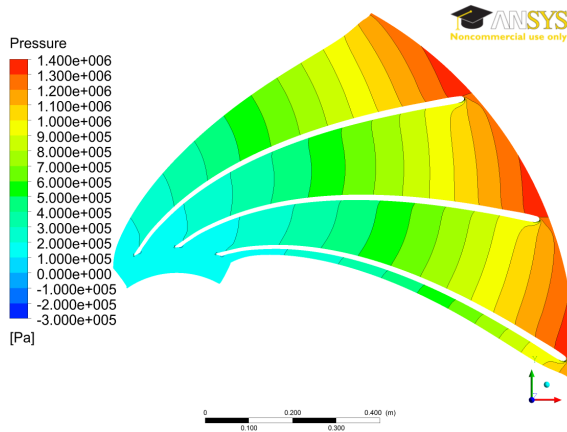


Figure 10.12: Blade to blade pressure distribution

It should however be taken into account that changing the number of pole pairs is a drawback if designing a new turbine for an existing power plant, as this implies that a new generator is needed. For new power plants, this is not a big issue, as a generator is needed anyway.

Figure 10.12 shows that the blade to blade pressure distribution has no unfavourable trends either. In addition, the negative pressure region which was present on the reference design trailing edge, is gone, implying that this blade is not prone to have cavitation problems. This confirms the required submergence calculated in the design software. Figure 10.9 shows that  $H_s$  is 0.96 mWc for six pole pairs, which implies that cavitation should not occur for a turbine placed at no more than 0.96 meter above tail water level.

	$Z_p = 6$	<i>Ref. Design</i>	<i>Difference[%]</i>
<i>Inviscid simulations:</i>			
Head (LE-TE)	201.6720 m	200.5760 m	0.55
Total Efficiency(IN-OUT)	98.8762 %	98.4175 %	0.47
<i>Viscous simulations:</i>			
Head (LE-TE)	201.7850 m	200.9830 m	0.40
Total Efficiency(IN-OUT)	97.8340 %	97.5108 %	0.33

Table 10.3: Simulation results six pole pairs

### Effects of varying the inlet peripheral velocity

Varying the inlet peripheral speed  $\underline{U}_1$  does not affect the outlet conditions, yielding a constant outlet velocity triangle and thus also constant submergence requirements. With constant discharge, head and rotational speed, the speed number is constant as well. Consequently, variations in  $\underline{U}_1$  only affects the reaction ratio, the inlet dimensions and the inlet velocity triangle.

Due to continuity, the inlet area is constant even though the inlet diameter is changing with  $\underline{U}_1$ . This implies that the inlet height has to increase for a decreasing inlet diameter, as can be seen in figure 10.13.

Studying the inlet velocity triangle, we see that a reduction in  $\underline{U}_1$  implies an increase of blade inlet angle. According to figure 10.14,  $W_1$  is decreasing when  $\beta_1$  approaches  $90^\circ$ . When  $\beta_1$  surpasses  $90^\circ$  the inlet relative velocity regains magnitude. A shift in inlet blade angle from below  $90^\circ$  to above implies a rather radical change to the runner blade. When studying the radial view, as shown in figure 10.15, we see that the blade curves in the opposite direction for  $\beta_1$  larger than  $90^\circ$  than the blade

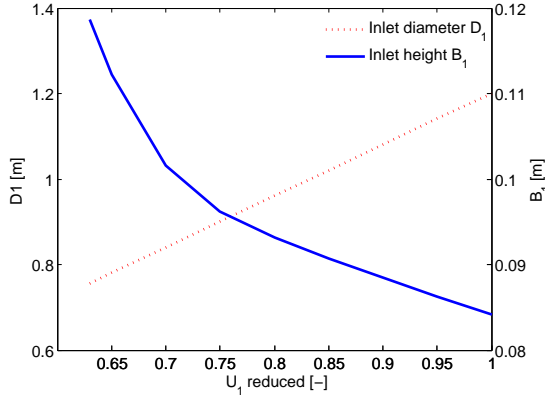


Figure 10.13: Effect on inlet height and inlet diameter

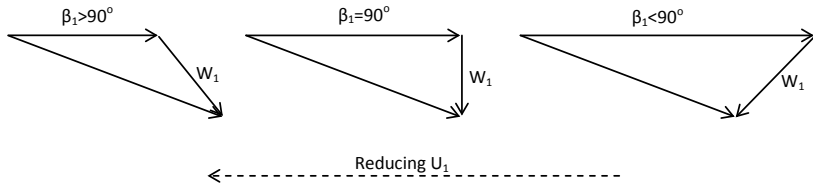


Figure 10.14: Effect on  $\beta_1$  and  $W_1$  when reducing  $\underline{U}_1$

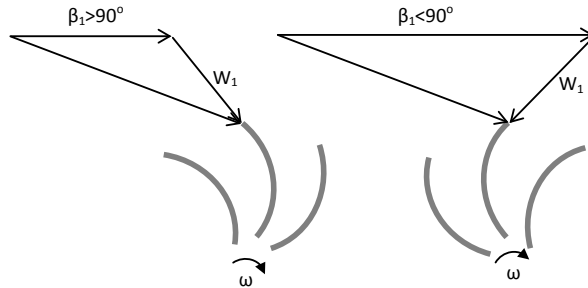


Figure 10.15: Effect on blade shape when reducing  $\underline{U}_1$ . (Blade shape at hub)

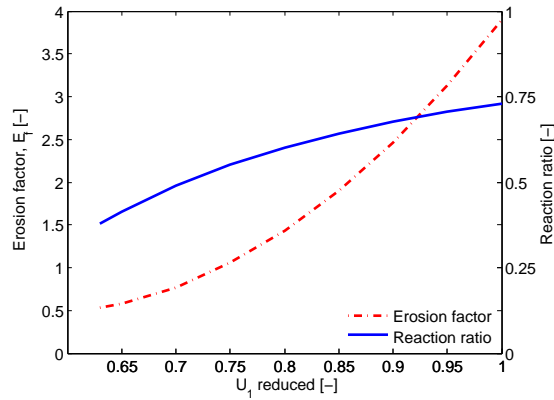


Figure 10.16: Effect on erosion factor and reaction ratio

does for traditional Francis runners with  $\beta_1$  less than  $90^\circ$ .

When the inlet peripheral speed is decreased compared to the reference design, the erosion factor is reduced. Decreasing  $\underline{U}_1$  also causes a lower value of the reaction ratio. This implies that the amount of pressure energy converted to mechanical energy in the turbine is reduced. If the turbine only converts kinetic energy into mechanical energy and no pressure energy is converted, the reaction ratio is zero. This is the case for Pelton turbines. For a Francis turbine, the reaction ratio is

usually found close to 0.5.

Figure 10.16 shows how the erosion factor decreases when  $\underline{U}_1$  is decreased, and that the curve flattens out for low values of  $\underline{U}_1$ . The reaction ratio is also decreased when decreasing  $\underline{U}_1$ , but for the reaction ratio the curve becomes steeper for lower values of  $\underline{U}_1$ . Choosing a Francis turbine runner design for low values of the reaction ratio should be done very carefully. According to Dahlhaug [27, personal conversations], designs with reaction ratios ranging below 0.3 should be thoroughly evaluated before they are chosen. This is however not an issue when  $\underline{U}_1$  is the only design parameter varied with respect to the reference design, because the reaction ratio is higher than 0.38 for all values of  $\underline{U}_1$  possible in the design software. For lower values of  $\underline{U}_1$ , the design software fails in producing a geometry. Decreasing the reaction ratio implies that more of the energy converted to mechanical energy in the turbine

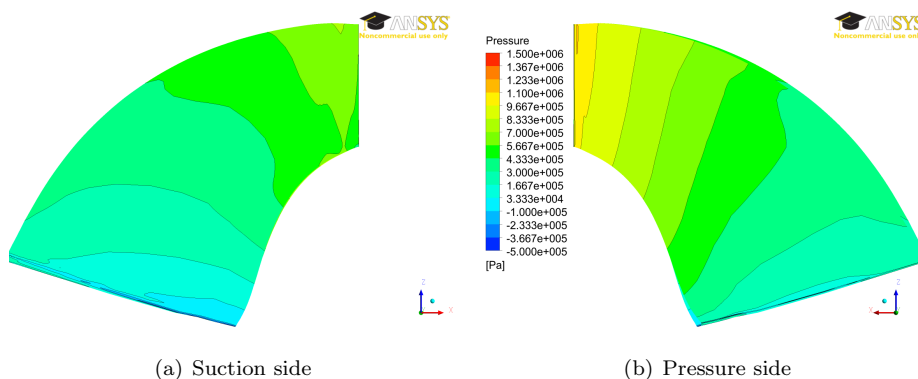


Figure 10.17: Pressure on the runner blades

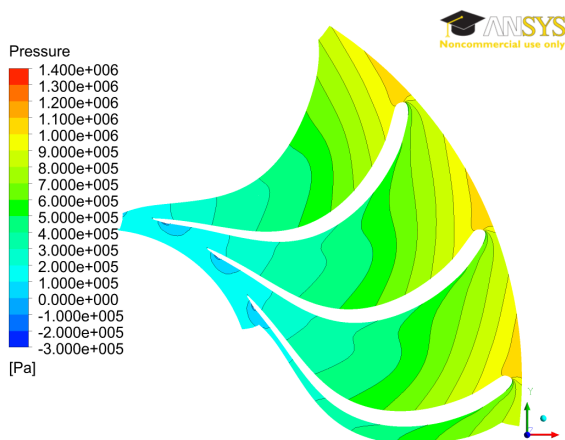


Figure 10.18: Blade to blade pressure distribution

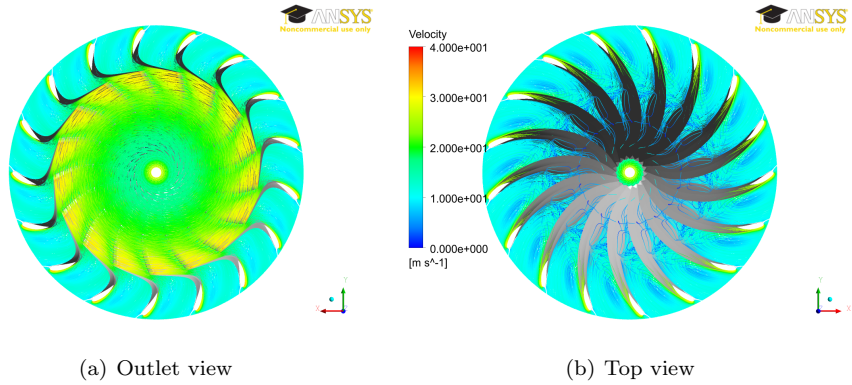


Figure 10.19: Relative velocity in runner seen from outlet and from top

	$\underline{U}_1 = 0.63$	<i>Ref. Design</i>	<i>Difference[%]</i>
Head (LE-TE)	201.1820 m	200.5760 m	0.30
Total Efficiency(IN-OUT)	97.3857%	98.4175 %	1.05

Table 10.4: Simulation results  $\underline{U}_1 = 0.63$

comes from kinetic energy. Studying the pressure distribution on the blades (see figure 10.17) and the blade to blade pressure distribution (see figure 10.18), we see that the pressure at the inlet is clearly lower than for the reference design. The shape of the pressure distribution contour lines, both on the blades and between the blades, is also quite different from the reference design. The wavy shape of the contours reveals that the flow might have unfavourable trends in this region. Because the flow goes from high to low pressure, the wavy contours are a sign of cross flows and swirls being present in the flow. This is confirmed by looking at the streamlines in the blade channel in figure 10.19. The swirl, which can be seen in figure 10.19(b), is harmful to the turbine, imposing more erosion. Looking at table 10.4, we also see that the efficiency is decreased compared to the reference design, probably because of the unfavourable flow conditions.

In the draft tube, the flow is well within an acceptable range in terms of rotation, and thus of no concern. The design is however not very favourable due to the swirl in the blade channel and consequently low efficiency. An investigation of how decreasing  $\underline{U}_1$  to some extent but not to the extreme end will affect the flow is of interest, and should be performed. How  $\beta_1$  affects the flow in the blade channel should also be investigated, in order to see if a inlet angle above  $90^\circ$  is unfavourable, or if some other limit exists.

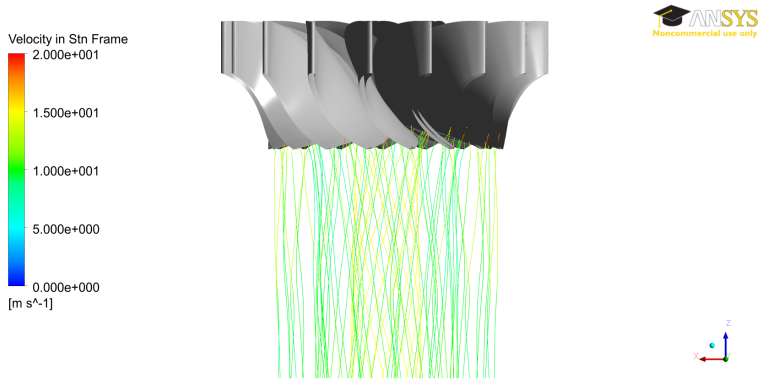


Figure 10.20: Streamlines in the draft tube

### Effects of varying the acceleration of the flow through the runner

Changing the acceleration through the runner cause a change in  $C_{m1}$ , as shown in figure 10.21. Due to continuity, this causes a change in inlet area. With a constant inlet diameter, the change in inlet area has to be accounted for by changing the inlet height.  $\underline{U}_1$  and  $C_{u1}$  are unaffected by the changes in how much the flow is accelerated through the runner. The change in  $C_{m1}$  only influences the absolute velocity  $C_1$  and the relative velocity  $W_1$ .

With constant outlet conditions, the erosion factor is only dependent on the inlet conditions and the blade angle distribution. For a high acceleration, the inlet relative velocity is decreased, and for a constant blade angle distribution, the erosion factor is decreased too. Studying figure 10.22, the trend shows that increasing the acceleration above 50 % would probably reduce the erosion further, but to achieve

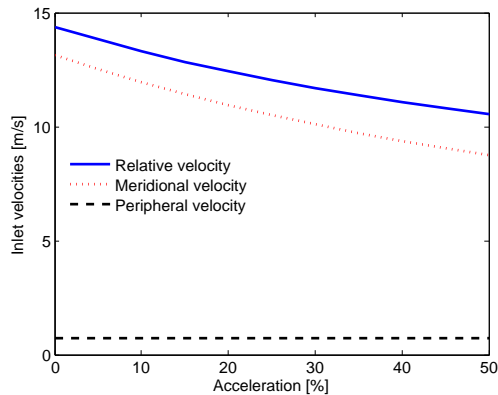


Figure 10.21: Effects on inlet velocities



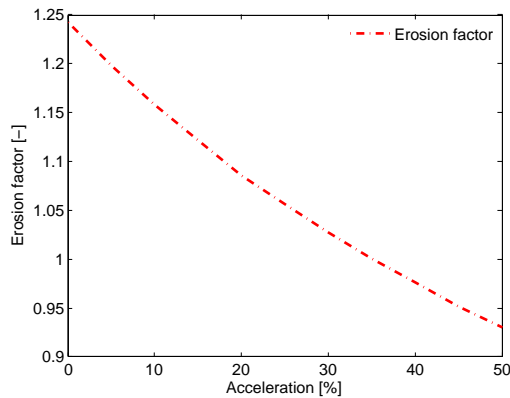


Figure 10.22: Effect on erosion factor

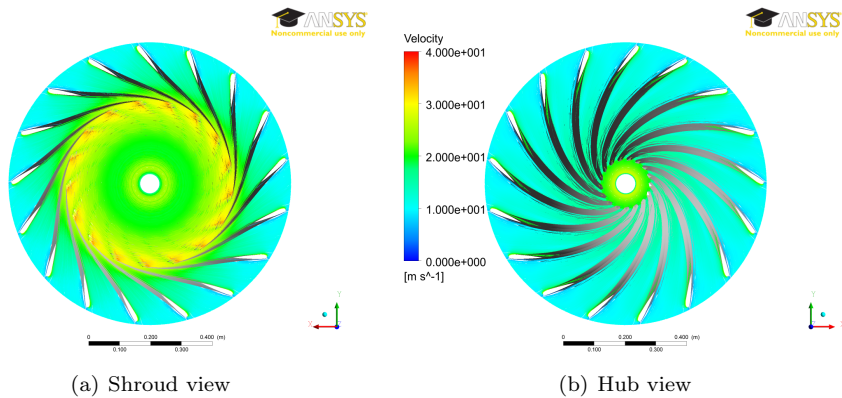


Figure 10.23: Relative velocity in runner seen from hub and from shroud

a substantial reduction in erosion factor just by changing the acceleration would demand a very high acceleration of the flow. This may affect the number of blades required to avoid backflow in the runner, as this is dependent on the magnitude of the relative velocity in the inlet region.

Comparing the CFX results for the turbine with 50 % acceleration and the reference design turbine, both the relative velocity in the runner and the blade to blade pressure distribution are very similar. (See figures 8.3 and 10.23 and figures 8.5 and 10.24.) With similar turbine dimensions as well, the manufacturing cost will also be more or less equal. Taking into concern that the head of the reference design is further off the design head than this design and that the efficiency is higher, it is probable that the reference design is hydraulically better than this design. The differences are however small, and might be acceptable if erosion is reduced.

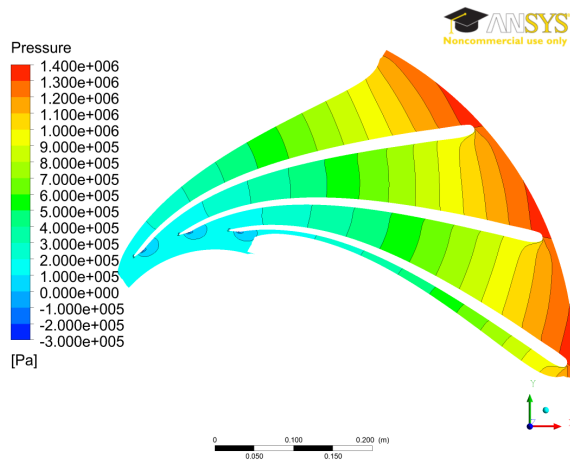


Figure 10.24: Blade to blade pressure distribution

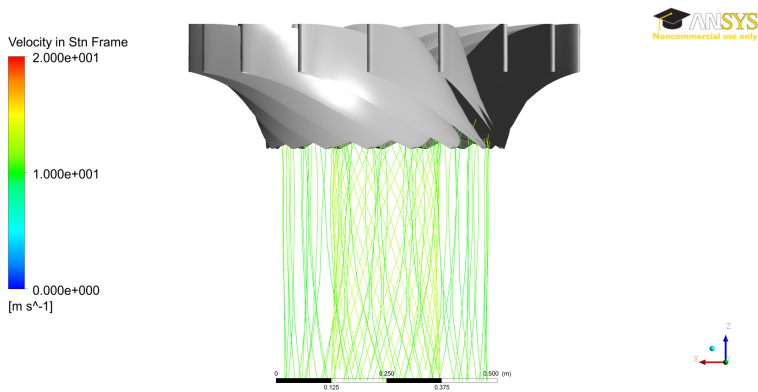


Figure 10.25: Streamlines in the draft tube

	<i>Acc = 50%</i>	<i>Ref. Design</i>	<i>Difference[%]</i>
Head (LE-TE)	201.0940 m	200.5760 m	0.26
Total Efficiency(IN-OUT)	98.2362%	98.4175 %	0.18

Table 10.5: Simulation results *Acc=50%*

### Effects of varying the height $b$ of the runner

When the main dimensions are determined, the shape of the runner's axial view has to be decided. The outlet and inlet diameter and the inlet height are given from the main dimensions, whereas the height difference from inlet to the outlet

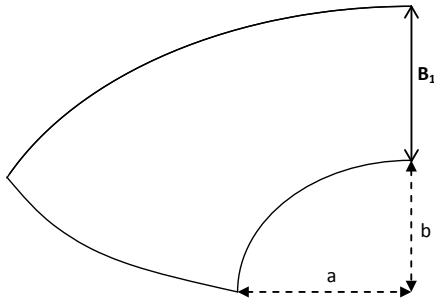


Figure 10.26: Definition of height  $b$

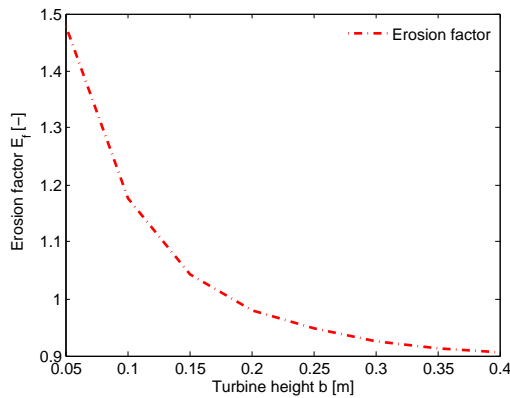


Figure 10.27: Effect on erosion factor

at the shroud  $b$ , as shown in figure 10.26, has to be chosen.

Changing the runner height  $b$  will not change the remaining main dimensions. The erosion factor is however affected. Choosing the value of  $b$  higher than the difference in inlet and outlet radius  $a$ , gives a lower erosion factor, whereas a lower value of  $b$  cause an increase in erosion factor, as shown in figure 10.27. This is due to the fact that a higher value of  $b$  will cause longer blades and thus a lower erosion factor as discussed earlier. According to this figure, the height  $b$  affects the erosion factor more in a negative manner if choosing a too low value than it improves the erosion factor when increasing  $b$ .

CFD analysis is performed for a runner with height  $b$  equal to 0.4 m. This is more than twice the difference between inlet and outlet radius, which is quite extreme. In figure 10.30, which show the pressure distribution between the blades on 50 % span between hub and shroud, we see that the blades curve a lot close to the trailing edge. Despite of that, the pressure distribution looks good. However, studying the pressure distribution on the blades in figure 10.28, we see that in the region where the blades curve a lot the pressure contour lines are quite wavy near the hub and

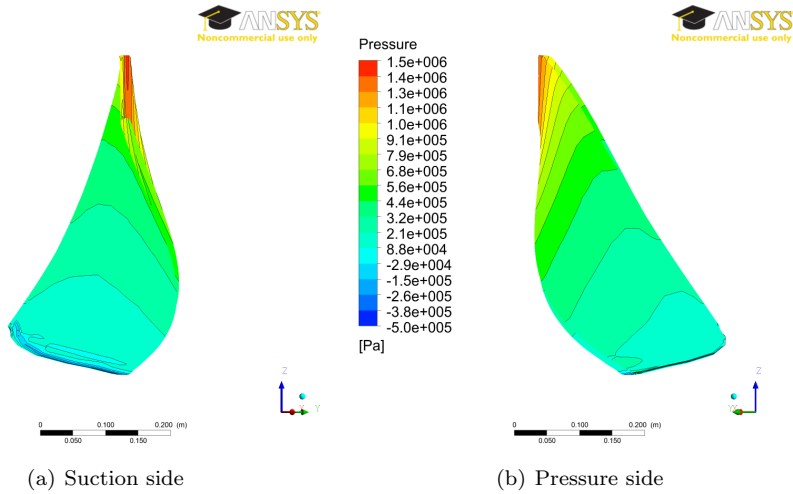


Figure 10.28: Pressure contours on runner blade. The blade are turned so that the trailing edge area close to the hub are visible

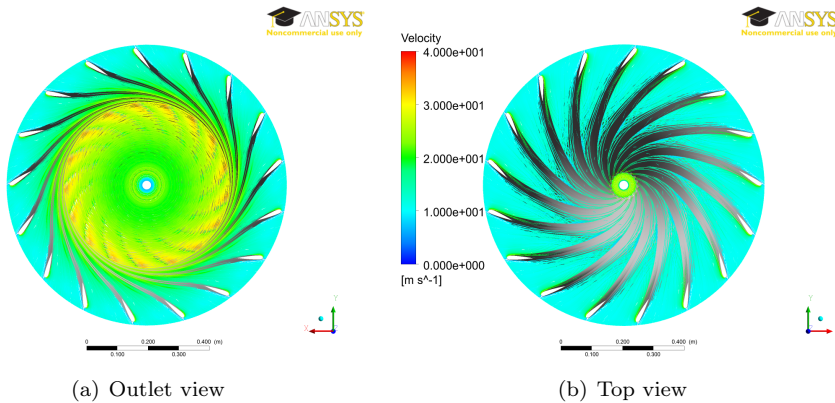


Figure 10.29: Relative velocity in runner seen from outlet and from top

	$b=0.4 \text{ m}$	<i>Ref. Design</i>	<i>Difference[%]</i>
Head (LE-TE)	201.6870 m	200.5760 m	0.55
Total Efficiency(IN-OUT)	98.0100%	98.4175 %	0.41

Table 10.6: Simulation results  $b=0.4 \text{ m}$

shroud, imposing unfavourable flow conditions in these regions. Looking at the relative velocity in figure 10.29, we see that a swirl appear in the same area as the wavy pressure contours.

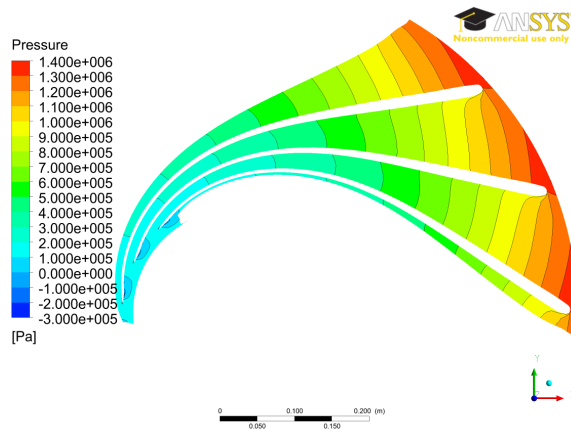


Figure 10.30: Blade to blade pressure distribution

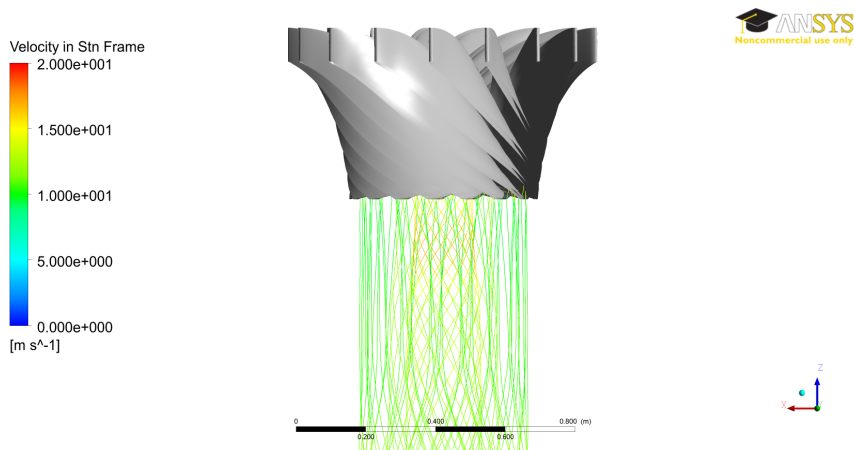


Figure 10.31: Streamlines in the draft tube

A small but harmless swirl is present in the middle of the draft tube. Close to the walls of the draft tube is the flow going straight down, imposing no BEP operation concerns. The efficiency is lower than for the reference design when changing the height  $b$  to the extreme end of what is possible to import and mesh with TurboGrid. This implies that such a large change in  $b$  is not hydraulically favourable. The effect on the erosion factor is not too strong either, and it seems like small changes of the height are best suited in combination with changing other parameters.

## Effects of varying the shape of the blade angle distribution

From the main dimensions, the inlet and outlet blade angles are fixed. According to section 4.3, the distribution of the blade angles in between has to be determined. This can be done in two ways; either by specifying the blade angle distribution or by specifying the energy distribution. For the parameter study, specifying the blade angle distribution was chosen.

The five different shapes plotted in figure 10.32 were chosen for the parameter study. Shape 3 is the distribution used for the reference design. (Results of a viscous CFD simulation are found in chapter 8.) Shape 1 and shape 2 are the extreme variants of the blade angle distribution, compared to the reference design. They also have the highest and lowest erosion factors respectively, as shown in figure 10.33.

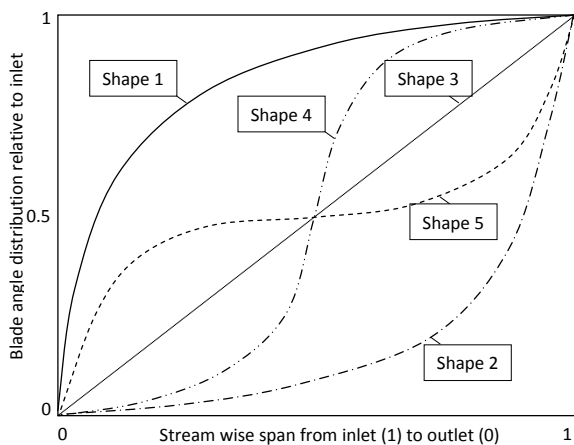


Figure 10.32: Different shapes of the blade angle distribution for the parameter study

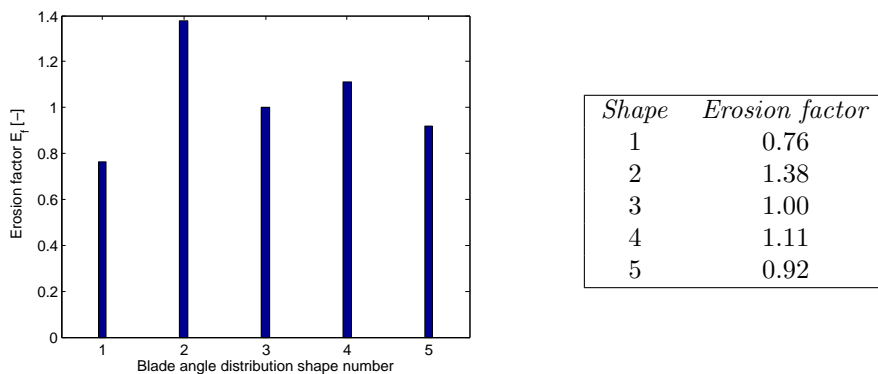


Figure 10.33: Erosion factor for different shapes of the blade angle distribution

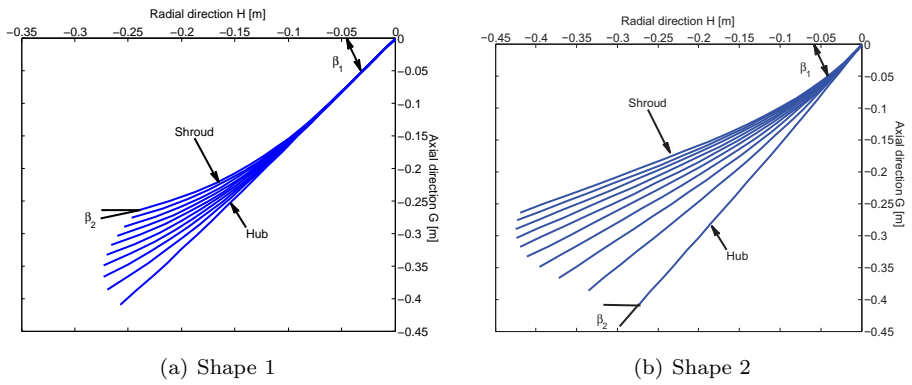


Figure 10.34: GH-plane plots for different blade angle distributions

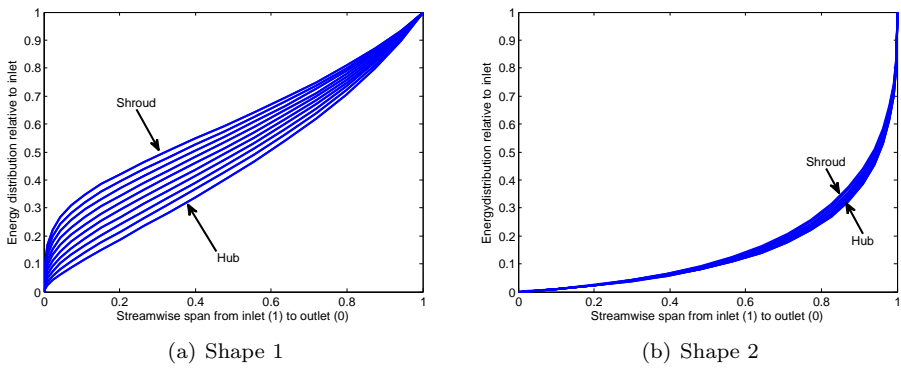


Figure 10.35: Energy distributions for different blade angle distributions

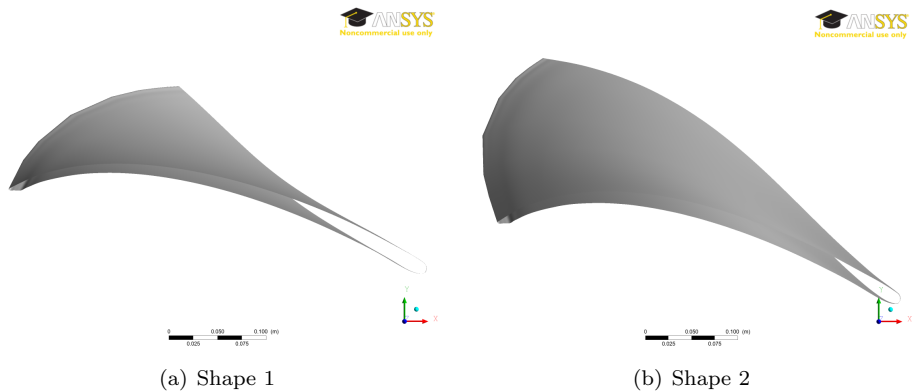


Figure 10.36: Shape of the blade for different blade angle distribution

Due to the different radius at the hub and at the shroud, the outlet angles are different for each streamline as shown in the GH-planes in figure 10.34. (See chapter 4.3 for definition of the GH-plane.) This causes a different energy distribution for each streamline. The energy distribution is actually the distribution of the product of  $U$  and  $C_u$ . The  $C_u$  component is strongly correlated to the blade angle distribution, whereas  $U$  is only dependent on rotation and radius. Due to this, the energy distribution is somewhat correlated to the blade angle distribution. The correlation is easiest to see in figure 10.35(b). The energy distribution is not similarly correlated for shape 1, as shown in figure 10.35(a). This is due to the peripheral velocity, which is decreasing for when the radius is decreased. This causes the energy (the  $U \cdot C_u$ -product) to decrease as well.

Different shapes of the blade angle distribution cause energy conversion in different parts of the turbine, as shown in figure 10.35. The different blade angle distribution also causes different transition from inlet to outlet velocity, which explains the difference in erosion factors.

In terms of energy conversion, shape 1 implies that most of the energy is converted from halfway through the runner to the trailing edge, whereas shape 2 implies that most of the energy is converted from the inlet to halfway through the runner. Traditionally, a shape similar to shape 2 is chosen. For this shape, the blades are chosen thicker at the leading edge, and gradually thinner towards the trailing edge.

Changing the blade angle distribution causes the entire shape of the blade to change, and the effect on the shape is relatively large. Figure 10.36 shows the shape of the blades for the two extreme ends of the blade angle distribution; shape 1 and shape 2 (see figure 10.32). For shape 1, the blade has no curvature at the inlet, whereas shape 2 curves a lot close to the inlet. Consequently, to have equal change in blade angle from inlet to outlet, the shape 1 blade curves a lot in the section close to the trailing edge, whereas the blade with shape 2 curves almost nothing in this region.

Based on the low erosion factor, CFD analysis is only performed for a design with blade angle distribution shape 1. Shape 1 implies that the relative velocity is kept low, only increasing slightly as  $C_m$  increases due to acceleration. This causes a low erosion factor. The shape does however imply a large acceleration of the relative velocity and a large deceleration of both the peripheral velocity and the  $C_u$  component at the last part of the blade. This implies that most of the energy is converted at the end of the blade, where the blade traditionally is at its thinnest. Strength analysis (Finite Element Method (FEM) and Fluid Structure Interaction (FSI)) has to be performed to determine if the blade is strong enough to handle the forces. If such analysis shows that the blade fails, a more moderate shape of the blade angle distribution or another thickness distribution has to be chosen for the blade. Due to strength concerns, a thicker blade might be favourable at the trailing edge. In addition, the number of blades required should be evaluated using CFD.



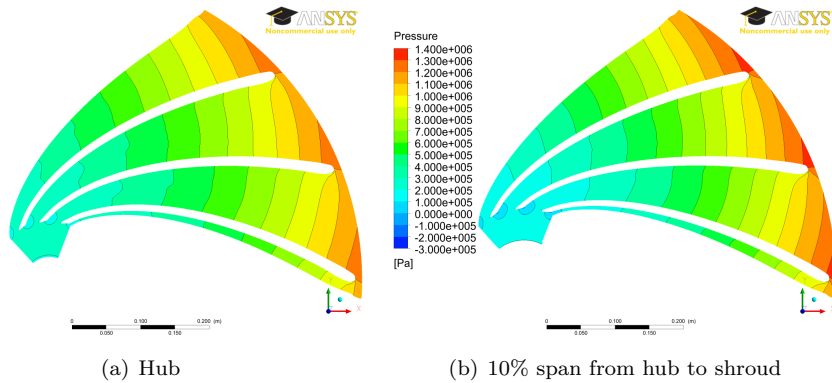


Figure 10.37: Blade to blade pressure distribution

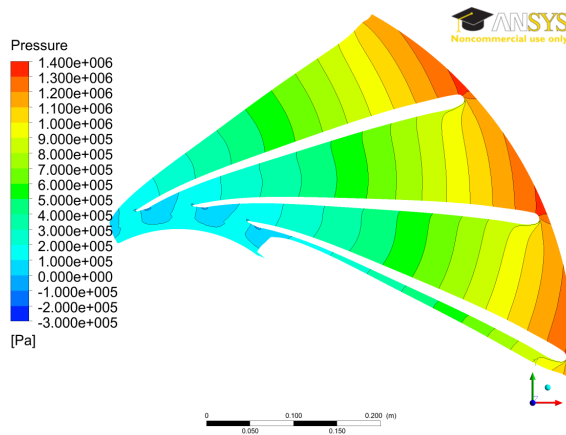


Figure 10.38: Blade to blade pressure distribution for  $\beta$ -distribution shape 1 at midway from hub to shroud

Studying the blade to blade pressure distribution at the hub, as shown in figure 10.37(a), we see that the contour lines from the inlet to halfway through the runner are straight and as desired. From halfway through the runner and to the outlet, the contour lines are wavy. The pressure distribution in this region causes the flow to stream from the pressure side towards the suction side. Studying the blade to blade pressure contours in the blade channel at 10 percent span from the hub, as shown in figure 10.37(b), we see that the contour lines are almost straight. In the middle of the channel, midway between hub and shroud, as shown in figure 10.38, the contours are acceptably straight. Thus are the unfavourable flow conditions only found at the upper 10 percent of the channel, and small modifications to the geometry might reduce this.

The transition of the relative velocity from inlet to outlet behaves as predicted by

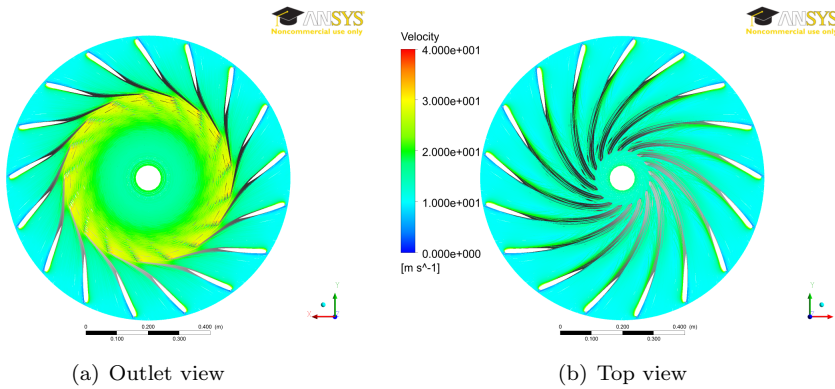


Figure 10.39: Relative velocity in runner

	<i>Shape 1</i>	<i>Ref. Design</i>	<i>Difference[%]</i>
Head (LE-TE)	201.5830m	200.5760 m	0.50
Total Efficiency(IN-OUT)	98.5984%	98.4175 %	0.18

Table 10.7: Simulation results  $\beta$ -distribution shape 1

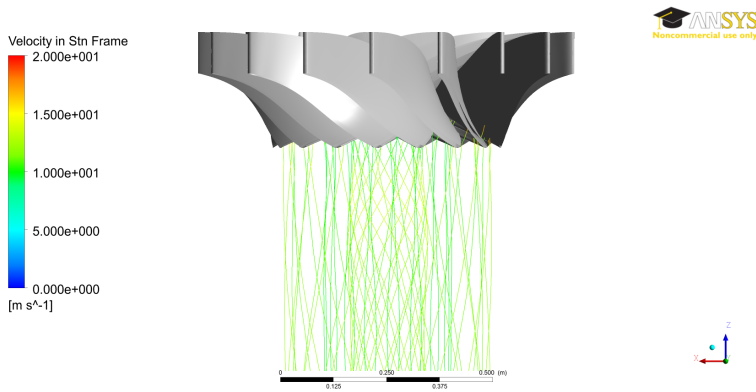


Figure 10.40: Streamlines in the draft tube

the design software, with low acceleration in the inlet region for shape 1 and high acceleration of the flow in the outlet region as shown in figure 10.39. in the outlet region close to the hub, as shown in figure 10.39(b), indications of a small swirl is visible, as predicted when looking at the pressure distribution at the hub.

At the trailing edge, CFX gives a positive value for the  $C_u$  component at the reference diameter, implying operation slightly at overload condition. Studying the streamlines in the draft tube, we see that the streamlines close to the walls

rotate in the opposite direction of the streamlines in the centre. Consequently, the flow goes straight down somewhere in between. The hydraulic efficiency is slightly higher than for the reference design, implying a better hydraulic performance. The energy lost in the draft tube due to the  $C_{u2}$  component, calculated according to equation 8.1, is relatively low, only 1.17 mWc.

### 10.3 Selective Parameter Studies

For the selective parameter study, the joint effects of changing two or more design parameters at a time are studied. The combinations are chosen based on the results of the previous section.

When designing a turbine for an existing power plant, it has to be decided whether to reuse some of the old equipment or to design the entire turbine as if it was for a new site. In such case, there are different options:

- Keep all outer runner dimensions as for the existing runner. This implies that only the blade angle distribution and thus the energy distribution may be changed. This has been studied in the previous section and found to yield a reasonably good reduction of the erosion.
- Keep the rotational speed, and consequently use the old generator.
- Design the entire turbine from scratch. This allows decreasing the rotational speed of the unit.

#### Selective design no.1:

#### Six pole pairs and blade angle distribution shape 1

Allowing to change the rotational speed compared to the reference design, six pole pairs were chosen in combination with blade angle distribution shape 1. Six pole pairs imply a rotational speed of 500 rpm, which is half the reference design rotational speed. For this combination, the erosion factor was reduced from the reference design erosion factor of 1 to 0.5.

CFX results show that all the streamlines rotate the same way in the draft tube, as shown in figure 10.41. This is due to the negative value of  $C_u$ , as listed in table 10.8,

	<i>Selective design no.1</i>	<i>Ref. Design</i>	<i>Difference[%]</i>
Head (LE-TE)	200.5360 m	200.5760 m	0.04
Total Efficiency (IN-OUT)	98.7349%	98.4175 %	0.31
$C_u$ (TE cut)	-2.2910 m/s	0.6686 m/s	0.31

Table 10.8: Simulation results selective design no. 1

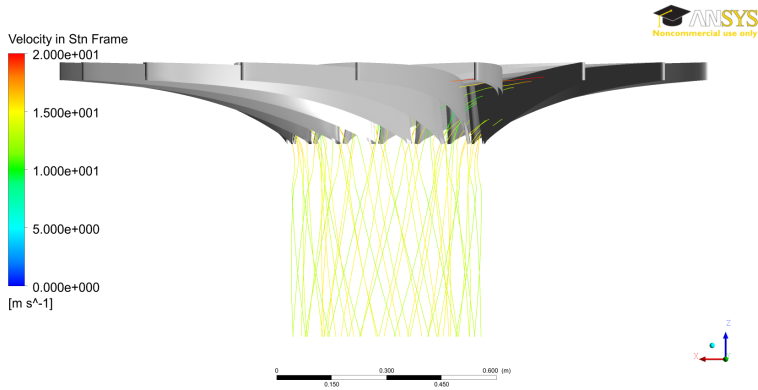


Figure 10.41: Flow in the draft tube

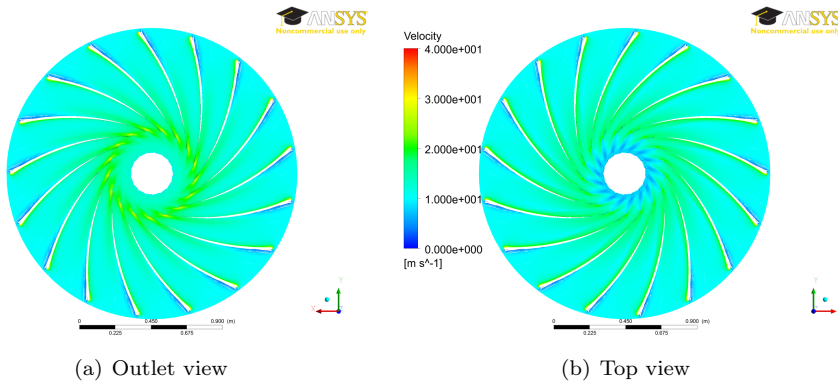


Figure 10.42: Relative velocity in runner

meaning that the turbine actually operates on part load conditions for the design head. The energy loss is however only 0.52 mWc according to equation 8.1.

Compared to the reference design, the reaction ratio is the same, but the inlet relative velocity is slightly decreased for this design. At the outlet, the relative velocity is decreased a lot compared to the reference, from 31.2 m/s to 18.9 m/s. Flow patterns and pressure distributions for the design look very good with no unfavourable trends. With a substantial reduction of erosion and a better hydraulic efficiency than for the reference design, this design is considered as one of the better this far in the design process. The drawbacks of this geometry are the large inlet diameter (1.78), which is twice the reference design inlet diameter, and the generator size and cost which is increased too.

**Selective design no. 2:**

$U_1$  equal to 0.71 and blade angle distribution shape 1

Keeping the rotational speed fixed at 1000 rpm as for the reference design a selective design combining variations in some of the other design parameters were tested. Even though the efficiency of the design generated by changing  $U_1$  was quite low, compared with the reference design, it was desirable to see if that could be improved by changing the blade angle distribution too. The erosion factor for this design is only 0.61, yielding a substantial reduction of the erosion.

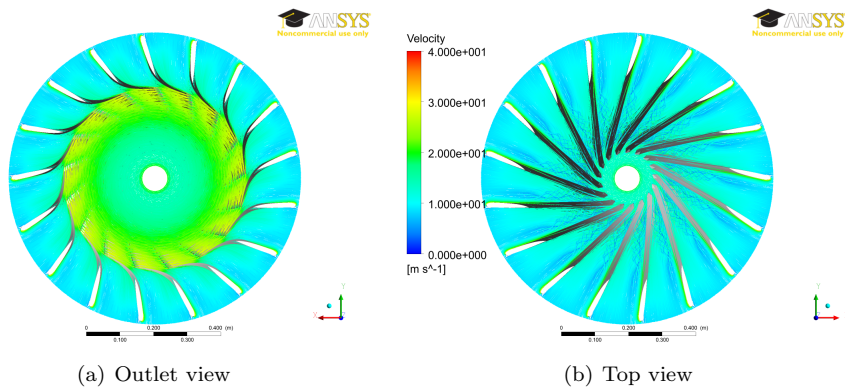


Figure 10.43: Relative velocity in runner

CFD results show that a swirl is present in the blade channel. This can be seen in figure 10.43(b). Taking the swirl into account, the efficiency is relatively high, as can be seen in table 10.9. If minor changes to the geometry can remove the swirl and still keep the erosion factor low and the efficiency high, this will be a very favourable design.

	<i>Selective design no.2</i>	<i>Ref. Design</i>	<i>Difference[%]</i>
Head (LE-TE)	201.457 m	200.5760 m	0.04
Total Efficiency (IN-OUT)	98.2041%	98.4175 %	0.31

Table 10.9: Simulation results selective design no. 2



# 11 Discussion

## 11.1 Design Software

The design software has proven to generate designs with acceptably good hydraulic performance, especially when trying to generate traditional geometries. This is however only valid for BEP operation as part load and full load conditions have not been simulated using CFD. This would be necessary in order to verify the geometry for the full range of operation conditions. Better control of the pressure distribution from hub to shroud would also be favourable.

### Erosion estimate

In need of a preliminary estimate of erosion in the design software, the erosion tendency was implemented. This parameter is calculated as explained in chapter 10.1. The model chosen were based on the fact that erosion is proportional to the velocity cubed in most erosion models.

Having established the reference design, the erosion factor, which indicates whether a new design will have a higher ( $E_f > 1$ ) or lower ( $E_f < 1$ ) erosion tendency than the reference design were implemented.

A verification of the erosion factor using results from erosion simulations in CFX was intended, but having problems with mesh dependency for the erosion rate, and especially for the fine meshes, the verification was not fulfilled as part of this thesis. Verification should be done if further work will be based on this factor.

The model used to calculate the erosion tendency should also be further evaluated. Today's model does not take the location of the high and low relative velocities into account, meaning that it does not take the location of the erosion into account either. Thus can a very high relative velocity at the outlet, giving heavy local erosion, have a lower erosion tendency than a blade with more uniform erosion all over the blade. This has to be taken into account, and it has to be decided which scenario that is worse. A heavy local erosion might be easier to repair by welding than a uniform erosion all over the blade. Thus, the uniform erosion might be more fatal for the runner. Today's method gives a measure of the overall erosion. If the heavy local erosion is considered as a more fatal scenario, a new method taking location into account might be desirable.

## 11.2 The Reference Design

The outer dimensions are the same for the reference design as for the existing runners at Jhimruk. However, knowing neither the blade angle distribution, nor the energy distribution of the blades, it was an impossible task to design a reference runner exactly equal to today's Jhimruk runners. Having no experience in how the

blade angle distribution looks like for a traditional Francis turbine, a distribution with a linear shape (shape 3 in figure 10.32) was chosen based on recommendations from Dahlhaug [25]. In addition, CFD results for the design with a linear shape of the blade angle distribution were sufficiently good for a reference design.

The existing runners at Jhimruk have splitter blades with 15 long and 15 half-length blades. It would have been desirable to model the reference design runner with splitter blades as well but splitter blades have not been implemented in the design software due to time limitations. Consequently, only ordinary, full length blades are used. The number of blades was not taken as a variable design parameter, but chosen based on experience [27, personal conversations]. According to Dahlhaug, 15 blades will yield a narrow efficiency curve, meaning that the turbine is not suited for operation off design load. On the other side, 19 blades cause a very tight outlet of the runner. Hence, 17 blades were chosen.

If the reference runner was modelled with splitter blades, the blade thickness should have been modelled equal to the existing runners. However, not knowing the existing blade thickness and because the chosen number of blades are lower than for the existing runners, the blade thickness only has to be chosen such that the blades can withstand the hydraulic forces acting on them, and thick enough to meet manufacturing requirements. The method used for calculating the runner blade thickness gave very thin blades, approximately 6-8 mm at the inlet. According to Dahlhaug [27, personal conversations], the calculated value was too thin, especially for operation in silty water, but also in a manufacturing point of view. As the method consistently gives too thin blades, a constant value were chosen and applied for all designs. Consequently, 15 mm were chosen for the inlet, whereas a thickness of 8 mm was chosen at the trailing edge. A gradually tapering of the blade is done in between. Strength analysis (FEM and FSI) will be necessary to determine if the blades are thick enough to withstand the forces. A thicker blade will disturb the flow more, causing larger wakes behind the trailing edges, and consequently less favourable flow conditions in the draft tube.

### 11.3 Single Parameter Study

The single parameter study is based on the reference design. The effects of changing one parameter at the time with respect to the reference design are mapped. The first stage of the parameter study was performed using the design software. Each design parameter was varied with respect to the reference design. For all values tested, the effects on other parameters, such as velocities, inlet diameter, inlet height and the erosion factor were mapped.

CFD simulations were performed for the parameter value giving the lowest value of the erosion factor. For most of the parameters, that minimum erosion factor was found at one of the extreme ends of the test range. It is likely that the extreme end value causes a design with unfavourable flow conditions and low efficiency, whereas a design with high efficiency and acceptably low erosion might be found in between



this extremity and the reference design value. It was also evident that some of the parameters did not affect the erosion factor a lot alone, but that they might make an important contribution in combination with changing other parameters.

### **Changes to the number of pole pairs**

Increasing the number of pole pairs seems to be the best way of reducing the erosion. This is coincident with recommendations from other researchers as well [38, 23]. CFD results show that this turbine has the highest efficiency amongst the designs analysed. However, the longer blades were thought to cause relatively large friction losses, which were not accounted for in the inviscid analysis. Hence, a viscous simulation was performed, showing that the losses were acceptably low, and that still the efficiency was higher than for the reference design (viscous simulation results).

Another drawback of increasing the number of pole pairs is the increase in size and price for the generator. In the case of Jhimruk, a new generator is needed if changing the rotational speed.

### **Changes to the reduced inlet peripheral velocity, $\underline{U}_1$**

Based on the design software results,  $\underline{U}_1$  seemed to be the second most efficient design parameter to vary in terms of reducing sediment erosion. Decreasing  $\underline{U}_1$  does however affect the blade shape quite a lot, as illustrated in figure 10.14 and figure 10.15.

The design analysed with CFD in the single parameter study had an inlet angle of approximately  $150^\circ$ , and thus a quite untraditional shape of the blade. Because of the swirl that appeared in the CFD results for this design, and the fact that decreasing  $\underline{U}_1$  only a little would also yield a relatively high reduction of erosion, a design with an  $\underline{U}_1$  value giving an inlet blade angle of  $90^\circ$  was analysed. This design did however also show a swirl in the blade channel.

Brekke [21] recommends a value of  $\underline{U}_1$  in the interval from 0.70 to 0.76 for Francis turbines. For high head turbines in particular, a value between 0.71 and 0.73 is recommended in order to minimize the impact losses. The swirl was still present for  $\underline{U}_1$  equal to 0.70.

For  $\underline{U}_1$  equal to 0.71 the swirl was gone, and the erosion factor was 0.84. The efficiency was reduced compared to the reference design. For this design, however, it seems like a high pressure zone appears on the suction side of the blade close to the hub, approximately midway along the blade, deflecting the flow towards the shroud, but apparently without any swirl. Thus it is probable that the design is balancing on an edge between swirling and not. A higher value of  $\underline{U}_1$  might be necessary if combining a change in this parameter with a change in another design parameter.

## Different blade angle distributions

Altering the blade angle distribution seemed as a very effective parameter to vary in order to reduce the erosion. Changing this parameter does not affect the outer dimensions of the runner or the rotational speed at all. Changing the blade angle distribution does change the energy distribution on the blade, and thus also the force distribution on the blades. Shape 1 (in figure 10.32), which seems as the most erosion reducing shape, but has also the most of the energy conversion at the trailing end of the blade. This implies that the forces are highest on this part of the blade. Having chosen a traditional thickness distribution for the blade meaning a thicker leading edge, and gradually thinner blade towards the trailing edge, the blade might not be strong enough to withstand the increased forces. Strength analyses are necessary to determine this.

Considering the results from the CFD analysis performed in the single parameter study, a high pressure zone is found close to the hub. This is not favourable, and should be avoided. Gaining control of pressure distribution by including a blade leaning feature in the design software would possibly allow the designer to remove such high pressure zones, but this has to be further studied. Another approach is to choose a more moderate shape of the blade angle distribution. Either choosing shape 5, which is the second best shape tested, in terms of less erosion, choosing a shape in between shape 1 and shape 3.

Erosion prediction in the design software, calculated according to equations 10.1 and 10.2, show that shape 1 is the blade angle distribution yielding the least erosion on the blades. The difference between shape 1 and shape 2, which will cause the most erosion, is from reducing the erosion with 24% to increasing it with 37%, as can be seen in figure 10.33. In total, that means that if shape 2 had been taken as a reference design shape, shape 1 would yield a 45% reduction of erosion, only by changing the shape of the blade.

## Changing the acceleration

Increasing the acceleration of the flow through the runner causes the erosion factor to decrease, but the slope of the acceleration-erosion factor curve is quite gentle (see figure 10.22). Traditionally, an acceleration of approximately ten percent is recommended. However, to obtain the correct inlet dimensions for the reference design, an acceleration of approximately 35 percent was necessary. An acceleration of 50 percent only reduces the erosion factor to 0.93. Increasing the acceleration even further seems somewhat drastic, especially as the full effects of a high acceleration of the flow in a Francis turbine are not known. Further study in this field should be performed before a very high acceleration is accepted as reasonable way of reducing erosion.

## Outlet diameter and the height $b$ of the runner

Theoretically, decreasing the outlet diameter causes the erosion factor to increase quite fast. However, increasing the outlet diameter does not cause the erosion factor to decrease at the same rate. The same trend can be seen for the varying the height  $b$ .

For varying the outlet diameter, the erosion factor has a minimum value for the erosion factor within the range tested, and not at the extreme end as for the other design parameters. The CFD results show good pressure distributions both blade to blade and on the blade surface. The streamlines does also look good. The efficiency is however low, implying that the hydraulic design is better for the reference runner than for this geometry. Further study to find out if a design with higher efficiency exists in between the tested parameter value and the reference design value should be performed.

For varying the height  $b$ , it seems as the erosion will be reduced further if increasing the height even more. However, an error occurs in TurboGrid for values of more than 0.4 m (in this case with the other design parameters equal to the reference design values). CFD results for  $b$  equal to 0.4 m show a swirl in the blade channel, and lower efficiency than for the reference design. All in all, it seems as only varying  $b$  is not very favourable taking flow conditions, erosion and efficiency into account. Small changes of  $b$  in combination with varying other design parameters does however seem promising, and should be studied further.

## 11.4 Selective Parameter Study

For the selective parameter study, two design parameters were changed with respect to the reference design at the same time. The first design tested allowed changes in all parameters, including the number of pole pairs. Increasing the number of pole pairs and applying shape 1 for the blade angle distribution gave a design with very low erosion factor, and a fairly high efficiency. Hence is this the most promising design tested in the parameter study.

The second selective design was established with the constraint that the rotational speed should be the same as for the reference runner. Combining shape 1 for the blade angle distribution with the reduced value of the inlet peripheral speed equal to 0.71, the erosion factor was 0.61. The CFD simulations did however show a swirl in the blade channel, similar as for the single parameter study results when just varying  $\underline{U}_1$ .

Whether the swirl in selective design no. 2 is a result of changing  $\underline{U}_1$  or the blade angle distribution is not known. Assuming that  $\underline{U}_1$  is the reason, several designs were generated for blade angle distribution shape 1 with changes in the other design parameters. The different combinations are listed in table 11.1. Theoretically, all these designs will reduce the erosion substantially, from approximately 30 to almost 50 percent. The CFD simulation results, however, show a swirl halfway through the

blade channel, close to the hub. Based on this, it seems as if the swirl is dependent on the blade angle distribution shape 1, as it appears for all the designs. Thus a more moderate blade angle distribution seems favourable.

Combinations	
Design 1:	$\overline{U_1}=0.73$
Design 2:	$\overline{D_2}=0.6$ m
Design 3:	$b=0.25$ m

Table 11.1: Design parameter values combined with blade angle distribution shape 1. The values of the parameters not listed are chosen equal to the reference design value

## 12 Conclusion

The design software has proven to be an effective tool for Francis turbine design. With the software, the turbine designer can see the result of a change immediately, and alter the variables until a promising design is obtained. The design software results compare well with CFD results as long as the design parameters are chosen within the recommended ranges.

Using the design software, a reference design was generated. CFD analysis of the reference design shows good hydraulic conditions in the runner at design load, and an acceptably high efficiency.

Erosion simulations in CFX were attempted, but with no useful results, due to strong mesh dependency, especially for finer meshes with  $y^+$  values below five. Thus the erosion factor was used as the measure of erosion for the different designs. Based on the reference design, a parameter study was performed to map the effects of varying the design parameters. CFD analyses were performed for designs which the design software predicted to have low erosion. CFD results show that increasing the number of pole pairs is a good place to start, as this gives good results in terms of flow conditions in the blade channels. In addition, the efficiency was higher for the design tested than for the reference design.

Changing the shape of the blade angle distribution does also seem to yield a fairly good reduction of erosion. This does however also change the energy distribution on the blade, which causes a different force distribution on the blade. Strength and fluid-structure analysis is necessary to determine if the blade is capable of handling the new force distribution. In addition, CFD analysis of full load and part load operation is necessary to verify the hydraulic conditions off design point.



## 13 Further Work

A more comprehensive study of mesh size for erosion prediction using CFD should be performed. It is of interest to find out if a mesh independent region exist for lower  $y^+$  values than tested here. If such a region is found, it would be of interest to investigate whether the coarse mesh region can be used to give the relative difference between two designs or not. This is desirable, as the coarse mesh simulations are very time saving. In addition, the fine mesh simulations are not possible in the student computers at NTNU, due to insufficient memory. To do this, several different designs has to be simulated in CFX for different mesh sizes.

If a mesh independent region is found for the erosion simulations, the erosion factor can be verified or invalidated using this kind of simulation results. Verification of the CFD results with experimental results would also be desirable.

Including the possibility of blade leaning in the design software has been discussed, but not implemented, due to time limitations. This will improve the designer's control of the blade geometry, and thus also blade pressure distribution. Splitter blades in the runner are also a desirable feature, which could be implemented in the design software. A study to see if splitter blades reduce or increase erosion in a runner would be of interest, especially for off-design load operation. In addition to this, the way the blade thickness is accounted for when calculating the main dimensions in the design software should be revised.

For the parameter study, the shape of the axial view was not studied at all. This should be taken into account when the optimization of the geometry is continued. This includes both the shape of the trailing edge and the shape of the shroud contour.

The main focus in this thesis has been on the runner. Optimization of guide vanes and stay vanes with respect to sediment erosion is required. Design of guide vanes and stay vanes are implemented in the design software to some extent, but for a comprehensive optimization, the design method should be re-established to allow tuning of the geometry before exporting it to TurboGrid and Pro/E.





## References

- [1] G.W. Stachowiak and A.W. Batchelor. *Engineering Tribology*. Amsterdam Boston : Elsevier Butterworth-Heinemann, 3rd edition, 2005. ISBN 9780750678360 0750678364.
- [2] Bhola Thapa. *Sand Erosion in Hydraulic Machinery*. Doctoral thesis, NTNU, Trondheim, 2004.
- [3] Mette Eltvik, Grunde Olimstad, and Eve C. Walseth. High pressure hydraulic machinery. Technical report, Waterpower Laboratory NTNU, 2009.
- [4] Haakon Hjort Francke. Konstruksjon av høytrykks Francisturbiner. Technical report, Waterpower Laboratory NTNU, 2008.
- [5] Ansys CFX Release 13.0. CFX-Solver modeling guide. Technical report, Ansys, November 2010.
- [6] Hari Prasad Neopane. *Sediment Erosion in Hydro Turbines*. Doctoral thesis, NTNU, Trondheim, 2010.
- [7] BBC. Nepal energy scheme for power crisis. <http://www.bbc.co.uk/news/world-south-asia-12846672>, March 2011.
- [8] RenewableNepal. Development of hydraulic turbines with new design philosophy as a foundation for turbine manufacturing in Nepal. Technical report, RenewableNepal, Kathmandu University, 2010. URL <http://www.ku.edu.np/renewablenepal/index.php/project-funding-and-application/77/122-project-ttl.html>.
- [9] C.G. Duan and V.Y. Karelin. Design of hydraulic machinery working in sand laden water. In *Abrasive erosion and corrosion of hydraulic machinery*, volume 2, pages 155–181. Imperial College press, London, 1 edition, 2002. ISBN 1-86094-335-7.
- [10] Helene Palmgren Erichsen. *Mechanical Design of Francis Turbine Exposed to Sediment Erosion*. Master thesis, NTNU, Trondheim, 2011.
- [11] Ole Gunnar Dahlhaug. Guide vanes in Francis turbines. Lecture notes. it’s learning, 2010.
- [12] Mette Eltvik. *Sediment Erosion in Francis Turbines*. Master thesis, NTNU, Trondheim, 2009.
- [13] Einar Bardal. *Korrosjon og Korrosjonsvern*. Tapir Forlag, NTH, Trondheim, 1 edition, 1985. ISBN 82-519-0700-4.
- [14] G.F. Truscott. A literature survey on abrasive wear in hydraulic machinery. *Wear*, 20(1): 29–50, May 1972. ISSN 0043-1648. doi: 10.1016/0043-1648(72)90285-2.
- [15] N. Tsuguo. Estimation of repair cycle of turbine due to abrasion caused by suspended sand and determination of desilting basin capacity. In *Proceedings of International seminar on sediment handling techniques*, NHA, Kathmandu, 1999.
- [16] IEC. Hydraulic machines – guide for dealing with abrasive erosion in water (draft). Technical report, International Electrotechnical Commission, 2008.
- [17] Ansys CFX Release 13.0. CFX-Solver theory guide. Technical report, Ansys, November 2010.
- [18] Kristine Gjørseter. *Design of Francis Turbine Exposed to Sediment Erosion*. Project thesis, NTNU, Trondheim, December 2010.
- [19] Alexey J. Stepanoff. *Centrifugal and Axial Flow Pumps - Theory, Design and Application*. Krieger, Florida, 2 edition, 1957. ISBN 0-89464-723-7.
- [20] Stephen Lazarkiewicz. Shaping the blade surface. In *Impeller pumps*, pages 165–174. Pergamon Press, Warsawa, 1 edition, 1965.

- [21] Hermod Brekke. *Pumper og Turbiner*. Waterpower Laboratory NTNU, 2003.
- [22] M.C. Verma. Silt friendly design of turbine and other under water components. In *Silting Problems in Hydro Power Plants*, New Dehli, India, October 1999. Central Board of irrigation and Power.
- [23] Dr B.S.K Naidu. Silt erosion problems in hydro power stations and their possible solutions. In *Silt Damages to Equipment in Hydro Power Stations & Remedial Measures*, New Delhi, 1996.
- [24] V.K. Nanda. Parameters effecting abrasion and remedial measures. In *Silting Problems in Hydro Power Plants*, New Dehli, India, October 1999.
- [25] Ole Gunnar Dahlhaug. Personal conversations, 2010.
- [26] Fridtjov Irgens. *Formelsamling mekanikk*. Tapir akademisk forlag, Trondheim, 3, 3.rd print edition, 2005. ISBN 82-519-1506-6.
- [27] Ole Gunnar Dahlhaug. Personal conversations, 2011.
- [28] Francis Turbine Design Team. Weekly meetings, 2011.
- [29] Ansys TurboGrid Release 13.0. Release notes. Technical report, Ansys, November 2010.
- [30] Florian R. Menter. Two-Equation Eddy-Viscosity turbulence models for engineering applications. *AIAA Journal*, 32(8), August 1994.
- [31] Florian R. Menter. Review of the Shear-Stress Transport turbulence model experience from an industrial perspective. *International Journal of Computational Fluid Dynamics*, 2009.
- [32] David Apsley. Turbulence modelling, 2011. URL <http://personalpages.manchester.ac.uk/staff/david.d.apsley/lectures/comphydr/index.htm>.
- [33] Per Egil Skaare. Personal conversation, March 2011.
- [34] Patrick Frawley, Julie Corish, Andy Niven, and Marco Geron. Combination of CFD and DOE to analyse solid particle erosion in elbows. *International Journal of Computational Fluid Dynamics*, 23(5):411–426, 2009. doi: 10.1080/10618560902919279. URL <http://dx.doi.org/10.1080/10618560902919279>.
- [35] Mette Eltvik. *Sediment Erosion in Francis Turbines*. Project thesis, NTNU, Trondheim, December 2008.
- [36] Mette Eltvik. Personal conversations, 2011.
- [37] Torbjørn K. Nielsen. Turbine theory. Lecture notes. it's learning, August 2011.
- [38] Hallvard Meland. *A New Design of a Francis Turbine in Order to Reduce Sediment Erosion*. Master thesis, NTNU, Waterpower laboratory, NTNU, Trondheim, 2010.

## A Sediment Erosion

This chapter is taken from Helene P. Erichsen's master thesis concerning *Mechanical design of Francis turbine exposed to sediment erosion*. Helene has been part of the Francis turbine design team at the Waterpower laboratory, but has submitted her thesis to the Department of Engineering Design and Materials.

## Sediment erosion

Wear caused by sediments is a huge problem in countries like Nepal. During the monsoon period, loads of sand and other particles often end up in the rivers due to the heavy rain. In addition, the glaciers are a large contributor to sediments. These sediments are travelling with the water from the upstream reservoir through the tunnel and penstock and into the turbine. The sediments are then impacting on the surface of the turbine and this is what is generally called erosion [17]. In other words, erosive wear is caused by the impact of particles of solid or liquid against the surface of an object [18]. Pipes, bends, pumps, turbine-machinery and other systems which transport fluids are highly exposed to erosion. In the following sections sediments, mechanisms of erosive wear and wear resistance of materials and coatings will be presented.

## Sediments

Sediments are fragments of rock and minerals loosened from the surface of the earth due to different processes. These processes are often weathering processes and the impact of rain and snow, blowing winds, flowing water and moving glaciers. The sources of sediments are the non-organic component of soils, fluvial and other deposits and rock [19].

Sediment transportation occurs when the eroded material is carried by the flowing water and it is therefore a natural phenomenon. In a geomorphologic context, land erosion and sediment transport are balancing the geological processes creating mountains, e.g. the uplift of the Himalayas was caused by the collision between the Indian plates and the Eurasian plate in the Himalayan area.

In addition to the natural phenomena, some of the contributions to sediments are man-made. These contributions are for example building of power plants in the hillsides and these contributions are not likely to be reduced during the lifetime of the power plants [19].

Bed materials in a river system may be of minerals, organic or mixed origin. Organic material is usually found in lakes and quiescent river reaches. The content of organic matter in mixed samples is determined as weight loss after glowing of the sample. Mixtures with more than

30% of organic matter are termed organic. Mineral particles are classified according to their size  $d$  and are presented in Table 1.

**Table 1: Classification of sediment particles [19]**

Sediment	Clay	Silt	Sand	Gravel	Cobbles	Boulders
Size (mm)	<0.002	0.002-0.06	0.06-2	2-60	60-250	>250

River sediments are usually mixtures of grains and particles. A common way to describe a mixture is in terms of percent finer by weight of particles with increasing grain size ( $d$ ) and the “percent finer” given as a sub script. The size  $d_{50}$  means an equally weight between finer and coarser particles. The ratio  $d_{60}/d_{10}$  is commonly used as an indicator of grading; if  $d_{60}/d_{10} > 5$  then the mixture is termed “well graded”, otherwise it is termed “poorly graded” or “uniform”.

When sediments enter a Francis turbine, they can cause much damage. Figure 1 shows the energy losses in a Francis turbine:

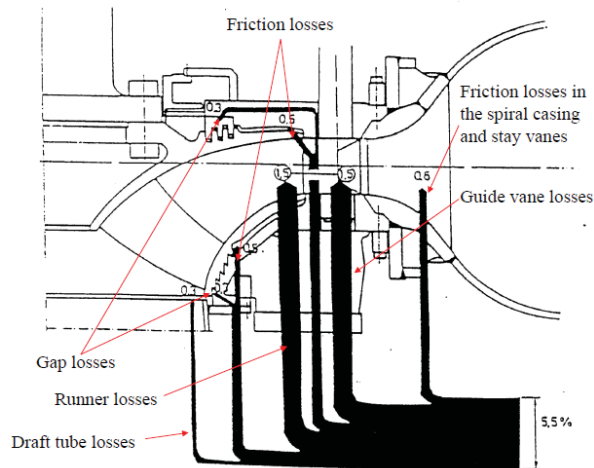


**Figure 1: Energy losses in Francis turbine [7]**

These losses are due to three reasons which are all caused by sediment erosion [4]:

- Increase in clearance between guide vane and face plates
- Friction loss due to roughening of surfaces
- Leakage through seal rings

## Mechanisms of erosive wear

Impact erosion is characterized by individual particles impacting the surface with a velocity ( $v$ ) and angle of impact ( $\alpha$ ). Removal of material over time occurs through small scale deformation, cutting, fatigue cracking or a combination of these depending upon the properties of both the wear surface and the eroding particle. These properties are presented in Table 2 while Figure 2 shows the known possible mechanisms of erosive wear.

Table 2: Factors affecting erosive wear [20]

Particle movement	Number of particles Particle velocity Impact angle
Particle properties	Size Shape Hardness Density
Target surface properties	Ductile or brittle material Stress levels Surface morphology Fracture toughness Hardness

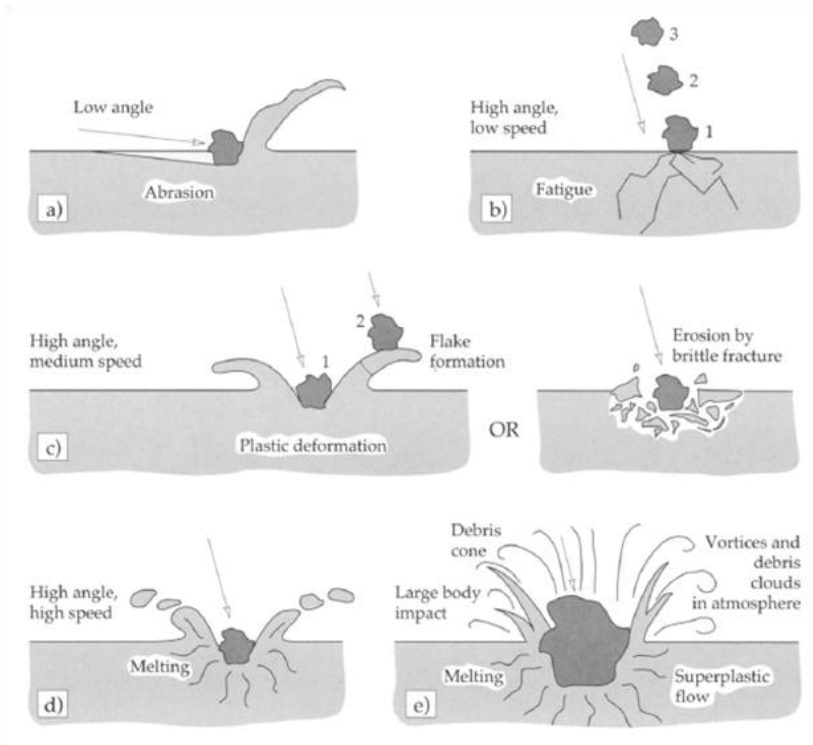


Figure 2: Possible mechanisms of erosive wear [18]

Figure 2 shows the different erosion mechanisms. Depending on the nature of the particle and the material, the degradation phenomena can be different from one to another.

*Abrasion (cutting) figure 2a*

Particles strike at low impingement angle and roll or slide when they strike the surface. Material is removed by scouring or scrapping by sharp edges of the particles.

*Surface fatigue figure 2b*

Particle strike at high impingement angle and low speed and the surface becomes weak after repeated hitting causing cracks in the material.

*Plastic deformation figure 2c*

Particle strikes at high impingement angle and medium speed, causing plastic deformation due to formation of flakes around the striking point.

*Brittle fracture figure 2c*

The particle strikes at high impingement angle and medium speed, causing brittle fragmentation provided the particle is sharp.

### Factors affecting the wear rate

Several factors are affecting the erosion rate, one of the most influencing being the impact velocity. In the case of hydro-turbines it is reasonable to assume that the particles have the same velocity as the water. In the context of this project, the velocity is assumed to be 46.6 m/s at the inlet of the runner. The relationship between velocity and wear rate is given by equation 3-1 [18]:

$$-\frac{dm}{dt} = kv^n \quad (3-1)$$

Where  $m$  is the mass of specimen,  $t$  is time of duration,  $k$  is an empirical constant,  $v$  is the velocity of the particle and  $n$  is the velocity exponent. The value of  $n$  varies for different erosion conditions such as material properties and concentration of particles. If it is assumed that the erosion rate is proportional to the particle energy, the value of  $n$  is 2. This can be shown by the formula for kinetic energy given in equation 3-2:

$$E_k = \frac{1}{2}mv^2 \quad (3-2)$$

Where  $m$  is the mass of the particle and  $v$  is the velocity. However, if more than one particle is taken into account, the number of particles impacting the surface over a specified time interval must be calculated. This can be done with equation 3-3:

$$N = \beta vct \quad (3-3)$$

Where  $\beta$  is a coefficient dependent of flow conditions around the specimen,  $c$  is the concentration of particles and  $v$  is the velocity of the flow. If assuming that the velocity of the particle is proportional to the flow velocity, the total mass loss for a time interval  $t$  is then [18]:

$$-dm = E_k N = \frac{1}{2}mv^2 \beta vct = \frac{1}{2}m\beta ctv^3 \quad (3-4)$$

This gives the velocity exponent  $n$  the value 3. However, other studies have shown that the value of  $n$  is in the range 2-4 [20].



### *Effect of particle shape, hardness, size and flux rate:*

The properties of the eroding particle are important factors which influences the erosion rate. One of the most important factors within these properties is the shape of the particle. As written in the previous section, brittle fracture may occur if the particle is sharp. A blunt particle has larger contact area, i.e. the stresses are more spread out compared to a sharp particle. This might result in ductile deformation.

The ratio of hardness of particle and substrate is influencing on the erosion rate, i.e. if the hardness of the particle is greater than that of the substrate, severe erosion will occur. However, a particle with high hardness but blunt edges will not necessarily increase the erosion rate [4]. Hence, the particle shape and hardness are complimentary in order to cause severe erosion.

Most of the erosion wear problems involve particles ranging from 5  $\mu\text{m}$  to 500  $\mu\text{m}$  [18]. If assumed that the particle has a spherical shape, then mass  $\propto d^3$ . In theory, from equation 3-2 and 3-4, this means that the erosion rate  $\propto d^3$ .

The wear rate is proportional to the particle flux rate up to certain limiting values. The limiting flux rate varies from material to material and is said to be as low as 100  $\text{kg/m}^2\text{s}$  for elastomers and as high as 10000  $\text{kg/m}^2\text{s}$  for erosion against metals by large and fast particles [18].

### *Effect of temperature*

The rate and mechanism of erosive wear are influenced by temperature. Steel starts to soften at temperatures above 600°C and this increase the wear rate significantly. If the high temperature erosion occurs in an oxidizing environment, corrosion might occur which will further accelerate the wear rate [18]. However, in a hydro turbine is it reasonable to assume that the temperature not will exceed 600°C.

### *Droplet erosion*

If a water droplet hits a surface at high impact velocity the droplet can cause as much damage as solid particles. When the droplet hits the surface, shock waves propagate and allow for release of the impact pressure. This impact pressure is sustained until the shock waves have passed through the droplet. The contact pressure can be estimated from equation 3-5 [18]:

$$p = \rho v_s v \quad (3-5)$$

This is a problem for steam-turbines and supersonic aircrafts when impingement velocity exceeds 250 m/s and the droplet diameter is greater than 200  $\mu$  m [18].

### *Effect of impingement angle*

By looking at the impact of the impingement angle, it seems convenient to divide the material behaviour in two groups, one with materials showing ductile behaviour and another one with materials showing brittle behaviour. Figure 2 shows the relationship between wear rate and impingement angle for both ductile and brittle material.

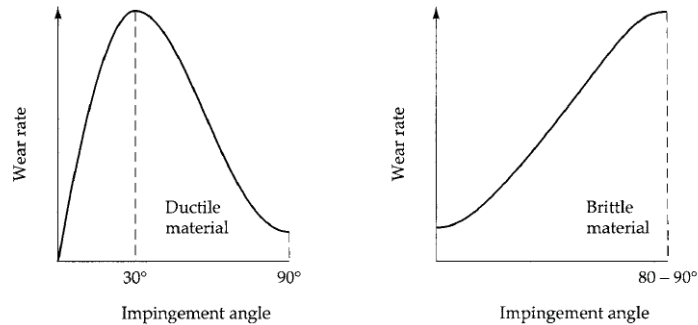


**Figure 3: Wear rate vs. impingement angle for ductile and brittle materials [18]**

For ductile materials, the highest wear rate occurs in a process of plastic deformation in which the material is removed by the displacing or cutting action of the eroding particle. The plastic deformation mechanisms are most effective from 10° up to 45° (Figure 2a). For brittle materials the largest contribution is microscopic fractures which occurs at large impingement angles. Here, the highest wear rate comes from intersections from cracks which radiate out from the point of the impact of the eroding particle. Figure 2b shows how this mechanism works.

As mentioned in chapter 2.4, the runner of a Francis turbine is often made of 13Cr4Ni, a type of martensitic stainless steel. Because of the martensitic microstructure the material shows brittle behaviour.

### **Models of erosion**

There are several different models of erosion such as Bitter's model, Finnie's model [17] for ductile materials, and Bergevin's modified model [21] which is a modification of Finnie's model. Bitter's model covers brittle materials such as 13Cr4Ni and will therefore be presented in the following in addition to a general erosion model.

A general erosion model is given by [22]:

$$W = K_{mat}K_{env}cv^n f(\alpha) \quad (3-6)$$

Where  $K_{mat}$  is a material factor which depends on hardness and ductility and  $K_{env}$  is an environment factor which includes particle size, shape, density and hardness.

#### *Bitter's models*

After studying silver plates exposed to a jet of cast iron pellets in 1962, Bitter classified the mechanisms of erosion wear into two categories. The two categories are cutting and deformation. Deformation wear is when the surface is exposed to repeated collision with relatively large impingement angle and a small amount of the surface material is removed in the form of small fragments during a subsequent process. Bitter derived the following equation for wear rate of target material due to deformation wear [23]:

$$W_D = \frac{\frac{1}{2}M(v\sin\alpha - K)^2}{\varepsilon} \quad (3-7)$$

Cutting wear occurs when a particle strikes the surface with an acute angle and the material is subjected to shear over an area equal to the vertical cross section of the particle that has penetrated into the surface. If the shearing strength is exceeded, failure occurs.

In addition to the importance of the impact angle ( $\alpha$ ) the particle velocity ( $v$ ) needs to be taken into account as well. The velocity can be divided into two components, one parallel to the surface ( $v_{\parallel}$ ) and one perpendicular to the surface ( $v_{\perp}$ ). When the particle leaves the body the value  $v_{\parallel}$  has two options, either it is zero, otherwise it is not.

Bitter derived the following equations for removed wear rate of target material due to cutting wear [24]:

$$W_{c1} = \frac{2MH(vs\sin\alpha - K)^2}{\sqrt{(vs\sin\alpha)}} \left( v\cos\alpha - \frac{H(vs\sin\alpha - K)^2}{\sqrt{(vs\sin\alpha)}} \zeta \right) \quad (3-8)$$

$$W_{c2} = \frac{\frac{1}{2}M(v^2\cos^2\alpha - K_1(vs\sin\alpha - K)^{3/2})}{\zeta} \quad (3-9)$$

Where  $\zeta$  is the energy needed to scratch out a unit volume from a surface and  $\alpha_0$  is the impact angle at which  $v_{\parallel}$  has just become zero when the particles leaves the body. The value of  $\alpha_0$  depends on material properties. If the material is soft then the threshold is  $15^\circ$  and if the material is hard then the threshold is  $60^\circ$ . Equation 3-8 is valid if  $\alpha \leq \alpha_0$  and equation 3-9 is used otherwise.

## Materials and coatings

### Materials

Different materials react differently to erosion. Materials such as lead, aluminium/aluminium-alloys, copper/copper-alloys and steel should be avoided, while materials such as stainless steel and titanium- and nickel-alloys have higher resistance because of their superior hardness compared to the former materials [22]. However, it is found that improvements in mechanical properties not always coincide with superior erosive wear resistance, e.g. erosive wear rate may increase if a material is deliberately hardened. As written in chapter 3.2, the erosive wear rate is controlled by the material characteristics and the mechanism of erosive wear and it is therefore difficult to optimize materials. Figure 4 shows the relative erosion resistance of metals as a function of impingement angle, and as expected hard materials show lower wear than soft steel at low impingement angles; the converse is true at high impingement angles. The impingement angles are  $15^\circ$  and  $90^\circ$  and the abrasive used was silicon carbide of diameter about 1 mm impinging at a velocity of 30 m/s.

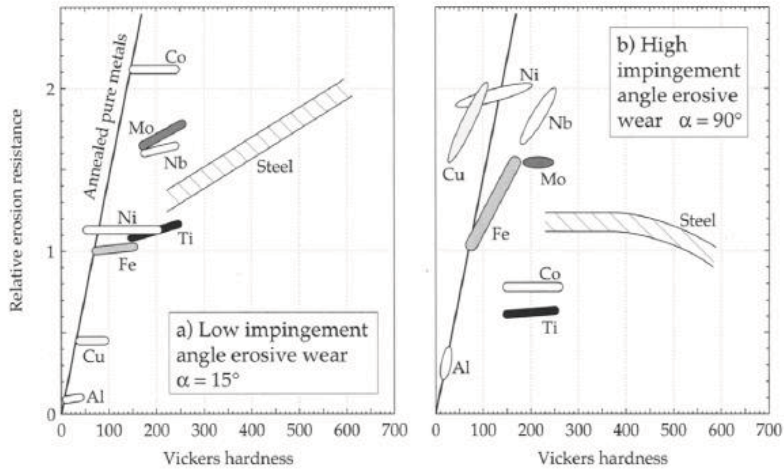


Figure 4: Effects of primary material characteristics and erosion parameters on erosive wear rate [18]

It is interesting to see how the ranking of the materials change with the impingement angles, e.g. cobalt being the most resistant material at impingement angle of  $15^\circ$ , but is the third worst at impingement angle of  $90^\circ$ . Heat treatment of steel to increase hardness improves erosive wear resistance at low impact angles but lowers the erosive wear resistance at high impact angles. However, in order to define a material's erosive resistance it is only useful to consider broad classes of materials, e.g. polymers, ceramics and metals, where distinctive differences are present and are not obscured by the effects of variables such as velocity or impingement angle. The approach adapted when developing metallic or ceramic erosion resistant materials is to make the material as hard and as tough so that the impacting particle is unable to make any impression on the surface. Alternatively, the material can be tough but with an extremely low elastic modulus so that the kinetic energy of the particles is dissipated [18].

#### *Erosive wear resistance of steels*

The literature available on the effect of steel microstructure on erosive wear rates suggests that ductile steel is the most wear resistant. Hardening of steel to form martensite offers little improvement except at very low impingement angles, and the formation of massive or lamellar carbides reduces erosive wear resistance. For low alloy carbon steels, the ferritic phase with sufficient spheroidal carbide inclusions to induce strengthening is very effective against erosive wear [18]. As a general rule, however, ductility rather than hardness should be enhanced in steels for improved erosive wear resistance.

A comparative study has been made on the erosion behaviour of 13Cr4Ni (martensitic) and 21Cr4Ni (austenitic) steels by means of solid particle impingement using gas jet. As written in chapter 3.4, 13Cr4Ni is the most widely steel used in hydro turbines. However, the maintenance repair of this steel is a primary cause of concern in its use. The quantity of martensite and its hardness are the main causes of weldability problems encountered with these steels where hydrogen embrittlement may occur. Austenitic stainless steel, on the other hand has been widely preferred by industry due to its good mechanical properties, outstanding corrosion resistance in a wide range of environment and good weldability. However, there is a need to increase the strength level of this steel in order to meet the challenges forced by severe erosive conditions faced by hydro turbine underwater parts. In raising the strength of austenitic stainless steel, N alloying has been gaining much attention. This is because N is a strong solid solution hardener, has higher solubility in austenite than C, and improves corrosion resistance. The conclusions of this comparative study are [25]:

- The erosion resistance of 21Cr4Ni-Nitronic steel is higher than that of 13Cr4Ni
- High erosion resistance of 21Cr4Ni-N steel is due to the distribution of hard carbides in the matrix of stabilized austenite.
- Mechanical properties significantly affect the erosion resistance of target material. In 21Cr4Ni-N nitronic steel, high resistance to erosion is due to (i) high hardness coupled with high ductility, (ii) high tensile toughness and (iii) high rate of strain hardening in comparison to 13/4 martensitic stainless steel.

#### *Erosive wear resistance of polymers*

The erosive wear resistance of polymers is generally poorer than that of steel. From Figure 5 it can be seen that polymers showing brittle mode of erosive wear characterized by high wear rates at high impingement angles are considerably inferior to steel.

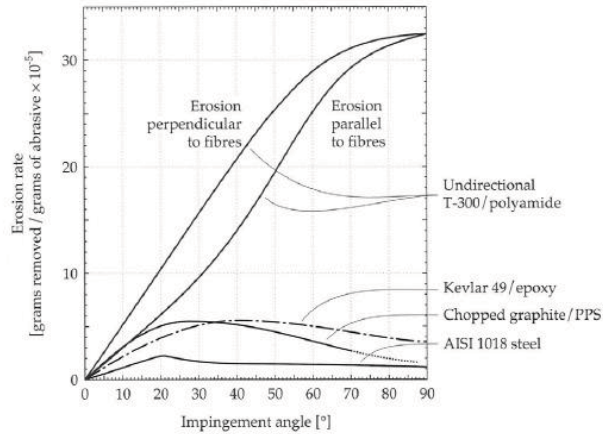


Figure 5: Erosive wear of reinforced polymers and carbon steel [18]

However, rubber is generally believed to provide good erosion resistance by elastic absorption of particle energy although this has not been demonstrated experimentally. It has been shown that the first particle impact causes no visible damage to a rubber surface and that wear depends on slow fatigue process. Because of a long “incubation period”, a weight gain may be recorded. This is due to eroding particles becoming embedded in the much softer polymer [18].

As written in section 2.4, the seals in a hydro turbine are often made of polymers such as rubber. The flow through the seals (the leakage), is dependent upon the seal clearances. A new turbine has small seal clearance and little leakage, but as the turbine is operated, the seals wear and the leakage increase, resulting in decrease of efficiency. If the water contains sediments it will result in faster seal wear and a more rapid decrease of efficiency.

#### *Erosive wear resistance of ceramics and cermets*

Ceramics are finding use as erosive wear resistant materials particularly at high temperatures. When compared to steel, ceramics show higher wear resistance at high temperature but are inferior at ambient temperatures. This is because steel becomes soft at temperatures above 600°C while ceramics become more ductile which suppresses the brittle mode of erosive wear. The principal disadvantage of ceramic materials for this application is their brittleness which may result in accelerated wear in certain cases [18].

## Coatings

A coating is a surface treatment applied onto a substrate material which is used in order to protect it from wear such as erosion or cavitation. In the case of erosion wear, hard coatings combined with ductile matrix have shown good resistance and are widely used in the oil and gas industry, but also within hydro power. The coatings can be applied by several different techniques such as thermal spraying, electro metallization, chemical vapour deposition (CVD), or physical vapour deposition (PVD).

Tungsten- carbide coatings (WC-Co) have been used to reduce fluid erosion, wear and corrosion encountered on drill bits and downhole tool assemblies used in mining as well as in the oil and gas industry. This coating has also been used in hydro turbines and will therefore be presented in the context of thermal spray coatings. In addition, two other coatings applied by the CVD technique, will be presented.

### *Thermal spray coatings for erosion purposes*

Thermal spraying was first invented by Dr. Schoop in the early 1900s after observing how lead cannon balls adhered to vertical surfaces after firing [26]. Ceramic coatings are hard coatings and can be applied by thermal spraying. An important alternative to this is ceramic-metallic coatings consisting of hard carbide particles bounded together by a metallic material. WC-M compounds where M can be Co, CoCr, Ni etc are often used, but the most common cermet used for erosive wear applications is WC with Co-binders [22].

The main range of WC-Co systems typically uses 86-88% WC and 6-13% Co [26]. If the application is used in an environment where chlorides are present, i.e. a corrosive environment, then adding 1.5-8% Cr to the matrix improves the corrosion resistance as well.

Major properties of WC-Co coatings are large hardness, better adhesion and small difference in stiffness between substrate and the top layer part. WC-Co material provides a better distribution of the contact stress and thus avoids severe delamination problems. High wear resistance comes from the incorporation of hard, homogenised distributed WC particles, which increases the coating hardness. Compared to other thermal sprayed coatings such as alumina-titanium coatings, WC-based coatings exhibit the largest toughness because of the ductile matrix (principally due to metal binders such as Co or Ni) and the composite microstructure. Severe decarburisation, forming of  $W_2C$ , may occur depending on the spraying process and this acts against wear performance at high design temperatures, as this is



the case of thermal spray techniques. These carbides are brittle and with brittle metal binder phase present, this will favour crack propagation [27].

The hardness of WC-Co coatings depend on the grain size of the WC, i.e. the hardness increases with increasing grain size [28]. The mean hardness of WC-Co coatings are 12 GPa [27].

A WC-Co coating is already used in hydro turbines (section 3.5) and has shown good resistance when applied to runner, runner blades and guide vanes.

### *CVD coatings*

Chemical vapour deposition (CVD) is a process where gaseous chemical reactants are transported into a reaction chamber in order to react to form a solid deposit on the substrate surface [29].

A family within CVD coatings is the Hardide™ family. There are several different Hardide coatings and among them the Hardide-T coating. This coating consists of tungsten/ tungsten carbide (W+WC) where the WC nano-particles disperses into W matrix which gives the material enhanced hardness of 1100 HV( $\approx 10$  GPa) to 1800 HV ( $\approx 17$  GPa). Erosion tests have shown that the Hardide-T coating resists erosion more than two times better than WC-Co when testing at impingement angles of 30°, 45°, 60° and 90°. These coatings can be applied with a thickness up to 100  $\mu\text{m}$  compared to other CVD coatings where the thickness is less than 5  $\mu\text{m}$  [30].

Other important CVD coatings are the diamond-like carbon (DLC) coatings. The DLC coatings are carbon based coatings with excellent wear properties [31]. DLC coatings have a high Young's modulus and high hardness, and the correlation between them can be shown by the following equations from [32] through [33]:

$$E = E_0(Z_{cc} - 2.4)^{1.5} \quad (3-10)$$

$$H \approx \frac{E}{10} \quad (3-11)$$

Experimentally, the hardness of thin DLC films has been found to vary between 13 GPa and 18 GPa depending on the bonding within the DLC coating [34]. The thickness of the coating is in the range from 3  $\mu\text{m}$  to 10  $\mu\text{m}$  [35].

The size of the substrate to coat is limited because CVD coatings are applied in combustion chambers. Hence, CVD coatings can be applied to small components such as runner blades or guide vanes but not on larger surfaces, e.g. the whole runner<sup>1</sup>. This is a disadvantage of CVD coatings with respect to thermal spray coatings.

### **Influence of coatings on sediment erosion in Francis turbines**

The solution of coating chosen parts in a Francis turbine was tested on one of the turbines at Cahua Power Plant in Peru. The coating used was a WC-Co coating with thickness of 0.3 mm [36]. Figure 3-6 shows the coated parts within the turbine:

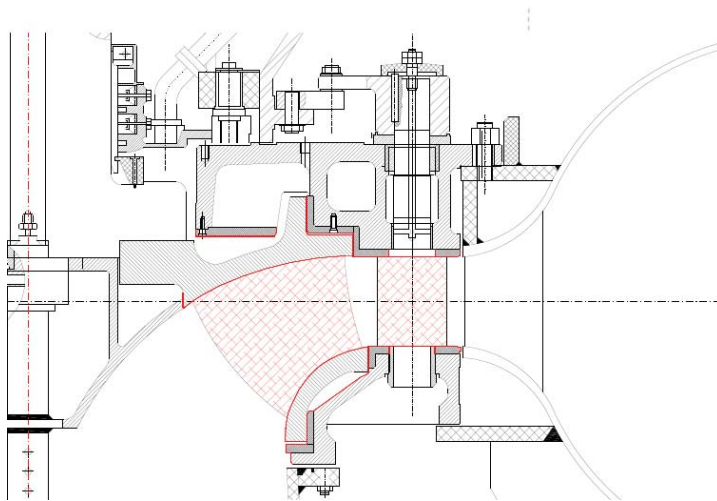


**Figure 6: Coated parts in Francis turbine [7]**

During the testing of the turbine, more than 100.000 tons of sediments flew through the turbine during the period with heavy monsoon rain. Figure 7 shows the result of the coated turbine compared to an uncoated one during the same period of time:

---

<sup>1</sup> These sizes are related to turbine currently at Jhimruk.

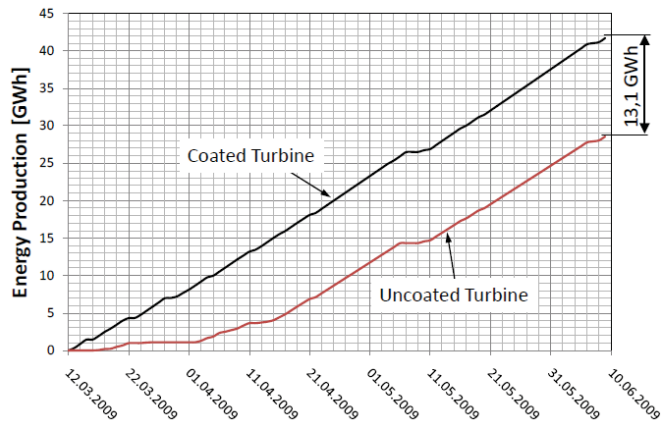


Figure 7: Coated vs. uncoated turbine at Cahua in Peru [7]

Comparison of coated and uncoated guide vanes was carried out at Jhimruk. Figure 8 shows that a coated guide vane can handle much more sediments than an uncoated one:

**DynaVec guide vane**  
130.000 tons of sediment load



**Old guide vane**  
90.000 tons of sediment load



Figure 8: Coated guide vane from DynaVec vs. old guide vane at Jhimruk [7]

This shows that WC-Co coatings have an impact on the erosion rate which again can lead to longer life time of turbines exposed to sediment erosion.

## Bibliography

1. [cited 2011 25.04]; Available from: <http://science.howstuffworks.com/environmental/energy/hydropower-plant1.htm>.
2. Thapa, B.S., *Project application Renewable Nepal*. 2010, Kathmandu University.
3. energidirektorat, N.v.-o. *Energistatus 2010*. 2011 [cited 2011 01.05]; Available from: [http://www.nve.no/Global/Publikasjoner/Publikasjoner%202011/Diverse%202011/NVE\\_Energistatus2011.pdf](http://www.nve.no/Global/Publikasjoner/Publikasjoner%202011/Diverse%202011/NVE_Energistatus2011.pdf).
4. Thapa, B., *Sand erosion in hydraulic machinery*. 2004, Norges teknisk-naturvitenskapelige universitet: Trondheim.
5. News, B. *Nepal energy scheme for power crisis*. 2011 [cited 2011 24.05]; Available from: <http://www.bbc.co.uk/news/world-south-asia-12846672>.
6. Aryal, R.S. and G. Rajkarnikar. *Water resources of Nepal in the context of climate change*. 2011 [cited 2011 13.04]; Available from: [http://www.wec.gov.np/Water%20Resources%20of%20Nepal%20main\\_March10.pdf](http://www.wec.gov.np/Water%20Resources%20of%20Nepal%20main_March10.pdf).
7. Dahlhaug, O.G., *Lecture notes in Turbomachinery*. 2010.
8. Kjølle, A., *Veileder i kvalitetssikring av små vannmaskiner*. 2005: Trondheim.
9. Brekke, H., *Konstruksjon av pumper og turbiner*. 2008, Trondheim: Vannkraftlaboratoriet.
10. Timoshenko, S.P. and S. Woinowsky-Krieger, *Theory of Plates and Shells (2nd Edition)*, McGraw-Hill. p. 51-78.
11. Brekke, H. *A review on oscillatory problems in Francis turbines and simulation of unsteady flow in conduit systems*. 1994.
12. Waløen, Å.Ø., *Maskindeler 2*. 1976.
13. Standards, I., *Geometrical product specification (GPS) in Part 1: Basis of tolerances, deviations and fits*. 2010.
14. Kjølle, A., *Vannkraftmaskiner*. 1980, Oslo: Universitetsforlaget.
15. Brekke, H., *Choice of materials for water turbines and the influence this has on design manufacture, testing and operation*. 1984.
16. Saeed, R.A., A.N. Galybin, and V. Popov, *Modelling of flow-induced stresses in a Francis turbine runner*. *Advances in Engineering Software*, 2010. **41**(12): p. 1245-1255.
17. Finnie, I., *Erosion of surfaces by solid particles*. *Wear*. **3**(2): p. 87-103.
18. Stachowiak, G.W. and A.W. Batchelor, *Engineering tribology*. 2005, Elsevier Butterworth-Heinemann: Amsterdam. p. XXIV, 801 s.
19. Lysne, D.K., *Hydraulic design*. *Hydropower development*. Vol. Vol. no. 8. 2003, Trondheim: Norwegian Institute of Technology. Department of Hydraulic Engineering. 193 s.
20. Bjordal, M., *Erosion and corrosion of ceramic-metallic coatings and stainless steel*. 1995, NTH.: Trondheim.
21. Nešič, S. and J. Postlethwaite, *Hydrodynamics of disturbed flow and erosion–corrosion. Part II — Two-phase flow study*. *The Canadian Journal of Chemical Engineering*, 1991. **69**(3): p. 704-710.
22. Bardal, E., *Korrosjon og korrosjonsvern*. 1994, [Trondheim]: Tapir. 337 s.
23. Bitter, J.G.A., *A study of erosion phenomena part I*. *Wear*, 1962. **6**(1): p. 5-21.
24. Bitter, J.G.A., *A study of erosion phenomena: Part II*. *Wear*, 1962. **6**(3): p. 169-190.
25. Chauhan, A.K., D.B. Goel, and S. Prakash, *Erosion behaviour of hydro turbine steels*. *Bulletin of Material Science*, 2008. **31**(2): p. 115-120.
26. Wood, R.J.K., *Tribology of thermal sprayed WC-Co coatings*. *International Journal of Refractory Metals and Hard Materials*, 2010. **28**(1): p. 82-94.
27. Zhu, Y.-c., et al., *Tribological properties of nanostructured and conventional WC-Co coatings deposited by plasma spraying*. *Thin Solid Films*, 2001. **388**(1-2): p. 277-282.

28. Jia, K. and T.E. Fischer, *Sliding wear of conventional and nanostructured cemented carbides*. *Wear*, 1997. **203-204**: p. 310-318.
29. Bunshah, R.F., *PVD and CVD coatings*. ASM International, ASM Handbook, 1992. **18**: p. 840-849.
30. Zhuk, Y.N., *Hardide™: Advanced nano-structured CVD coating*. *International Journal of Microstructure and Materials Properties*, 2007. **2**(1): p. 90-98.
31. Grill, A., *Tribology of diamondlike carbon and related materials: an updated review*. *Surface and Coatings Technology*, 1997. **94-95**: p. 507-513.
32. He, H. and M.F. Thorpe, *Elastic Properties of Glasses*. *Physical Review Letters*, 1985. **54**(19): p. 2107.
33. Robertson, J., *Diamon-like carbon*. *Pure and Applied Chemistry*, 1994. **66**(9): p. 1789-1796.
34. Savvides, N. and T.J. Bell, *Hardness and elastic modulus of diamond and diamond-like carbon films*. *Thin Solid Films*, 1993. **228**(1-2): p. 289-292.
35. Fujii, M., M. Ananth Kumar, and A. Yoshida, *Influence of DLC coating thickness on tribological characteristics under sliding rolling contact condition*. *Tribology International*. **In Press**, **Corrected Proof**.
36. Valmot, O.R. (2010) *Løste en av vannkraftens største utfordringer*. *Teknisk Ukeblad*.
37. PTC. [cited 2011 04.04]; Available from: <http://www.ptc.com/products/creo-elements-pro/>.
38. Dahlhaug, O.G.
39. ANSYS. [cited 2011 04.04]; Available from: <http://www.ansys.com/Products/ANSYS+13.0+Release+Highlights>.
40. ANSYS, I., *Lecture 5 Mesh quality check in Customer Training Material*. 2011.
41. ANSYS, I., *Lesson 4 Local mesh settings, in Customer training material*. 2011.
42. Kreyszig, E., *Advanced engineering mathematics*. 2006, Hoboken, N.J.: Wiley. XVII, 1094, [129] s.

## **B Design Software**

The Matlab code for the design software is found in the folder Design Software on the attached CD or zipped folder.

To run the program, the file named RunMe has to be executed.

New versions of the program are expected, as it will be used and further developed as part of the doctoral thesis of Mette Eltvik. The newest version available can be provided if contacting the Waterpower Laboratory at NTNU.